From XENON100 to XENON1T: direct dark matter searches with dual phase liquid xenon time projection chambers

Inauguraldissertation
der Philosophisch-naturwissenschaftlichen Fakultät
der Universität Bern

vorgelegt von

Lukas Bütikofer

von Zuzwil (BE)

Leiter der Arbeit:
Prof. Dr. M. Schumann

Albert Einstein Center for Fundamental Physics
Laboratory for High Energy Physics

Von der Philosophisch-naturwissenschaftlichen Fakultät angenommen.

Bern, 11. April 2017

Der Dekan:
Prof. Dr. G. Colangelo

From XENON100 to XENON1T: direct dark matter searches with dual phase liquid xenon time projection chambers

There is a wide range of astrophysical and cosmological evidence for the existence of dark matter, based on indirect observations at all length scales. Nonetheless, besides the fact that it interacts gravitationally and that it makes up $\sim 26\,\%$ of the Universe's energy density, little is know about the nature of dark matter. A plethora of experiments aim at its direct detection in underground low background detectors. Among them are the detectors of the XENON program, which exploits the technique of dual phase liquid xenon time projection chambers.

One of these detectors is XENON100 with a target mass of 62 kg, located at the underground laboratory Laboratori Nazionali del Gran Sasso (LNGS). In this thesis a background model is developed for the full exposure of $17.6\,\text{tons}\times\text{days}$ from XENON100, taken over a period of 477 live days. The model is a crucial input for the profile likelihood analysis. No signal excess above the background expectation has been found and limits on the spin-independent WIMP-nucleon interaction as well as on the spin-dependent WIMP-neutron and WIMP-proton interaction cross sections are placed. This analysis improves the previous limits from XENON100 by a factor of ~ 1.7.

We also present the first-ever search for dark matter-induced delayed coincidence signals in a dual phase xenon time projection chamber. This analysis uses a 224.6 day exposure from the XENON100 science run II. The very distinct delayed coincidence signature is predicted in the framework of magnetic inelastic dark matter which has been proposed to reconcile the modulation signal reported by the DAMA/LIBRA collaboration with the null results from other direct detection experiments. No candidate event has been found in the region of interest and upper limits on the WIMP's magnetic dipole moment have been derived. We exclude the DAMA/LIBRA modulation signal being due to magnetic inelastic dark matter at $> 90\,\%$ confidence level and exclude previously uncovered parameter space.

To improve the current experimental sensitivity to WIMP dark matter, with a realistic chance of a detection, the first ton-scale detector, XENON1T, has been built at LNGS and is currently taking science data. In the framework of this thesis an FPGA based veto system has been developed and incorporated into the new data acquisition system of XENON1T.

Contents

Chapter 1

Introduction

Over the last decades there has been a large number of astrophysical and cosmological observations that lead to the conclusion that ordinary matter, of which stars, planets and life consist, only accounts for $\sim 5\,\%$ of the Universe's energy density [1]. The remaining part is attributed to the yet unknown dark matter ($\sim 27\,\%$) and dark energy ($\sim 68\,\%$). In this chapter the evidence for dark matter and its possible nature are discussed. Furthermore, various experimental approaches in order to detect dark matter are introduced. In the framework of this thesis the search for dark matter with liquid xenon filled detectors is studied.

1.1 Evidence for dark matter

Although the phrase "dark matter" already appeared in 1922 in a publication by Kapteyn about the distribution of masses, forces and velocities of the Milky Way [2], the pioneering work by Fritz Zwicky, published in 1933, is often mentioned as the first prediction of the existence of dark matter [3]. Similar to the 1931 work by Edwin Hubble and Milton Humason [4] Zwicky studied the motion of galaxies by measuring their redshifts and noticed a large velocity dispersion in the Coma Cluster. By applying the viral theorem he was able to estimate the mass of this galaxy cluster. The viral theorem relates the time average of the total kinetic energy $\overline{T}$ with the potential energy $\overline{U}$. In the case of gravitational attraction it takes the form $2\overline{T} = -\overline{U}$. If the system is in equilibrium $\overline{T}$ corresponds to the ensemble average at any time. Thus, by approximating the kinetic energy by $T \sim \frac{3}{2}M\langle v_R^2\rangle$, where $\langle v_R^2\rangle$ is the average radial velocity, and the potential energy by $U \sim -\frac{3}{5}\frac{GM^2}{R}$, with G being the gravitational constant and R the radius of the system, the total mass of the galaxy cluster can be estimated by [5]

$$M \sim \frac{3R}{G}\langle v_R^2 \rangle. \tag{1.1}$$

By measuring the velocity dispersion of the cluster via the redshifts, Zwicky was able to show that the mass estimated using the viral theorem is in strong disagreement with the mass obtained by multiplying the number of visible galaxies by the average mass of a galaxy. This observation led him to the famous conclusion that *"...dark matter is present in much greater amount than luminous matter"* [3]. At that time, however, dark matter was still believed to consist of faint astronomical objects such as cold stars and gases.

In the 1970s there were a series of publications studying the rotation curves of spiral galaxies with the help of radio astronomy, pointing towards missing mass at larger radii of the galaxies. By measuring the 21 cm hydrogen line and its Doppler shift at different longitudes, the velocity can be measured as a function of distance to the center of the galaxy. Using these rotation curves the mass distribution $M(r)$, denoting the mass contained within a radius r, can be inferred by equalizing the gravitational acceleration and the acceleration originating from a circular orbit

$$\frac{GM(r)}{r^2} = \frac{v^2(r)}{r} \quad \Longrightarrow \quad M(r) = \frac{rv^2(r)}{G}. \tag{1.2}$$

Therefore, if the mass would be concentrated at the center of the galaxy (following the distribution of the luminous matter), $M(r)$ would be approximately constant outside a certain radius and the expected orbital velocity should follow the relation $v(r) \propto \frac{1}{\sqrt{r}}$. However, the measured rotation curves show that the velocity is constant to the outermost observable radii (see figure 1.1), indicating the existence of large amounts of mass in the outer parts of the galaxy. In 1978 the well known paper by Rubin, Ford and Thonnard was published, containing optical measurements of 10 spiral galaxies which show flat rotation curves out to the largest observed radii [6].

General relativity predicts that light should be affected by gravity and its trajectory should be bent by a strong gravitational field. Thus, a massive object between a light source and the observer will act as a gravitational lens and create multiple images of the same source. This prediction was confirmed by the observation of gravitational lensing in 1979 where two mirror images of the same quasar were detected [7]. Several years later, first observations of galaxy clusters acting as gravitational lenses were made. Today this technique is frequently used in order to estimate the total mass and the mass distribution of large objects such as galaxy clusters. In 2006 one of the most striking evidence for dark matter at the scale of galaxy clusters was published in the paper *"A*

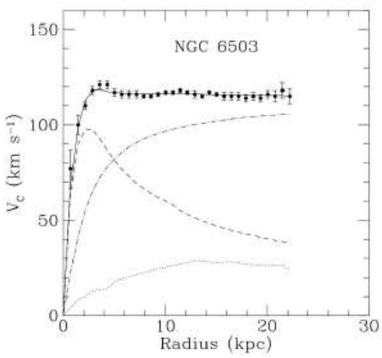

FIGURE 1.1: Measured rotation curve of a spiral galaxy (black points), together with the individual mass components. The dashed line shows the contribution of the visible disk, the dotted line the contribution of the gas and the dash-dot curve represents the dark matter halo. Figure from [9].

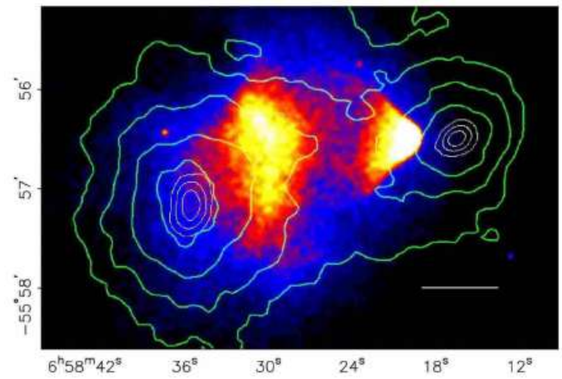

FIGURE 1.2: Image of the merging cluster 1E 0657−558 ("Bullet Cluster"). The green lines indicate the mass distribution obtained by gravitational lensing and the coloured image shows the distribution of the X-ray emitting baryonic matter, measured by Chandra. Figure from [8].

direct empirical proof of the existence of dark matter" [8]. In this work Clowe et al. studied the merger of two galaxy clusters known as the "Bullet Cluster", for which they estimated the total mass distribution by means of gravitational lensing. Furthermore, by analyzing the X-ray emission of the two clusters they were able to infer the baryonic mass distribution of this system, which for the most part consists of hot, X-ray-emitting gas. Comparing the two maps they showed that the mass distribution did not follow the distribution of the baryonic matter. This lead to the conclusion that in the course of the merger of the two clusters the gas was interacting with each other while the dark matter, which makes up the dominant part of the clusters mass budget, passed through each other essentially collisionless. This resulted in a displacement of the visible mass and the observed mass distribution of the two clusters.

With the accidental discovery of the predicted cosmic microwave background (CMB) by A. Penzias and R. Wilson in 1965 [10] a new window into the history and evolution of the Universe opened up. Originating from the decoupling of light and matter in the early Universe, anisotropies in the CMB show the density distribution of the Universe at this time ($\sim 300'000\,$y after the big bang). Small density variations of matter back then, which served as seeds for the formation of large-scale structures, are visible as tiny temperature fluctuations in the CMB. In 1992 the measurements from the COBE satellite confirmed the existence of such anisotropies at the level of $\sim$100 μK [11]. Subsequent satellite missions, such as the Wilkinson Microwave Anisotropy Probe (WMAP) [12] and the more recent Planck mission [1] (see figure 1.3), provided precise measurements of the CMB over the full sky. The angular power spectrum of the fluctuations can be well described by the ΛCDM model, which depends on cosmological parameters like the

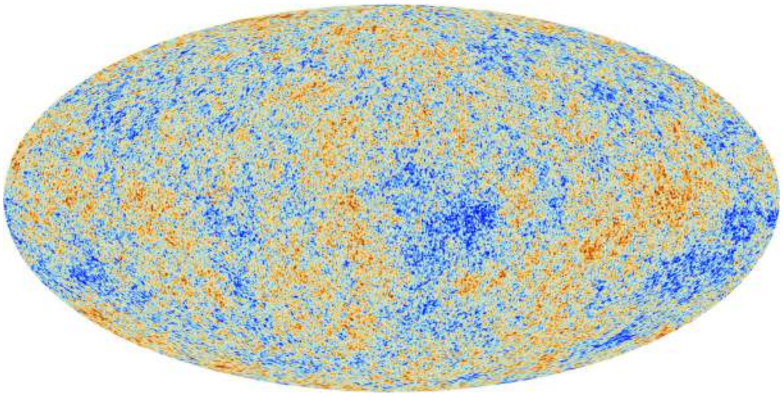

FIGURE 1.3: Fluctuations of the cosmic microwave background (CMB) as observed by the Planck satellite. Cosmological parameters like the baryon density, the cold dark matter density, and the dark energy density can be deduced by analysing the power spectrum of the anisotropies of this map. Image credit: ESA and the Planck Collaboration [1].

baryon density, the cold dark matter density, and the dark energy density. Thus, by fitting the measurements with this model it is possible to derive constraints on these parameters with striking precision. These fits tell us that only $(4.85 \pm 0.06)\,\%$ of the Universe's energy density is due to ordinary matter, while $(25.89 \pm 0.33)\,\%$ is assigned to dark matter and the remaining part to dark energy [1]. This result provides evidence for dark matter at the largest scales and represents the most precise measurement of the abundance of dark matter in our Universe.

1.2 What is dark matter made of?

Although the existence of dark matter started to become evident with the study of the dynamics of galaxy clusters in 1933 [3], it was still not clear what dark matter is made of. At that time nobody thought of a new particle when discussing the so calle "missing mass problem". A common theory was that dark matter consists of non luminous or faint massive objects that are not observable like stars. Such objects could be planets, dwarf stars, neutron stars, or black holes, later summarised under the term "MACHOs" (massive astrophysical compact halo objects). Thanks to gravitational lensing, the light of a star or quasar can be deflected by a massive object (MACHOs) in the foreground if it gets well aligned with the source. This effect is called gravitational microlensing and causes a variation of the light curves over a time scale of months. Searching for such microlensing events the MACHO, EROS and OGLE collaborations started to survey millions of stars in order to test if dark matter consisted of MACHOs. In 1993 the first observations of microlensing events were reported by the MACHO and EROS collaboration located in the Large Magellanic Cloud [13, 14]. At the time the

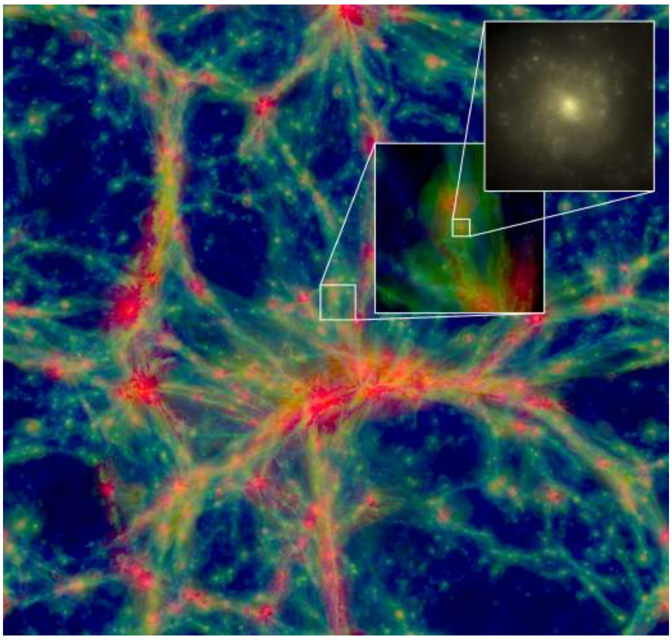

FIGURE 1.4: Slice through the simulation volume of the Eagle simulation showing the intergalactic gas colour coded from blue (cold temperature) to red (hot temperature). Hot gas has temperatures of more than 100,000K, and is contained with dark matter structures that host galaxies. The insets zoom into a spiral galaxy, showing first its gas, and then its stellar disc. Figure from [18].

observed rate of such events was consistent with the expectation from a dark matter halo dominated by MACHOs. However, after acquiring almost 7 years of data, the EROS collaboration was able to place an upper limit of only 8 % of the fraction of the Milky Way halo mass consisting of MACHOs [15]. Furthermore, by studying the CMB one can conclude that only ∼5 % of the Universe's energy density is due to baryonic matter and thus MACHOs as an explanation of dark matter are excluded.

In the 1980s new results from numerical simulations showed that dark matter should be non-relativistic (cold) in order to be able to explain the formation of large scale structures in the Universe [16]. The only possible dark matter candidate from the standard model which is neutral and only weakly interacting, the neutrino, was thus ruled out as well, since it would freeze out in the early Universe at relativistic temperatures and form "hot dark matter" [17]. This showed that the standard model cannot account for the observed large fraction of dark matter and that one or more new particles are needed in order to explain the missing mass. In figure 1.4 a slice through the simulation volume of the recent Eagle simulation is shown [18].

There are various models that predict such particles. In the following, two well-motivated theories are briefly discussed, axions and weakly interacting massive particles (WIMPs). These two models are appealing, as they have been constructed in order to solve open questions in the standard model of particle physics and not the problem of dark matter in particular.

Axions

Despite the success of the theory of quantum chromodynamics (QCD) the underlying mechanism of charge-parity (CP) conservation is still not understood.

The Lagrangian of Quantum chromodynamics contains a CP-violating term, which would lead to a finite electric dipole moment of the neutron. However, such a dipole moment is not observed and very tight limits are placed. A possible solution to this so called "strong CP-problem" was proposed in 1977 by Roberto Peccei and Helen Quinn [19] who introduced a new spontaneously broken global U(1) symmetry. This makes the pre-factor of the CP-violating term dynamic, which allows it to "roll" to a value close to zero. Frank Wilczek [20] and Steven Weinberg [21] pointed out that a new pseudo-Nambu-Goldstone boson, called the axion, emerges from this broken symmetry. The mass of this original axion was at the MeV-scale, and excluded quickly by astrophysical and laboratory constraints. Nevertheless, there is still the possibility of so called "invisible" axions with a mass of $\mathrm{m}_a \sim 10^{-6} - 10^{-4}\,\mathrm{eV}$ as discussed in [22–25]. This type of axions could have been produced in the early Universe through a non-thermal production mechanism (QCD phase transition) and could account for dark matter.

There are several experiments looking for axions. The Axion Dark Matter Experiment (ADMX) is looking for astrophysical axions using a large microwave resonant cavity in which axions might be converted into microwave photons. The sensitivity of this experiment is maximized by choosing a resonant cavity frequency corresponding to a certain axion mass. Thus, by changing the resonant frequency a range of axion masses can be scanned. The ADMX experiment excluded axion models of dark matter in a mass range of $\mathrm{m}_a = (1.9 - 3.53)\,\mu\mathrm{eV}$ [26]. OSQAR [27] and ALPS [28], on the other hand, are using the so called "light shining through walls" technique, based on the fact that photons from an intense laser beam could be converted into axions in a strong magnetic field. These axions then pass through a "wall" and can be converted back into detectable photons. Due to the coupling of axions to electrons it is also possible to search for axions in liquid xenon through the axio-electric effect, through which an axion is absorbed similar to the photoelectric effect. XENON100 searched for this type of signals in a dual phase liquid xenon time projection chamber [29].

Weakly interacting massive particles

Since baryonic matter and neutrinos can't account for dark matter a new, more massive particle which only interacts at the weak scale was proposed. It is called the weakly interacting massive particle (WIMP). In the standard model no such particle is known, but for example in the framework of supersymmetry (with conserved R-parity) there is a "natural" WIMP candidate, the neutralino [30]. Supersymmetry is a much discussed extension of the standard model which predicts that for each particle there is a supersymmetric partner, where the superpartners of the W, Z and H form the neutralino. Like in the case of the axion this candidate is appealing because the underlying theory itself was not introduced in order to solve the dark matter problem, but in this case the hierarchy problem of the standard model (i.e, why are the electroweak scale and the Planck so different, or why is the Higgs mass at the electroweak scale and not near the Planck scale) or the unification of forces at higher energies.

Another strong argument for WIMPs is the "WIMP miracle". In the early Universe WIMPs and standard model particles were in thermal equilibrium and were produced and annihilated in pairs at equal rates. Due to the expansion of the Universe, however, at some point the temperature dropped below the WIMP mass and their creation stopped. As a result the WIMP density dropped due to self annihilation until it was small compared to the annihilation cross section, leaving a constant relic WIMP density. This process can be described by the following equation [30]

$$\frac{dn_\chi}{dt} = -\langle\sigma_a v\rangle \left[(n_\chi)^2 - n_\chi^{eq}\right] - 3Hn_\chi \tag{1.3}$$

which defines the evolution of the number density of WIMPs $n_\chi(t)$ over time. $\langle\sigma_a v\rangle$ denotes the thermally averaged annihilation cross section times velocity, n_χ^{eq} is the number density at thermal equilibrium and H is the Hubble expansion rate. This equation can be understood such that the first term on the right side accounts for the annihilation of WIMPs, the second term for their creation due to the inverse reaction and the last term accounts for the expansion of the Universe. If the creation of WIMPs stops due to the decreasing temperature, the number density will drop until the third term dominates and the number density will be driven by the expansion of the Universe. The time at which this happens depends on the interaction cross section of the WIMP. An approximate solution of equation (1.3) for the relic density Ω in units of the critical density is given by [30]

$$\Omega h^2 \sim 3 \cdot 10^{-27}\,\mathrm{cm}^3\mathrm{s}^{-1} \frac{1}{\langle\sigma_a v\rangle} \tag{1.4}$$

where h denotes the Hubble constant in units of $100\,\mathrm{km\,s^{-1}\,Mpc^{-1}}$. The actual "miracle" is that if we assume an annihilation cross section at the weak scale for a particle with a mass of the order to 100 GeV/c^2, given by

$$\langle \sigma_a v \rangle = \alpha^2 (100\,\mathrm{GeV})^{-2} \sim 10^{-25}\,\mathrm{cm}^3\mathrm{s}^{-1}, \tag{1.5}$$

the resulting relic density is remarkably close to the observed dark matter density. In the framework of this thesis, the focus is on the search for WIMPs using liquid xenon filled detectors.

1.3 Detection of WIMPs

Today there is a plethora of experiments, utilizing different approaches to search for WIMP dark matter. At collider experiments, such as ATLAS and CMS at the Large Hadron Collider (LHC), WIMPs might be produced in the collisions of high energetic protons. WIMPs wouldn't interact inside the detector (like neutrinos) and thus would leave only a "signature" of missing energy. This is further discussed in section 1.3.3. Indirect searches on the other hand try to detect products of the annihilation of dark matter particles, e.g., neutrinos, gamma rays, antiprotons and positrons, see section 1.3.2. Direct detection experiments, such as the XENON experiments discussed in more detail in chapter 2, aim for the detection of (in-)elastic scattering between WIMPs and atomic nuclei.

1.3.1 Direct detection

In this section the expected interaction rates and the different experimental approaches for direct detection experiments are discussed in more detail.

Interaction rate

As shown in section 1.1 there is clear evidence for dark matter at the scale of galaxies where the measured rotation curves reveals the existence of a halo of dark matter. This is also true for our own galaxy, the Milky Way [31]. Thus, while orbiting the center of the galaxy, the Earth is moving through a halo of dark matter, facing a continuous "WIMP wind". The idea of directly detecting WIMPs from this halo through elastic scattering off nuclei goes back to Goodman and Witten in 1985 [32].

Following the summary in [33] the differential interaction rate of elastic scattering can be described as

$$\frac{dR}{dE_\mathrm{R}} = \frac{\rho_0}{m_\mathrm{N} m_\chi} \int_{v_{min}}^{v_{max}} v f_\mathrm{n}(\mathbf{v}) \frac{d\sigma}{dE_R} d^3 v, \tag{1.6}$$

with m_{N} being the nucleus mass, m_χ the WIMP mass, $\rho_0 = 0.3\,\mathrm{GeV/cm^3}$ the local dark matter density [34]. $\mathbf{v}$ and $f_{\mathrm{n}}(\mathbf{v})$ denote the WIMP velocity and the normalized velocity distribution. The WIMP-nucleus differential cross section $\frac{d\sigma}{dE_R}$ incorporates inputs from particle physics and can be expressed as

$$\frac{d\sigma}{dE_R} = \frac{m_{\mathrm{N}}}{2\overline{\mu}^2 v^2}\left(\sigma_0^{SI} F_{\mathrm{SI}}^2(E_{\mathrm{R}}) + \sigma_0^{\mathrm{SD}} F_{\mathrm{SD}}^2(E_{\mathrm{R}})\right). \tag{1.7}$$

It is separated into a spin-independent (SI) and spin-dependent (SD) part, where $\overline{\mu}^2$ is the reduced mass of the WIMP nucleus system and $\sigma_0^{\mathrm{SI,\,SD}}$ denote the cross sections at zero momentum transfer. The form factors $F^2_{\mathrm{SI,\,SD}}$ take into account the coherence loss at higher momentum transfer. For SI interactions this can be expressed by the Helm form factor [35]

$$F^2(q) = \left(\frac{3j_1(qR_1)}{qr_n}\right)^2 \exp\left(\frac{-q^2 s^2}{2}\right), \tag{1.8}$$

where $q = \sqrt{2m_{\mathrm{N}}E_{\mathrm{R}}}$ is the momentum transfer, j_1 the Bessel function of the first kind and $s \simeq 0.9\,\mathrm{fm}$. r_n is the nuclear radius, which can be expressed as

$$r_n = \sqrt{1.23A^{1/3} - 3.82}\,\mathrm{fm}. \tag{1.9}$$

The spin-independent cross section at zero momentum transfer is given by

$$\sigma_0^{\mathrm{SI}} = \frac{4\overline{\mu}^2}{\pi}\left[Zf_p + (A-Z)f_n\right]^2, \tag{1.10}$$

where Z and A are the atomic and mass numbers. This WIMP-nucleus cross section can be normalized to a single nucleon, which is conventional when interpreting results from direct dark matter experiments to allow comparison of different targets. It is given by

$$\sigma^{p,n} = \frac{1}{A^2}\frac{\mu_{p,n}^2}{\overline{\mu}^2}\sigma_0^{\mathrm{SI}}, \tag{1.11}$$

where $\mu_{p,n}$ is the reduced mass of the WIMP-nucleon system. In many cases the proton coupling f_p and the neutron coupling f_n are similar and the SI part of equation (1.7) simplifies to

$$\left(\frac{d\sigma}{dE_{\mathrm{R}}}\right)_{SI} = \frac{2m_{\mathrm{N}}A^2(f_p)^2}{\pi v^2}F^2(E_{\mathrm{R}}). \tag{1.12}$$

In general both the SI and the SD contributions have to be taken into account. However, for heavy targets (A>20) the SI component dominates unless it is suppressed by some process. Figure 1.5 shows the differential event rate for different target materials. At zero momentum transfer (i.e., E_R=0) the cross section, and thus the event rate for heavy target materials is higher due to the A^2 enhancement in equation (1.12). The shape of the spectrum is given by the exponentially falling form factor and the energy dependent

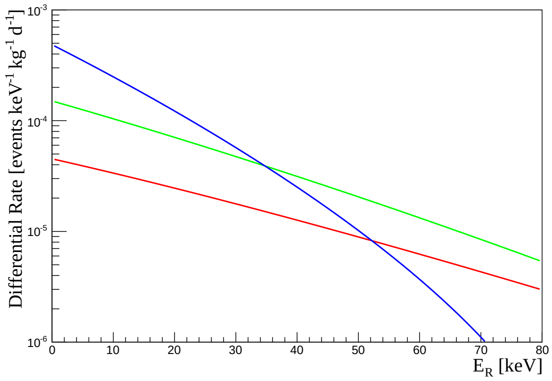

FIGURE 1.5: Expected differential event rate for a WIMP-nucleon cross section of $1 \cdot 10^{-44}\,\mathrm{cm}^2$ and a WIMP mass of $100\,\mathrm{GeV/c}^2$ for different target materials. The red line represents argon (A=40), the green line germanium (A=73) and the blue line xenon (A=131). The drop in the xenon rate at higher recoil energy E_R is from the form factor.

lower boundary, $v_{\min}$, of the velocity integral in equation (4.2), which is given by

$$v_{\min} = \frac{\sqrt{m_{\mathrm{N}} E_R}}{\sqrt{2}\mu}. \tag{1.13}$$

The SD WIMP-nucleon cross section is given by

$$\left(\frac{d\sigma}{dE_{\mathrm{R}}}\right)_{SD} = \frac{16 m_{\mathrm{N}}}{\pi v^2} \Lambda^2 G_F^2 J(J+1) \frac{S(E_{\mathrm{R}})}{S(0)} \tag{1.14}$$

where G_F is the Fermi constant, J the total angular momentum of the nucleus and $S(E_{\mathrm{R}})$ is the SD form factor. Λ is given by

$$\Lambda = \frac{1}{J}\left[a_p \langle S_p \rangle + a_n \langle S_n \rangle\right], \tag{1.15}$$

with $\langle S_{p,n} \rangle$ being the expectation values of the proton and neutron spin operators and $a_{p,n}$ being the effective proton and neutron couplings. WIMPs will only couple to isotopes with a non-zero spin. Natural xenon contains two such isotopes, ^{129}Xe (spin $1/2^+$) and ^{131}Xe (spin $3/2^+$), which makes it sensitive to the SD channel. For a more detailed discussion of the SD contribution see for example [33] or [36].

Direct detection experiments

Due to the exponentially falling recoil spectrum of the WIMP-nucleon interaction, shown in figure 1.5, one important prerequisite for a direct dark matter detector is a low energy threshold. Since the expected interaction rate is very low, the detectors also need to have a low radioactive background. WIMPs are expected to scatter once off the atomic nuclei, and thus the possibility of a detector to discriminate between nuclear recoils (NR) and electronic recoils (ER) results in a major reduction of the background originating from γ radiation and β decays, which produce electronic recoils. Further signatures that can be exploited are the annual variation of the total event rate arising from the motion of

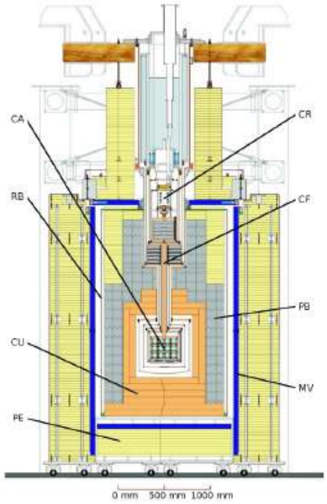

FIGURE 1.6: Schematics of the CRESST-II experiment. The detector carousel (CA) (shown in figure 1.7) is connected to the mixing chamber of the cryostat (CR) by a long copper cold finger (CF) in order to reduce background originating from the dilution refrigerator. The gas-tight radon box (RB) encloses the low background copper (CU) and low background lead shielding (PB). It is covered by a plastic scintillator muon-veto (MV) and a 45 cm thick polyethylene neutron moderator (PE). Figure from [40].

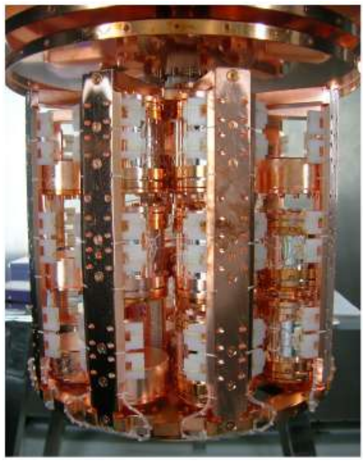

FIGURE 1.7: Detector carousel containing the crystals out of $CaWO_4$ from CRESST-II made of ultrapure copper, electropolished to reduce surface contamination. The structure can accommodate 33 detector modules (i.e., 10 kg of target mass) which can be mounted or dismounted individually. The carousel is mounted at the lower end of the cold finger. The entire structure is cooled to $\sim$ 10 mK. Figure from [40].

the Earth around the Sun [37, 38] and the directionality of the signal due to the WIMP wind orientation with respect to the Earth [39]. Event-by-event position reconstruction allows the identification and rejection of event populations at the surface of the detector as well as double scatter interactions, since WIMPs are expected to interact uniformly and only once in the detector.

The deposited energy of a particle interaction inside a detector is shared between three different channels: ionization, heat/phonons and excitation/scintillation. Typical direct detection experiments are exploiting either one or two of those excitation channels. Currently the most sensitive direct detection experiments are based on cryogenic solid state detectors, on noble liquid detectors and superheated liquid detectors, which will all be discussed briefly below.

Cryogenic solid state detectors

Cryogenic detectors are operated at sub-Kelvin temperatures and typically reach an extremely low threshold (few keV) and a high energy resolution. Mainly due to their low threshold these detectors set the strongest limits at low WIMP masses (<6 GeV).

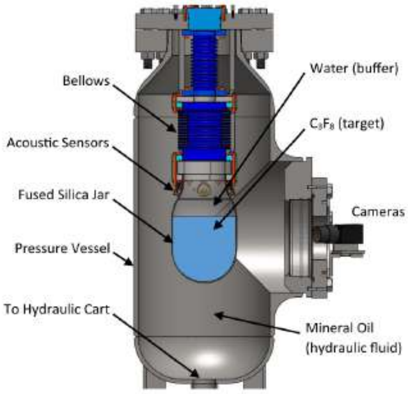

FIGURE 1.8: A schematic of the PICO-2L bubble chamber containing 2.9 kg of its target material C_3F_8. Figure from [45].

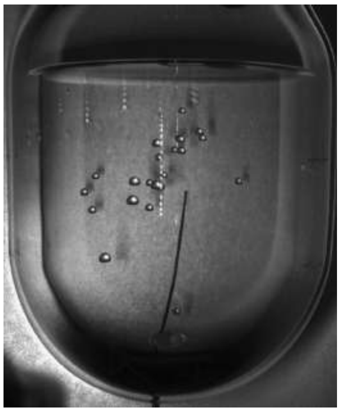

FIGURE 1.9: Multiple bubbles in the PICO-2L detector resulting from a neutron interaction. Figure from [46].

Typically they rely on the observation of tiny temperature increases in dielectric crystals, induced by a small energy deposition of an interacting particle. The additional measurement of the ionization signal allows for an excellent discrimination between NR and ER, achieving an ER rejection level up to 99.99 % [41]. Experiments following this strategy with Ge crystals are SuperCDMS [42] and EDELWEISS [43]. Instead of the ionisation signal the CRESST [44] experiment measures the scintillation light generated in $CaWO_4$ crystals. In CRESST the recoil energy is determined by the phonon signal and the light signal is used in order to distinguish between ER and NR interactions. The rejection power at low energies, however, is limited due to statistical fluctuations in the number of scintillation photons produced. In figure 1.6 a schematics and in figure 1.7 a picture of the CRESST experiment is shown.

Superheated liquid detectors

A completely different technique is used in superheated liquid detectors such as PICO [47] (shown in figure 1.8), PICASSO [48], COUPP [49] and SIMPLE [50]. These detectors are bubble chambers. Their target material mainly consists of fluorine, which makes them especially sensitive to spin-dependent interactions due to the unpaired proton resulting in a total angular momentum of ^{19}F of $1/2^+$. The pressure and temperature of the liquid target can be controlled such that only NRs with their high ionizing density lead to bubble formation (see figure 1.9), while the detector remains completely insensitive to ER and thus to background from γ and β radiation. The formation of bubbles can be detected visually and acoustically. Using the acoustic signal it is possible to discriminate between NR and background originating from α interactions [48].

Liquid noble gas detectors

Liquid noble gas detectors use liquid xenon (LXe) or liquid argon (LAr) as target materials, exploiting their good scintillation and ionization properties. Using those liquids as a target allows for the construction of large and homogeneous detectors, taking advantage of their self-shielding properties in order to reduce γ and β background originating from detector materials. Current liquid noble gas detectors either measure the scintillation light only or the scintillation plus the ionization signal. In experiments using LXe targets, particle identification is based on the ratio of these two signals, while in LAr it is possible to also discriminate between NR and ER based on the pulse shape of the scintillation light [51]. Current experiments with LXe targets are LUX [52], PandaX [53] and the first ton scale detector XENON1T [54]. The dual phase time projection chambers used by these experiments are currently the most sensitive detectors for probing the WIMP-nucleus scattering cross section above $\sim 5\,\mathrm{GeV/c^2}$. The design of such detectors is described in detail in chapter 2.

Dark matter detectors using a LAr target are for example DarkSide-50 [55], which measures scintillation light and ionization charge, or the single-phase detector DEAP-3600 at SNOLAB, in Sudbury, Canada [56], which only measures scintillation light. One challenge of using LAr is the radioactive isotope ^{39}Ar, present in atmospheric argon due to cosmogenic activation. One possible solution to this problem is the extraction of argon from underground reservoirs, where it is protected from cosmic rays and the ^{39}Ar is mostly depleted [55, 57].

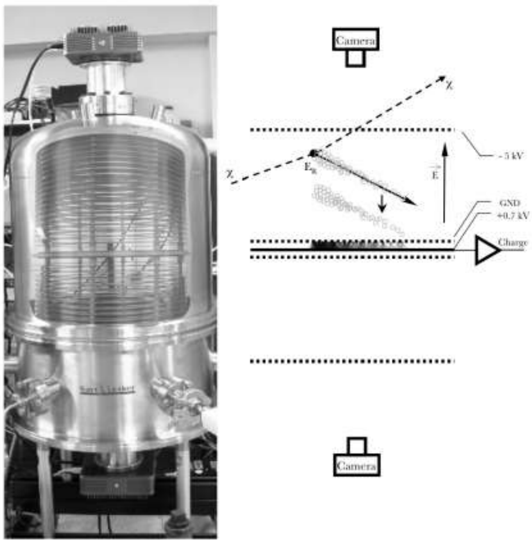

FIGURE 1.10: **(left)** Photograph of the 10-liter DMTPC detector with an image of its dual TPC overlaid to provide an artificial glimpse inside the vacuum vessel. The CCD cameras (top and bottom) each view an amplification region. The stack of stainless steel field shaping rings conditions the drift fields. **(right)** A schematic representation of a WIMP-nucleus elastic scattering event in the detector. The resulting track inside the TPC has a length of $\sim 6\,\mathrm{mm}$ with a higher density at the interaction point. Thus, a directional detection of the incident particle is possible. Figure from [58].

Directional detectors

One of the most convincing arguments of a potential NR signal being due to WIMPs from the galactic halo would be their directional signature. WIMPs from the galactic halo are expected to come from a preferred direction (constellation of Cygnus) given by the motion of the Sun through the Milky Way. Thus, the track of nuclear recoils induced by WIMPs should point preferably in that direction, taking into account the diurnal variation due to the rotation of the Earth. However, since NR tracks in solids or liquids are only $\lesssim$100 nm, directional detectors are based on gaseous targets. One of the main challenge of using gaseous targets is to accumulate a sizeable target exposure, which is required considering the existing constraints on the WIMP-nucleon cross section. The non-dense target also make self-shielding for background reduction inefficient. Current directional experiments in the research and development phase are DRIFT [59], DMTPC [60] and MIMAC [61]. A photograph and scheme of DMTPC is shown in figure 1.10. In table 1.1 a compilation of the different direct detection techniques is shown.

Direct detection techniques		Energy threshold	Energy resolution	Current target mass	Scalability	Directional signal	Background level	Background rejection power
Cryogenic solid state detectors		✓✓✓	✓✓✓	✓(✓)	✓	×	✓	✓✓✓
superheated liquid detectors		✓✓	✓	✓	✓✓	×	✓	✓✓✓
Liquid noble gas detectors	LXe	✓✓(✓)	✓	✓✓✓	✓✓✓	×	✓✓✓	✓✓
	LAr	✓(✓)	✓	✓✓✓	✓✓✓	×	✓(✓)	✓✓✓
Low pressure gas TPCs		✓	✓✓	(✓)	×	✓✓✓	✓	✓✓

TABLE 1.1: Compilation of different direct detection techniques and a qualitative rating of their different properties.

1.3.2 Indirect detection

A complementary way to search for dark matter is its indirect detection via its annihilation products. The approach relies on the assumption that WIMPs are their own anti-particles, which annihilate into standard model particles. Possible processes are

$$\chi\overline{\chi} \longrightarrow q\overline{q},\, l\bar{l},\, W^{+}W^{-},\, ZZ,$$

where the products eventually decay into electrons, positrons, neutrinos, protons, anti-protons and γ-rays. These particles can then be detected by suitable detectors. Since these experiments do not have to measure dark matter directly on Earth, it is advantageous to look at objects where a large over-density of dark matter is expected. One example for an interesting target is the Sun, since it should accumulate WIMPs in its

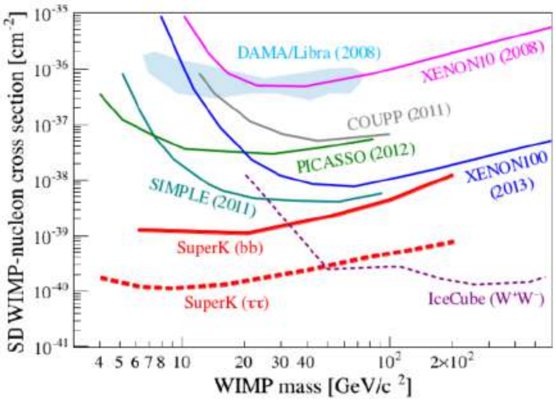

FIGURE 1.11: Limits on the spin-dependent scattering cross section derived from indirect measurements by Super-Kamiokande (red lines) [62]. Due to the low threshold, the limits are much stronger than other indirect searches (e.g., from IceCube [63]) and are also superior to direct searches (proton-only couplings). Figure from [64].

center while moving through the dark matter halo. The number-density of WIMPs in the Sun is given by

$$\frac{dN_\chi}{dt} = C_\odot - A_\odot N_\chi^2 - E_\odot N_\chi, \tag{1.16}$$

where $C_\odot$ defines the capture rate, depending on the WIMP-nucleon scattering cross section, and $A_\odot$ takes into account is the process of annihilation. Evaporation losses are described by $E_\odot$. Assuming that the capture and annihilation rates are in equilibrium, and neglecting evaporation losses, the annihilation can be described by

$$\Gamma_\odot = \frac{1}{2} A_\odot N_\chi^2 = \frac{1}{2} C_\odot. \tag{1.17}$$

Since this rate only depends on the scattering cross section, indirect detection results from dark matter annihilation in the Sun can be directly compared to direct dark matter searches. By searching for neutrinos originating from dark matter annihilation in the Sun, neutrino observatories are able to place constraints on the WIMP scattering cross section using the equilibrium assumption from above. Such analyses have been performed by Super-Kamiokande [62] and IceCube [63], shown in figure 1.11. Due to the A^2 term in the SI-scattering cross section (see equation 1.12), SD scattering dominates the capture rate $C_\odot$ of WIMPs in the core of the Sun. Thus, these kinds of analyses are mainly sensitive to the SD-scattering cross section and since the Sun predominantly consists of protons, the constraints are on proton-only couplings. Due to its lower energy threshold of $\sim 5\,\mathrm{MeV}$, SuperK is more sensitive at lower WIMP masses compared to IceCube.

Another clear signature for WIMP annihilation would be a mono energetic γ-line at m_χ from the annihilation process $\chi\overline{\chi} \longrightarrow \gamma\gamma$, as well as a broader peak at lower energies from $\chi\overline{\chi} \longrightarrow \gamma Z$. Even though the direct coupling of WIMPs to photons is suppressed at tree level, these signatures might be observed in the γ-spectrum thanks to the clear line-structure. In 2012 there was a publication, claiming that the Large Area Telescope on the Fermi Satellite (Fermi-LAT) had measured a γ-line with an energy of 130 GeV at

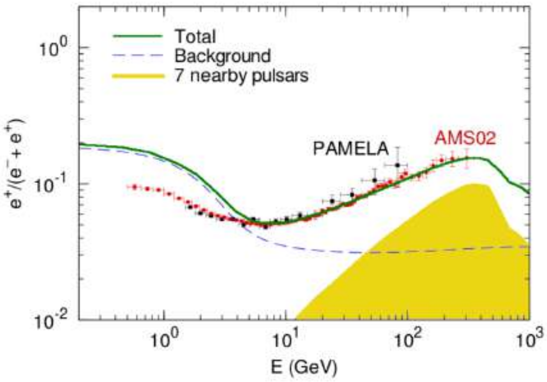

Figure 1.12: The rising positron fraction $e^+/(e^- + e^+)$, as observed by PAMELA [67] and AMS-02 [68]. The yellow area in the figure models the summed contribution of seven nearby pulsars, which describes the observed spectral shape very well [70]. Figure from [64].

the center of the Milky Way [65]. However, a similar analysis by the Fermi collaboration [66] didn't confirm this result.

In 2008 the PAMELA experiment measured for the first time an excess in the positron fraction above $\sim 5\,\text{GeV}$ [67], which can be interpreted as being due to annihilation of dark matter. Later the AMS-02 instrument confirmed this measurement and showed that the positron flux keeps increasing up to energies of $\sim 300\,\text{GeV}$ [68] (see figure 1.12). However, a dark matter interpretation of the rising positron fraction is in conflict with the absence of a similar excess in the anti-proton ratio [69]. Moreover, the amplitude of the positron signal is three orders of magnitude larger then what is expected according to the WIMP miracle. Alternatively the positron excess can also explained by including known astrophysical objects (like pulsars), which is shown in figure 1.12 [64].

As can be seen in the case of the γ-line and the positron excess, in indirect searches it is difficult to exclude all possible background processes, and thus to prove that a potential signal is due to annihilation of dark matter. Therefore, any signal claim must be confirmed by direct detection experiments in order to prove a dark matter detection.

1.3.3 Collider searches

Another approach to search for WIMP dark matter particles is to create them in a particle collider, such as the LHC. Since WIMPs only interact very weakly they will leave the two multi-purpose detectors ATLAS and CMS without depositing any energy. Thus, the WIMP signature is missing energy transverse to the collision axis. WIMPs produced in the pair-production process $q\overline{q} \longrightarrow \chi\overline{\chi}$ would not leave any signal in the detector at all. Therefore, the primary channel to look for dark matter at hadron colliders is pair-production associated with initial (or final) state radiation

$$q\overline{q} \longrightarrow \chi\overline{\chi} + \text{X}.$$

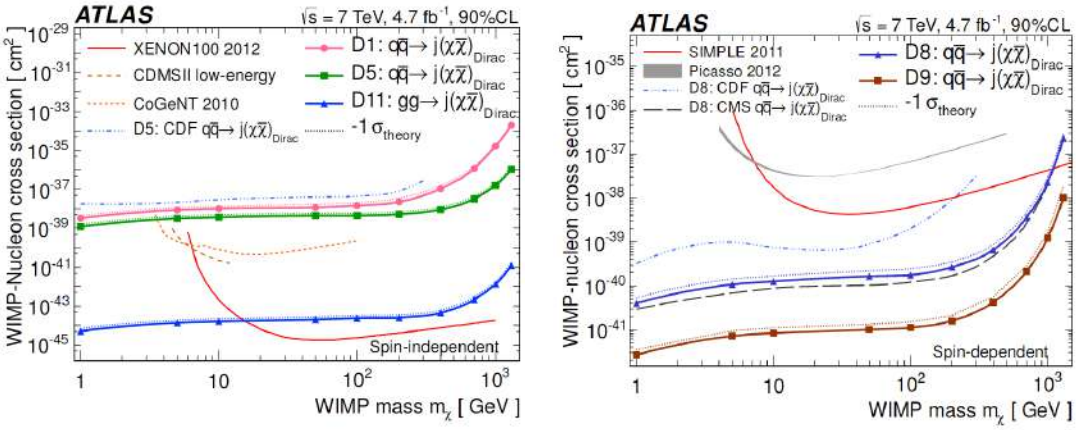

FIGURE 1.13: Inferred 90 % confidence level limits on spin-independent (left) and spin-dependent (right) WIMP-nucleon cross section from a mono-jet search of ATLAS. The solid lines labelled with D1–D11 correspond to different effective interaction operators. For comparison, 90 % CL limits from different direct detection experiments are shown. Figure from [71].

The additionally produced particle X can be a gamma, a Z- or W-boson, or a gluon. Such events can be selected by their missing energy plus a track or jet from a single particle. In figure 1.13 the result of a mono-jet analysis by the ATLAS collaboration is shown for SI WIMP-nucleon cross section and SD WIMP-nucleon cross section [71]. It can be seen that in case of SD interactions collider searches are much more competitive with direct detection experiments but somewhat model-dependent. The drop in sensitivity at larger WIMP masses is due to the fact that there is not enough energy available to produce the dark matter particles.

In 2012 the ATLAS collaboration announced the discovery of the Higgs particle at a mass of $m_H = 126\,\mathrm{GeV/c^2}$ [72]. If the Higgs particle couples strongly to WIMP particles (as expected by many models for WIMP masses smaller than $m_H/2 = 63\,\mathrm{GeV/c^2}$) the decay width of the Higgs would be affected [73]. Thus, constraints on the branching ratio of $BR(H \longrightarrow \text{invisible})$ can be derived, which can be translated into limits on the WIMP-nucleon cross section [74].

1.4 Revealing the dark within this thesis work

This thesis summarized my contributions to the XENON program, which is aiming for a direct detection of dark matter by means of dual phase liquid xenon time projection chambers (see chapter 2). In chapter 3, I discuss the final results on WIMP interactions from XENON100 [75], for which I studied the electronic recoil background and developed a background model for all three exposures of XENON100. I also conducted the first-ever search for dark matter-induced delayed coincidence signals in a dual phase xenon time projection chamber, which will be published in the near future. This analysis leads to an exclusion of the DAMA/LIBRA modulation signal as being due to magnetic inelastic dark matter at >90% confidence level and is discussed in chapter 4. For the XENON1T data acquisition system I developed a veto system, which will be discussed in chapter 5. This veto-system is currently installed and operational in XENON1T.

I also contributed significantly to the following publications and hardware work on XENON1T:

- For the study of dark matter sensitivity of multi-ton liquid xenon detectors [76] I determined the impact of the zero-field light yield L_y at $122\,\mathrm{keV_{ee}}$ on the electronic recoil background rejection by means of a simulation. The result of this simulation is shown in figure 3.5 of this thesis. I found that an increase of the light yield from $L_y = 4\,\mathrm{PE/keV_{ee}}$ (as realized by XENON100 [77]) to $L_y = 8\,\mathrm{PE/keV_{ee}}$ increases the background discrimination power by a factor ~ 4.
- An open source slow control system for small and medium scale project has been published in [78], which is currently operational in a low-background screening facility [79] and a R&D platform for cryogenic liquid xenon detectors. For this slow control system I developed a web application in order to display in real time the monitored parameters. Furthermore, the display allows to brows, plot and download older data, stored on a SQL database.
- During the installation of XENON1T I contributed to the cleaning campaign of all detector parts in order to minimize radioactive contamination on their surface. Depending on the material, different elaborate cleaning procedures have been applied. In case of copper for example the components have been cleaned in an ultrasonic bath and afterwards immersed in acetone. Subsequently all copper parts have been etched in nitric and hydrofluric acid and passivated in citric acid.
- In order to keep the liquid xenon in XENON1T at a precise level, a diving bell design was chosen (similar to XENON100 [77]). The height of the liquid level can be adjusted by vertically moving a small pipe inside the detector (which releases the pressure inside the bell) attached to a motion feedthrough on top of the cryostat. I developed a system allowing to operate this feedthrough from outside the water tank, while preventing any direct line of sight to the detector without water shield.

Chapter 2

The XENON dark matter detectors

The XENON collaboration aims for the direct detection of dark matter using dual phase time projection chambers (TPCs) filled with cryogenic liquid xenon. Above WIMP masses of ~5 GeV this detector design has been proven to be the most sensitive since years and is used in several experiments all around the world (XENON [[54, 75], LUX [80], LZ [81], Panda-X [53]). The working principle of the XENON dark matter detector is introduced in section 2.1, the xenon target properties are described in section 2.2 and the detectors XENON100 and XENON1T are introduced in section 2.3.

2.1 The XENON detector principle

The working principle of the XENON dual phase TPC is based on a cylindrical volume filled with liquid xenon. It is instrumented with light sensors, usually photomultiplier tubes (PMT), arranged in two arrays, one located in the liquid at the bottom of the volume and one in the gas phase above the liquid. A uniform electric field (~500 V/cm) is applied across the liquid volume. Whenever a particle interacts inside the liquid xenon it produces scintillation light and free electrons through ionization. More details on this processes can be found in section 2.2. The prompt scintillation signal (S1) is directly detected by the PMT arrays and serves as time zero (t_0) of the interaction. Due to the electric field the free electrons drift towards the anode at the top of the TPC with a constant drift velocity (~1.7 mm/μs for XENON100 [77], depending on the drift field [82]). Once they reach the liquid surface they are extracted into the gas phase by a strong electric field (~10 kV/cm) established across the liquid-gas interface. This is illustrated in figure 2.1 (left). The electric fields inside the TPC are created by means

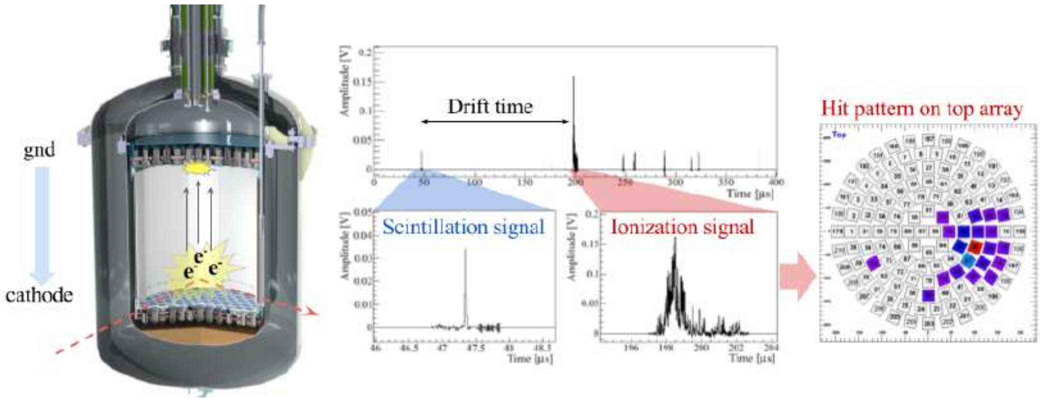

FIGURE 2.1: **(left)** Illustration a particle interaction in XENON1T producing prompt scintillation light and ionization electrons. Due to a uniform electric field the electrons drift towards the top of the TPC where they create proportional scintillation light. **(middle)** Exemplary waveform (from XENON100) of an interaction showing the scintillation (S1) and ionization signal (S2) separated by the drift time which defines the depth (z-position) of the interaction. **(right)** Hit pattern of top PMT array from which the x-y position of the event is derived.

of a stack of thin metal meshes. The drift field is produced between the cathode at negative potential located at the bottom of the TPC and the grounded gate grid 2.5 mm below the liquid surface. The stronger extraction field is created between the gate and the anode 2.5 mm above the liquid surface. In addition both PMT arrays are protected by two screening meshes located between cathode (anode) and PMT array.

Once in the gas phase the electric field accelerates them to energies high enough to produce scintillation light, which is proportional to the number of primary electrons (called S2 signal). The proportional scintillation light is again measured by the two PMT arrays. The ratio of ionization and scintillation signal is different depending on the interacting particle, which makes it possible to discriminate between backgrounds induced by γ- and β-radiation, and interactions induced by WIMPs [83].

The position of the electron cloud extracted into the gas phase is very localized. Thus, the x-y position of the interaction is measured from the S2 hit pattern on the pixelized top PMT array (see figure 2.1 right). The depth of the interaction (z position) is derived from the projection of the drift time (time difference between S1 and S2), shown in figure 2.1 (middle), using the known drift velocity, which is why these types of detectors are called time projection chambers. The three-dimensional position is used in order to select a fiducial volume in the center of the detector. This volume is shielded from external γ and β background radiation by the surrounding target material itself and thus an especially low background level can be achieved in this region. The fiducial volume is optimized in the course of the analysis based on the level of background to achieve maximum sensitivity. Knowing the position of an event also makes it possible to reject double scatter interactions originating from Compton-scattering γ-radiation or neutrons.

Property	Value
Atomic number	54
Molar mass	$131.29\,\mathrm{mol}^{-1}$
Isotropic abundances	^{124}Xe (0.095 %), ^{126}Xe (0.089 %), ^{128}Xe (1.91 %) ^{129}Xe (26.4 %), ^{130}Xe (4.07 %), ^{131}Xe (21.2 %) ^{132}Xe (26.9 %), ^{134}Xe (10.4 %), ^{136}Xe (8.86 %)
Melting point (at 1 atm)	161.4 K
Boiling point (at 1 atm)	165.1 K
Gas density	5.894 g/l
Liquid density	$3.057\,\mathrm{g/cm^3}$
Heat conductivity (gas, 273 K, 1 atm)	5.192 mW/(m·K)
Heat conductivity (liquid, 178 K, 1 atm)	71.1 mW/(m·K)
Relative permittivity (gas), ϵ_r	1.00
Relative permittivity (liquid), ϵ_r	1.96
Dielectric strength	$\gtrsim 400\,\mathrm{kV/cm}$
Average energy to form an e$^-$-ion pair (W_i)	15.6 eV
Maximum scintillation yield (W_{ph})	13.8 eV
Scintillation wavelength	178 nm

TABLE 2.1: Collection of physical properties of xenon. Numbers taken from [85].

2.2 Liquid xenon for dark matter detection

Xenon is present in the earth's atmosphere at a level of ~ 0.1 ppm and is the heaviest stable element of the noble gases. It basically does not have any long living radioactive isotopes with the exception of ^{136}Xe, which has a half-life of 2×10^{21} y and decays via two neutrino double beta decay. This background will become relevant for future large scale detectors such as DARWIN [84]. Apart from ^{136}Xe, xenon has essentially no intrinsic radioactivity coming from naturally occurring isotopes, which makes it ideal for rare event searches. Moreover, it has excellent electronic stopping power, as discussed in more details below, allowing the central part of the detector to be shielded against external background. Finally, the isotopes ^{129}Xe and ^{131}Xe have a non-zero nuclear spin which makes xenon also sensitive to spin-dependent interactions.

In order to measure radiation in a detector, its ability to transform the absorbed energy into detectable signals is very important. In the case of liquid xenon (LXe) scintillation photons and ionization electrons are produced with very high efficiency. The properties of xenon are summarized in table 2.1.

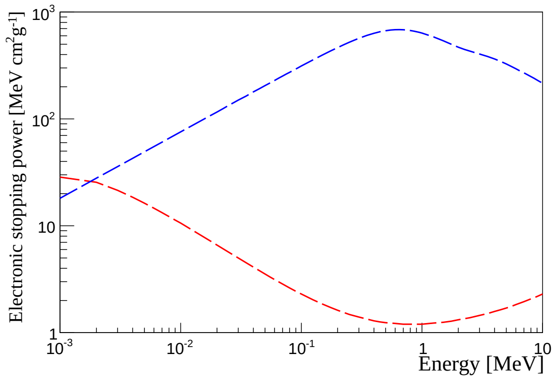

FIGURE 2.2: Electronic stopping power for electrons (red) and alpha particles (blue) in xenon. At energies smaller than 100 keV the track length is of the order of $\mathcal{O}(\mu\mathrm{m})$. Data from [89].

2.2.1 Energy deposition in liquid xenon

The discussion presented in this section is mainly following [29, 85–87]. When interacting with xenon, incoming charged particles lose energy via collisions with the atomic electrons and with the nuclei. In this process the xenon gets excited and ionized, which leaves free electrons and ions along the particle track. Electrons and α particles mainly lose their energy through inelastic collisions with electrons from the atomic shell, producing excitation and ionization. On the other hand, WIMPs (or low energy neutrons) are expected to interact with xenon via elastic scattering with a nucleus. In addition to electronic excitation, the recoiling nucleus loses a substantial amount of energy through elastic collisions with other nuclei, leading to a smaller detectable signal. This process is called nuclear quenching. The excited atoms generated in the process of electronic excitation form exited dimers (Xe_2^*), which decay and emit scintillation light of 178 nm wavelength. Ionization electrons and ions recombine and form excited dimers too, unless an external electric field is applied which separates and prevents them from recombination. For LXe the average energy required to form an electron-ion pair is $W_i = 15.6\,\mathrm{eV}$ and the maximum scintillation yield is estimated to be $W_{\mathrm{ph}}(\mathrm{max}) = (13.8 \pm 0.9)\,\mathrm{eV}$ [88] which is the average energy to produce a scintillation photon.

Figure 2.2 shows the stopping power of xenon for electrons and α particles. At energies of $< 100\,\mathrm{keV}$ the track length of electronic recoils and alpha particles in LXe are $\mathcal{O}(\mu\mathrm{m})$ and thus external α and β emitters do not contribute to the background inside the fiducial volume in the center of the detector. This property is often referred to as the self-shielding of xenon since due to its high stopping power the target shields itself from external radiation.

2.2.2 γ and neutron interactions

Depending on their energy, photons interact with matter through photoelectric absorption, Compton scattering or pair production. These interactions produce energetic electrons that will lose their energy through excitation and ionization. As can be seen in figure 2.3 at energies below 300 keV photoelectric absorption is dominant while above 300 keV Compton scattering becomes more likely. At energies below $\sim$ 100 keV the attenuation length for γ radiation is very small ($\sim$ 1 mm) and thus most photons at this energy will be absorbed by the outer LXe layer. The attenuation length becomes reasonably large ($\sim$ 6 cm) only at higher energies ($\sim$ 1 MeV), allowing the photon to penetrate into the fiducial volume of the detector. Thus, the dominant background is electronic recoils from single Compton scattering leaving low energy signals. Multiple scatter events are suppressed because they are rejected in the analysis.

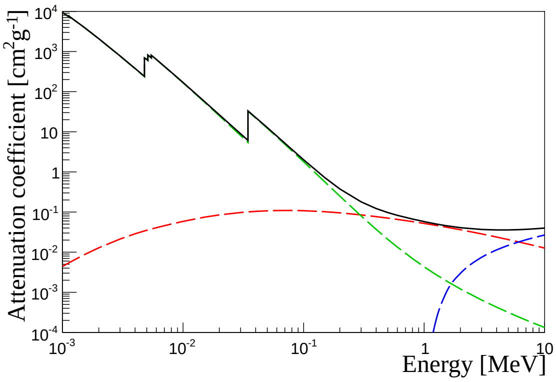

FIGURE 2.3: Total attenuation coefficient of γ-rays (solid black), for Compton scattering (red dashed), photoelectric absorption (green dashed) and pair production (blue dashed) in xenon as a function of the energy. Data from [90].

At energies below 1 MeV neutrons mainly interact with xenon via elastic scattering off a nucleus. These interactions produce recoiling nuclei that again lose their energy through excitation and ionization as well as through elastic collisions with other nuclei. At energies $>$ 1 MeV inelastic scattering starts to play a role, which leaves the nucleus in an excited state decaying with the emission of a γ-ray. Usually, these excited states are short lived ($\lesssim$ 1 ns). However, in the case of ^{129}Xe and ^{131}Xe there are meta-stable excited states with half-lifes of several days. The most dangerous irreducible background for the search of dark matter comes from elastic neutron interactions since they mimic the expected signal coming from a WIMP. Thus, detector materials have to be chosen very carefully in order to minimize their neutron production due to (α, n) reactions or spontaneous fission. In larger LXe TPCs, such as XENON1T with a dimension of $\sim$ 1 m, the possibility of rejecting neutrons due to double scatter interactions will become more powerful as their mean free path is $\mathcal{O}$(10 cm) at $\sim$ 1 MeV.

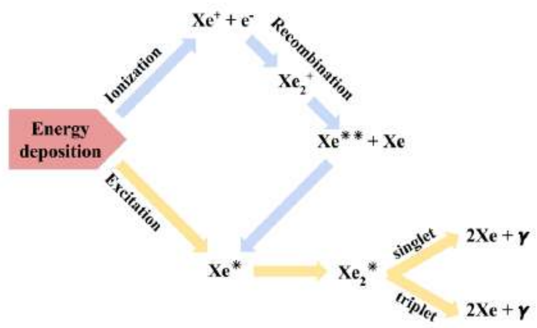

FIGURE 2.4: The generation process of scintillation light in xenon. Scintillation light can be produced directly through excitation of the xenon atoms or through ionization and subsequent recombination, leading to excitons and eventually to scintillation light.

2.2.3 Scintillation signal

A recoiling electron or Xe nucleus will create excited Xe atoms, "excitons" Xe^*, and electron-ion pairs, $\mathrm{Xe}^+ + e^-$. These excitons can form excimers Xe_2^* by colliding with neighbouring Xe atoms which subsequently decay to their ground state with the emission of a scintillation photon. With no electric field applied, the electron-ion pairs will recombine and eventually again form excitons and thus also produce scintillation light. The scintillation spectrum of xenon is centred at around 178 nm with a width of 13 nm [91]. It has two components, from the de-excitation of the singlet and the triplet state, with decay times of $\sim$ 3 ns and $\sim$ 27 ns, respectively, which makes xenon one of the fastest scintillators. In the absence of an electric field the recombination time constant dominates and a decay time of 45 ns is observed [92]. The process to generate scintillation light in xenon is illustrated in figure 2.4. The number of photons produced per unit energy, the scintillation yield, depends on the type of interacting particle as well as the interaction energy. There are various effects affecting the production of photons. Low-density ionization tracks, for example, might have a reduced scintillation yield due to escape electrons which will no longer undergo recombination. In the case of nuclear recoils the scintillation yield is reduced by nuclear quenching due to energy lost to atomic motion. An electric field reduces the scintillation yield by separating the electron-ion pairs and thus reducing the recombination fraction (called "field quenching"). Conventionally the relative scintillation efficiency, L_{eff}, of nuclear recoils is used in order to define a nuclear recoil energy scale (see section 2.2.5). It is defined as the ratio of the energy dependent scintillation yield, L_y, of nuclear recoils to that of electronic recoils at a fixed energy of 122 keV, which corresponds to the full absorption of the 122 keV γ rays from ^{57}Co:

$$L_{\mathrm{eff}}(E_{\mathrm{nr}}) = \frac{L_{\mathrm{y,nr}}(E_{\mathrm{nr}})}{L_{\mathrm{y,ee}}(E_{\mathrm{ee}} = 122\,\mathrm{keV})}. \tag{2.1}$$

E_{nr} refers to the nuclear recoil and E_{ee} to the electronic recoil energy. The precise measurement of the relative scintillation efficiency L_{eff} is the subject of ongoing research. In figure 2.5 a recent measurement by the LUX collaboration is shown [93]. In this

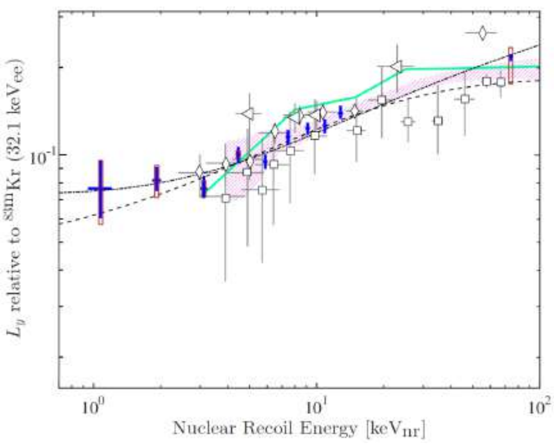

FIGURE 2.5: Light yield of nuclear recoils relative to that of electronic recoils at an energy of 32.1 keV at zero field measured by LUX (blue points). The gray data points are from [96] (◁), [97] (□) and [98] (◊). The cyan line [95] and the purple band [99] are measurements based on a spectral fits. The dashed (dot-dashed) black line corresponds to the Lindhard-based [100] (Bezrukov-based [101]) NEST model [102] fitet to the blue data points. Figure adapted from [93].

measurement the scintillation yield is presented relative to the 32.1 keV line of ^{83m}Kr instead of ^{57}Co. This newer energy standard can be dissolved in xenon and thus be used to calibrate the fiducial volume [94]. The solid cyan line shows the previous measurement of L_{eff} by XENON100 [95] based on a spectral fit of AmBe neutron calibration data. The applied electric field in LXe TPCs reduces the fraction of recombining electrons, and thus the scintillation signal. This effect is taken into account in the energy reconstruction by the energy independent field quenching factors $S_{\mathrm{nr}}(E)$ and $S_{\mathrm{er}}(E)$ where E represents the electric field. For the XENON100 drift field of 530 V/cm [77] they are $S_{\mathrm{nr}}(530\,\mathrm{V/cm}) = 0.95$ and $S_{\mathrm{er}}(530\,\mathrm{V/cm}) = 0.58$ [83].

2.2.4 Ionization signal

The second excitation channel measured by LXe TPCs is the ionization signal. An ionizing particle creates electron-ion pairs along its path through the xenon. In order to prevent free electrons from recombining, an external electric field is applied to separate them from the positively charged ions. Due to the electric field, electrons that escaped recombination drift towards the anode with a drift velocity of $v_d = 1.73\,\mathrm{mm}/\mu\mathrm{s}$ at 530 V/cm in XENON100 [77]. However, electronegative impurities, such as O_2 and water, might capture the drifting electrons and form negatively charged ions with much lower mobility and thus lead to a decreased ionization signal. The mean lifetime of an electron before it gets attached to an impurity is called electron lifetime τ_e and the number of electrons surviving after drifting for a certain distance $z = v_d \cdot t$ is following an exponential with the time constant τ_e. Therefore, impurities need to be reduced as much as possible in order to increase the electron lifetime. At the surface of the liquid volume a high electric field (several kV/cm) is applied between the gate, placed inside the liquid and the anode in the gas phase. This causes the drifting electrons to be extracted into the gas phase where their collisions with Xe atoms create scintillation light. This process is called electroluminescence or proportional scintillation as the amount of light is proportional to the initial number of electrons. The proportional scintillation light is measured by the top and bottom PMT arrays. Due to this highly efficient way of amplifying the ionization signal it is possible to detect single electrons [103, 104].

Different types of particles leave ionization tracks with different densities and thus are affected differently by the presence of an external electric field. This affects the recombination process, leading to different light to charge ratios for different particles. The complete mechanism of how the energy deposited by an ionizing particle is distributed between the scintillation and ionization channel is still not fully understood. The recombination model in [105] is able to predict the mean of the ER and NR bands but not their width. Nevertheless, it is experimentally verified that the ratio between the scintillation and ionization signal depends on the type of interaction. As shown for the first time in [83], this results in a lower charge/light ratio for nuclear recoils (NR) compared to electronic recoils (ER). Using this parameter it is possible to discriminate between ERs, induced by γ and β backgrounds, and NRs. In XENON100 a rejection level of 99.75 % while keeping a nuclear recoil acceptance of > 30 % has been achieved (see section 3.3.1). This discrimination power can be increased for example by increasing the light yield L_y as shown in [76]. In ZEPLIN-III for example a discrimination power of 99.98 % has already been achieved with a NR acceptance of ~ 50 % [106]. In figure 2.6 the response of XENON100 to ERs (black points) and NRs (red points) is shown. The separation between the two bands is clearly visible. As reported in [83], the separation between the two bands improves with increasing electric field and decreasing interaction energy. The dependency on the electric field is shown in figure 2.7, which shows the light and charge yields for ER and NR. It can be seen that the charge to light ratio of ERs changes a lot with increasing field while for NRs it stays almost constant.

2.2.5 Energy scales for nuclear and electronic recoils

In order to measure the energy of an interaction it is necessary to define and calibrate an energy scale. NRs and ERs will leave different signatures in the detector and thus need their own energy scales, the ER equivalent energy scale (referred to as E_{ee}) and the NR equivalent energy scale (referred to as E_{nr}). Traditionally, the energy scale is based on the scintillation light. The E_{nr} scale is defined by

$$E_{\mathrm{nr}} = \frac{S1}{L_y} \frac{1}{L_{\mathrm{eff}}} \frac{S_{\mathrm{er}}}{S_{\mathrm{nr}}}, \tag{2.2}$$

where L_y is the light yield from 122 keV γ-rays, which are calibrated in each detector individually, and L_{eff} is the relative scintillation yield for nuclear recoils previously

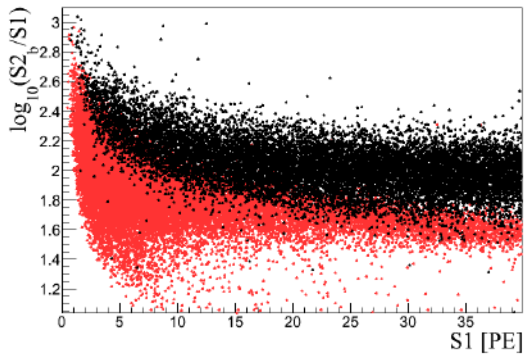

FIGURE 2.6: Electronic recoil band (black) and nuclear recoil band (red) from XENON100. A clear separation of the two bands can be seen.

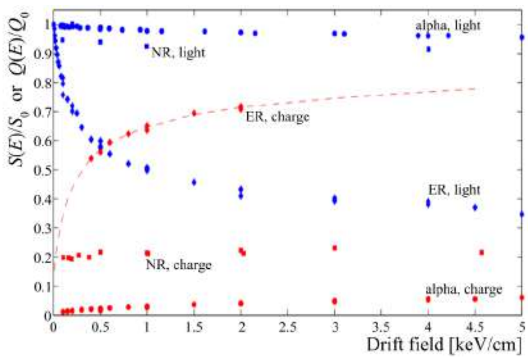

FIGURE 2.7: Field dependence of scintillation and ionization yield in liquid xenon for 122 keV electronic recoils, 56 keV nuclear recoils and alpha paritcles. The relative light yield $S(E)/S_0$ is the light yield relative to that at zero field S_0. The relative charge yield $Q(E)/Q_0$ is the charge collected relative to that at infinite field Q_0 (i.e., without recombination). Figure from [83].

discussed in section 2.2.3. S_{er} and S_{nr} are the scintillation field quenching factors and depend on the applied drift field. The ER equivalent energy scale based on the scintillation signal (S1) is defined as

$$E_{\mathrm{ee}} = \frac{S1}{f} \frac{1}{R(E)} \frac{1}{Q(E)} \tag{2.3}$$

where $R(E)$ is the energy dependent scintillation efficiency relative to the efficiency at an energy of 32.1 keV (^{83m}Kr) at zero drift field. A measurement of $R(E)$ can be found for example in [107]. $Q(E)$ defines the energy dependent quenching factor for a non zero field for ER interactions, measured as well in [107]. The factor f is the light yield at 32.1 keV and zero field, determined in each detector. The relative scintillation efficiency $R(E)$ and the quenching factor $Q(E)$ can be described by the semy analytical “Noble Element Simulation Technique” (NEST) model [108] which uses experimental inputs like the one from [107] and [109].

It is also possible to define a nuclear recoil equivalent energy scale based on the charge signal (S2), which is used in [87] since this allows to lower the energy threshold. The conversion from measured S2 signals into units of keV is given by

$$E_{\mathrm{nr}} = \frac{S2}{Y} \frac{1}{Q_y}, \tag{2.4}$$

where Y is the detector dependent secondary scintillation gain, which gives the number of photoelectrons detected per electron. Q_y is the energy dependent charge yield, which defines the number of electrons per keV deposited in the interaction.

Finally, it is also possible to determine an energy scale based on both the scintillation and the charge signals by using the linear combination of the two [77]. As the fluctuations of the S1 and S2 signals are anti-correlated due to the signal generating process, such a linear combination will result in an increased energy resolution. Although this anti-correlation has been measured for high energy γ-lines [110], it has yet to be observed for low energy nuclear recoils.

The measured S1 and S2 signals are derived by summing up the signal of all PMTs corrected for their different gain. They are both measured in units of detected photo-electrons (PE), which is the amount of observed signal resulting from a single electron ejected from the photocathode. The S1 signal is further corrected based on the position dependent light collection efficiency, hereinafter referred to as cS1. Similarly, the S2 signal is corrected for position dependent effects in the signal detection as well as for the finite electron lifetime, which is called cS2 [111].

2.3 The XENON detectors

One of the big advantages of LXe dual phase TPCs is their scalability to larger dimensions. This allowed a successive increase in target mass (and thus sensitivity) for the increments of the XENON program, from XENON10 (15 kg target), XENON100 (62 kg target) to XENON1T (2 ton target). In this section XENON100 and XENON1T are introduced and their background sources are discussed in more detail.

2.3.1 XENON100

XENON100 [77] is located at the underground laboratory *Laboratori Nazionali del Gran Sasso* (LNGS) in Italy at a depth of 3600 m water equivalent, which results in a reduction of the muon flux by a factor of 10^6 compared to the surface [112]. The goals of this detector were to increase the target mass by a factor of ten with respect to its predecessor, XENON10 [113], and to lower the background by two orders of magnitude. The cylindrical TPC with a height of 30.5 cm and a radius of 15.3 cm contains a target mass of 62 kg LXe. This volume is optically separated from the surrounding LXe by polytetrafluorethylen (PTFE) panels. PTFE is used due to its high reflectivity for the vacuum ultraviolet (VUV) scintillation light of xenon centred around 178 nm. In order to keep the liquid at a constant level, a diving bell design has been developed, where liquid level can be controlled by means of the pressure inside the bell. This design allows filling of the cryostat to a height above the bell and thus a LXe shield is present all around the TPC. The sensitive volume is viewed with two arrays of Hamamatsu R8520-06-Al 1" cube PMTs, above (98 PMTs) and below (80 PMTs) the target. The top array is

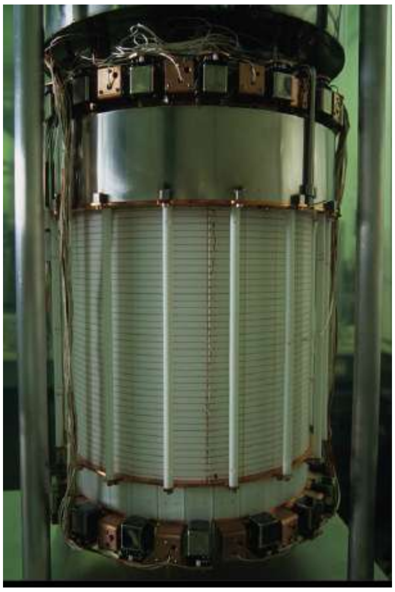

FIGURE 2.8: Picture of the XENON100 TPC. On top and on the bottom the veto PMTs can be seen, separated from the active target volume by the PTFE panels.

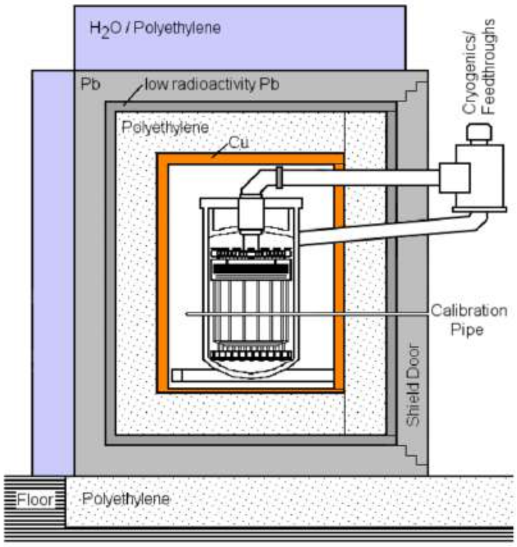

FIGURE 2.9: Drawing of the XENON100 detector. The TPC is inside a double-walled stainless steel cryostat and surrounded by several layers of passive shielding made out of copper, polyethylene, lead and water. Figure from [77].

arranged in concentric rings in order to improve the radial position reconstruction. On the bottom array, the PMTs are packed as densely as possible in order to maximize the sensitive area. The volume outside the TPC is instrumented with 64 PMTs of the same model. This volume contains 99 kg of LXe and serves as an active veto in order to tag multiple scatter events that interact once in the veto and once inside the TPC. A picture of the TPC is shown in figure 2.8, in which the veto PMTs can be seen above and below the TPC, separated from the active target volume by the PTFE panels.

The drift field in XENON100 is generated by thin stainless steel meshes at the bottom and the top of the TPC. The cathode is located above the bottom PMTs, which are shielded from the electric field by an additional screening mesh at ground potential. The 17 mm thick layer between this mesh and the cathode is charge insensitive, which results in an incomplete charge readout for double scatter events scattering once in this region and once inside the TPC. In such a topology only one S2 peak is detected, resulting in a fake single scatter event with a decreased S2 over S1 ratio. Thus these events represent a dangerous background, since they might leak into the NR region (called “gamma-X” events). The top of the TPC features a grounded mesh (gate) 2.5 mm below the liquid surface and the anode 2.5 mm above the liquid surface. The high electric field between these two meshes ($\sim 12\,\mathrm{kV/cm}$) is used to extract the drifting electrons into the gas phase where they produce the S2 signal. The top PMT array is also protected by a screening mesh at ground potential. Field shaping rings made out of copper wires ensure a homogeneous drift field of 530 V/cm. The electron drift velocity of 1.73 mm/μs and the dimensions of XENON100 lead to a maximum drift time of $\sim$ 178 μs.

In order to shield the experiment from external radiation, XENON100 is surrounded by a passive shield consisting of 5 cm of copper, 20 cm of polyethylene, and 20 cm of lead. The experiment rests on a 25 cm thick plate of polyethylene and a water/polyethylene layer encloses the top and three sides of the detector. A drawing of XENON100 and its passive shield is shown in figure 2.9. The xenon is liquefied by a pulse tube refrigerator (PTR) and is constantly purified from electronegative impurities using a high temperature getter. The cryogenic system is located outside the shielding in order to avoid introducing background inside the TPC. A detailed description of XENON100 can be found in [77].

XENON100 acquired its last dark matter search data in 2014, collecting a total of 477 live days of dark matter data over its lifetime. This data, spread over 4 years, led to a plethora of publications. Among them the final result from XENON100 on the spin independent WIMP-nucleon and the spin dependent WIMP-neutron/proton cross section, which will be discussed in chapter 3. This result confirms the absence of a WIMP dark matter signal. Furthermore, the first search for dark matter-induced delayed coincidence signal has been performed on science run II and is discussed in chapter 4.

2.3.2 XENON1T

XENON1T was designed to significantly increase sensitivity to WIMP-nucleus interactions beyond the current best limits. Like XENON100, XENON1T is located at LNGS in Italy. The target sensitivity of XENON1T to spin-independent WIMP-nucleon interactions is two orders of magnitude below the one achieved by XENON100 [54]. This goal is to be achieved by increasing the target mass by a factor of 32 as well as by lowering the background rate by a factor of $\sim$ 100.

The basic design of XENON1T is similar to that of XENON100. The cylindrical TPC has a height and a diameter of 96 cm and contains a target mass of $\sim$ 2 t of LXe. The fiducial mass is expected to be $\sim$ 1 t, depending on the background level, and the total mass inside the detector is about 3.2 t. Generation of the electric drift field inside the TPC follows the same basic design as in XENON100, including two linear grids (cathode and screening) on the bottom and three etched, hexagonal meshes (gate, anode and screening mesh) on the top of the TPC. The field uniformity is ensured by a stack of 74 field shaping rings made out of copper with each ring kept at a different electric potential. In figure 2.10 the TPC with its copper rings can be seen during underground installation. The electric drift field in XENON1T is currently kept at

Figure 2.10: XENON1T TPC during underground installation inside the water shield. The stack of copper field shaping rings are held together by PTFE holders (white vertical bars). The panels separating the TPC from the surrounding LXe volume are inside the copper rings and thus not visible.

$\sim 125\,\mathrm{V/cm}$, below the design goal, resulting in a maximum drift time of $\sim 650\,\mu$s. The target volume is separated from the surrounding LXe using interlocking PTFE panels. However, in contrast to XENON100, these panels are installed on the inside of the field shaping rings. The reason for this is to minimize metal surfaces inside the TPC, since they have been found to be the origin of photo-ionization after S2 peaks [103], and to increase the light yield. XENON1T is also equipped with two arrays of PMTs, one on the top and one on the bottom, consisting of 248 Hamamatsu R11410-21 3" PMTs [114]. Similarly to XENON100, the top array is arranged in concentric rings and the bottom array is packed as dense as possible in order to maximize the geometric coverage. The LXe shield outside the field shaping rings is equipped with six diagnostic PMTs (Hamamatsu R8520-06-Al 1"), located at two positions around the TPC. The height of the liquid level inside the target volume is again controlled by a diving bell design where the desired liquid level can be adjusted by moving the height of a bleeding tube for the xenon gas.

In order to protect the detector from external radiation, XENON1T is located inside a water tank of $\sim 10\,\mathrm{m}$ height and diameter, shown in the drawing of figure 2.11. The water tank is instrumented by 80 8" Hamamatsu R5912ASSY PMTs and serves as a Cherenkov detector in order to identify muons, and with a lower efficiency also hadronic showers, and thereby reduce the muon-induced neutron background inside a 1 ton fiducial volume to 0.01 event/year [115]. XENON1T can be calibrated using external sources (AmBe, ^{137}Cs) located in a mobile collimator inside the water tank as well as using a neutron generator in order to calibrate the NR band. In addition, internal sources, such as ^{220}Rn [116] and ^{83m}Kr can be used for ER calibration. The liquefaction and purification of the xenon is performed by means of two redundant PTRs to cool the xenon, two parallel

FIGURE 2.11: Picture of the XENON1T water shield, serving as Cherenkov muon veto. The cryostat, containing the TPC, is located in the middle of the water tank, shielded from external radiation. The service building on the right contains the xenon storage and the distillation column on the ground floor, the data acquisition on the middle floor and the cryogenic system on the top floor.

high-temperature getters to purify the xenon gas from electronegative impurities and a cryogenic distillation column in order to remove the radioactive ^{85}Kr. Furthermore, a storage system (ReStoX) has been developed which is able to contain all the xenon, either in liquid or in gas phase. A summary of the main differences between XENON100 and XENON1T is shown in table 2.2.

	TPC dimension	**Total mass**	**Active mass**	**Fiducial mass**	**Shield**	**Light sensors**
XENON100	30 cm	161 kg	62 kg	34–48 kg	passive lead PTFE and copper shield	178 1" PMTs (R8520) +64 veto 1" PMTs
XENON1T	96 cm	$\sim$3.2 t	2 t	$\sim$1 t	active water shield working as muon veto	248 3" PMTs (R11410-21) +6 diagnostic 1" PMTs
XENONnT	$\sim$ 1.4 m	$\sim$ 7 t	$\sim$ 5.7 t	4-5 t	active water shield working as muon veto	$\sim$ 450 3" PMTs (R11410-21)

TABLE 2.2: Main parameters of XENON100, XENON1T and XENONnT.

2.3.3 XENONnT

XENON1T is expected to take data for $\sim$ 2 years, resulting in a total exposure of 2 tons$\times$years. A subsequent upgrade to XENONnT is already in planning. Most of the sub-systems used for XENON1T have been designed in order to serve as well for XENONnT. The idea is to replace the TPC by a larger one while reusing the existing

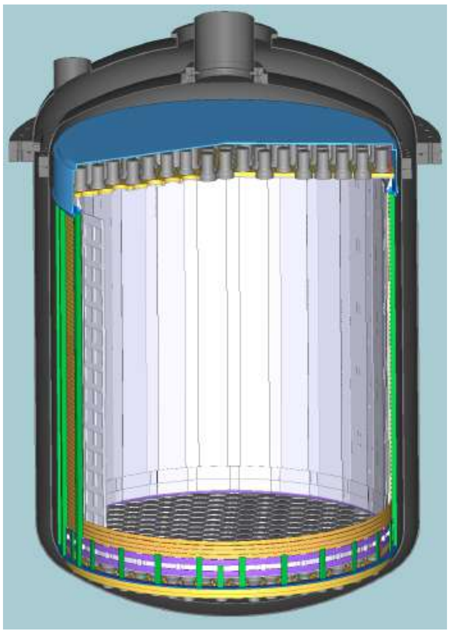

FIGURE 2.12: Drawing of the XENONnT inside the same outer cryostat as used for XENON1T. This TPC with a dimension of $\sim$ 1.4 m will contain a total active target of $\sim$ 5.7 t of liquid xenon and will be instrumented by $\sim$ 450 PMTs.

infrastructure such as the outer cryostat, support structure, calibration system, water shield, xenon storage and the service building as well as the scalable DAQ system and the slow control. XENONnT will contain a total mass of $\sim$ 7 t of LXe and a target mass of $\sim$ 5.7 t. It will be instrumented by $\sim$ 450 Hamamamtsu 3” R11410-21 PMTs. A drawing of the XENONnT TPC is shown in figure 2.12. The additional high voltage and signal cables needed for the increased number of PMTs are already installed inside the “umbilical pipe”, which connects the cryostat to the service building. The aim of XENONnT is to improve the sensitivity to spin-independent WIMP-nucleon interactions by another order of magnitude with respect to XENON1T with minimum of $1.6 \times 10^{-48}\,\mathrm{cm}^2$ [54], or to probe an eventual WIMP signal with higher statistics.

2.3.4 Backgrounds in XENON

For direct dark matter detectors and rare event searches in general it is important to reduce the background as much as possible. XENON100 and XENON1T are located at the underground laboratory LNGS in Italy in order to shield the experiments from cosmic radiation. With a rock overburden of 1.4 km (3600 m water equivalent) the muon flux is reduced by a factor of 10^6 compared to the surface [112]. In addition, external background radiation originating from the surrounding rock and from radioactive isotopes in the air, as well as internal background from detector materials or impurities inside the xenon itself, must be suppressed.

External background is reduced by enclosing the detector in a shield. In case of XENON100 this shield is built out of copper, PTFE and lead. In XENON1T external background is

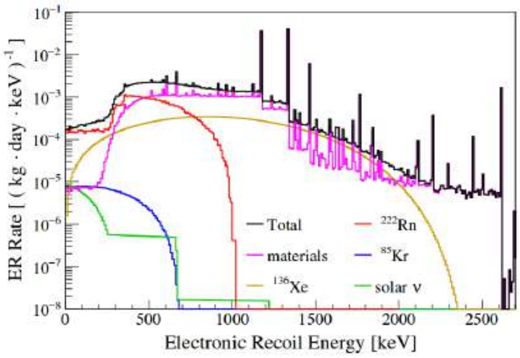

FIGURE 2.13: Energy spectrum of the total ER background rate in the 1 t fiducial volume (black), and the separate contributions from detector components (purple), 10 μBq/kg of ^{222}Rn (red), 0.2 ppt of $^{\mathrm{nat}}$Kr (blue), solar neutrinos (green) and ^{136}Xe double-beta decay (brown). Figure from [54].

reduced by a water shield with a diameter and a height of ~10 m. As described above, this water tank is equipped with PMTs and serves as a water Cherenkov detector, which allows to tag the remaining muons with an efficiency of $> 99.5\,\%$ and their showers from interactions in the rock with an efficiency of $> 70\,\%$. The prediction for the remaining background from muon-induced neutrons is 0.01 event per year [115].

A background component that cannot be reduced by the shield is the radiation of the detector materials themselves. The purple line in figure 2.13 showns the contribution of detector materials to the total ER background in XENON1T. In order to prevent this type of background the detectors are exclusively built out of carefully selected, radio pure materials such as copper, PTFE and stainless steel [117]. The selection of these materials is based on extensive measurements of their activity in dedicated screening facilities [79, 118, 119]. Furthermore, before installation, all parts are carefully cleaned and, e.g., in the case of copper and stainless steel, chemically treated in order remove the outermost layer and thereby possible surface contaminations. As γ and β radiation from the detector materials will mainly interact in the outermost layer of the detector, fiducialization further helps to suppress this source of background. Due to their longer mean free path of $\mathcal{O}(10\,\mathrm{cm})$, fiducialization is less effective for neutron background.

Finally, there is the contribution from intrinsic background coming from impurities inside the liquid xenon such as ^{222}Rn and ^{85}Kr. The radioactive ^{85}Kr is present in natural krypton with a relative isotopic abundance of $2 \cdot 10^{-11}$ and is present because xenon is extracted from the atmosphere. In order to reduce the krypton content (and thereby the ^{85}Kr concentration) the xenon for XENON1T is processed in a cryogenic distillation column [120], achieving a reduction factor of $6.4{\cdot}10^5$. ^{222}Rn is part of the ^{238}U decay chain and emanates from all detector surfaces. In order to reduce background originating from ^{222}Rn and its daughters low-emanation detector materials are selected. Recent XENON R&D showed that online removal of the Rn using cryogenic distillation is possible [121]. The contributions from ^{85}Kr and ^{222}Rn to the total ER background in XENON1T are shown in figure 2.13. It can be seen that in XENON1T, ^{222}Rn will be the dominant background at low energies [54].

In the course of the analysis it is mandatory to develop a prediction of the remaining background. Such a background model is used, for example, as an input for a profile likelihood analysis. In chapter 3 a background model for all three runs of XENON100 is developed. These models are used for the final result of XENON100, comprising a total of 477 days of data.

Chapter 3

Final results on WIMP interactions from XENON100

During the successful XENON100 physics program three long dark matter exposures have been acquired with a total live time of 477 days. Besides the conventional limits on the spin independent (SI) and spin dependent (SD) WIMP interactions [86, 122–124] several additional analyses based on the second science run have been published. Among them are the search for an event rate modulation [125] and the test of leptophilic dark matter models [126], which both exclude the modulation signal measured by DAMA/LIBRA [127] interpreted as being due to DM-electron scattering. Furthermore, there were publications on searches for axions and axion-like particles [29], a search for double electron capture of ^{124}Xe [128] and a search for magnetic inelastic dark matter. The latter will be discussed in detail in Chapter 4. A recent publication combines all three dark matter runs, with a total exposure of $\sim 17.6\,\text{tons} \times \text{days}$. It leads to the experiment's most stringent limits on the SI WIMP-nucleon and the SD WIMP-neutron and WIMP-proton cross section. This chapter describes the in-depth details of the background model used for the re-analysis of run I and II as well as for the analysis of run III. The data selection for the combined analysis of all three science runs is discussed in section 3.2. In section 3.3 the possibilities to reduce the background and possible sources of remaining background are discussed. Sections 3.4, 3.5 and 3.6 describe different approaches to determine a precise background prediction and how the background model used in the final analysis is constructed. The data is analyzed in the framework of a profile likelihood analysis (section 3.8) and the results are shown in section 3.9.

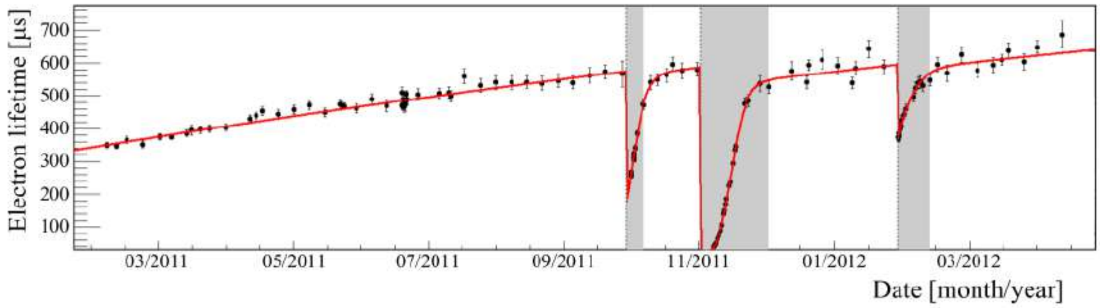

FIGURE 3.1: Evolution of the electron lifetime during run II. The gray areas mark short periods of detector maintenance that are excluded from the analysis. The average electron lifetime during this run is (519±64) μs.

3.1 Introduction

Over a period of four years, XENON100 acquired three long dark matter runs of 100.9, 223.1 and 154 live days, separated by short periods of maintenance. During this time the detector conditions were kept remarkably stable [125]. One significant difference between the individual runs, however, is the increased Kr concentration in run I caused by an air leak [123]. Due to the higher Kr content, the background of this run was dominated by the internal ^{85}Kr background and not by external backgrounds from detector materials. This allowed the use of a larger fiducial volume of 48 kg (compared to 34 kg in run II and III). Another exception is the electron lifetime, which increases with time as the xenon is constantly purified. The evolution of the electron lifetime during run II is shown in figure 3.1. All other relevant parameters are stable throughout the three runs and are summarized in table 3.1.

		Run I	**Run II**	**Run III**
Science Campaign	Live days [d]	100.9	223.1	153.0
	Period	2010	2011-2012	2013-2014
Detector condition	Average electron lifetime [μs]	294 ± 37	519 ± 64	720 ± 110
	L_y [PE/keV]	2.20 ± 0.09	2.28 ± 0.04	2.25 ± 0.03
	S2 amplification [PE/e$^-$]	18.6 ± 6.6	19.6 ± 6.9	17.1 ± 6.4
	Extraction field in gas [kV/cm]	11.89 ± 0.02	10.30 ± 0.01	11.50 ± 0.02
	Drift field [V/cm]	533	533	500
	^{nat}Kr concentration [ppt]	360 ± 70	19 ± 4	6 ± 1
Calibration	^{60}Co, ^{232}Th ER calibration in S1 range defined below [events]	4116	15337	10469
	^{241}AmBe NR calibration in S1 range defined below [events]	55423	25315	92226
Analysis	Low S1 threshold [PE]	3	3	3
	High cS1 threshold [PE]	30	30	30
	Low S2 threshold [PE]	300	150	150
	Fiducial mass [kg]	48	34	34
	Total Selected Events	929	402	346

TABLE 3.1: Detector and analysis parameters of all three runs. For the combined analysis of all three runs the S1 threshold has been equalized for all runs to S1 > 3 PE. S1 and S2 signals are only corrected for the different PMT gains while cS1 is also corrected for the position dependent light collection efficiency. Table from [75].

Run I and II have already been analyzed and limits on the SI and SD WIMP interaction cross sections have been published in [123] and [86, 124], respectively. However, in the course of the combined analysis of all three runs some improved selection criteria are applied post unblinding on the first two runs. Additionally, the background model is redefined for all three runs based on the principles discussed in this chapter.

3.2 Data selection

In XENON100 the analog signals measured by each of the 178 PMTs (plus 64 veto PMTs) are amplified by a factor of ten, using Phillips 776 NIM amplifiers. The amplified signal is digitized, read out and stored to disk. Subsequently the data is processed and a variety of peak properties are derived by the XENON100 data processor. Among them are the uncorrected energies of the measured peaks (S1 and S2) and the corrected energies (cS1 and cS2).

In order to select single scatter events, as expected from WIMP interactions, various selection criteria and data quality cuts are applied on the data. These cuts are summarized in table 3.2 and are explained in more detail in the previous publications of run I and run II [86, 111, 123]. For the combination of all three runs two additional cuts have been developed. In the case of run I and II these new cuts are applied post-unblinding and in the case of run III all cuts have been defined while the data was still blinded.

The first new data quality criteria is related to lone S1 peaks (an S1 without any correlated S2) during dark matter data taking. It has been found that in run II there are periods of significant higher rates of lone S1 peaks not consistent with a random occurrence (e.g., PMT dark current). Due to the higher lone S1 rate there is an increased probability of an accidental pairing to a random lone S2 during these periods. Although the origin of these S1 bursts is not known, they indicate an anomalous behavior of the detector and all periods with three or more lone S1s present in a 500 s window are excluded. This data quality criteria was defined and fixed based on run II data and applied post-unblining on all runs. While there were no such high rate periods found in run I, the live times of run II and run III are reduced by $\sim 0.7\,\%$ and $\sim 0.4\,\%$, respectively.

The second new cut is due to the fact that the XENON100 data processor sometimes misidentifies single-electron S2 peaks as S1 peaks which can lead to non-physical events leaking into the region of interest and thus significantly contribute to the expected background. Therefore, a new cut has been defined based on the improved peak classification of the new XENON1T data processor and has been applied post-unblinding on run II and blinded on run III. This cut is described in more detail in section 3.3.2.

Cut	NR acceptance in ROI
Reject noisy events based on S1 width	$> 97\,\%$
Reject events with no valid S1 peak	$\sim 98\,\%$
Remove events with noisy waveform	$98\,\%$
Remove S2 peaks with unusual x-y position and/or unusual fraction of light seen by top PMT array	$> 99.6\,\%$
Require twofold PMT coincidence for S1 peaks	$> 99\,\%$ above 10 PE ($\sim 60\,\%$ at 3 PE)
S1 threshold (S1 $>$ 3 PE)	
S2 threshold	Run I: $> 99\,\%$ above cS1=10 PE ($\sim 85\,\%$ at cS1=3 PE) Run II+III: $> 99\,\%$ above cS1=10 PE (95 % at cS1=3 PE
Remove events with more than one S2 peak	$> 95\,\%$
Remove events with more than one S1 peak	$> 97\,\%$
No signal in the active LXe veto	$\sim 99.5\,\%$
Remove double scatter events based on x-y position reconstruction	$> 99.6\,\%$
Remove S2 peaks with unphysical width	$\sim 90\,\%$
Remove events with unlikely S1 PMT hitpattern	$\sim 97\,\%$
Remove events with unphysical S2/S1 parameter	$> 99.9\,\%$
Require event to be inside the fiducial volume	$100\,\%$
Remove periods with high lone S1 rate	reduction of live time $< 0.7\,\%$
Remove misidentified S1 peaks	$\sim 99\,\%$ (only applied on run II+III)

Table 3.2: Summary of selection criteria and their NR acceptance used in this analysis. The last two cuts have been developed for the combined analysis of all three runs and are described in more detail in the text. All other selection criteria are described in [111].

Furthermore, the S1 threshold is now defined prior to corrections and set to S1$>$ 3 PE for all runs. Defining the threshold on the uncorrected S1 instead of the corrected cS1 takes into account the variations of the light collection efficiency (LCE) throughout the TPC more precisely. This results in a position dependent energy threshold with a lower value ($3\,\mathrm{keV_{nr}}$) towards the bottom of the TPC and a higher value ($8.5\,\mathrm{keV_{nr}}$) at the top of the TPC, where the LCE is lower but leads to a more uniform acceptance.

3.3 Backgrounds in XENON100

In order to enhance the sensitivity of direct dark matter detectors, it is important to reduce all backgrounds as much as possible. The total expected background in XENON100 is reduced to ~ 2.6 events/year inside the region of interest (a 34 kg fiducial volume and an energy range of (3–30) PE). The process required to get down to this level of background starts with the selection of radiopure materials used to build the detector [117]. In order to select those materials, extensive screening campaigns were carried out with high-purity germanium detectors (HPGe) [79] as well as inductively coupled Plasma-Mass Spectrometry (ICP-MS) for samples with a mass too small to achieve reasonable results with a HPGe. Backgrounds from external radiation is suppressed by a passive shield made of copper, lead and polyethylene. A cryogenic krypton distillation column is used to reduce the Kr content and thus the concentration of the radioactive isotope ^{85}Kr inside the liquid xenon. After these steps of physically reducing possible background sources, the trigger rate of XENON100 is $\sim 1\,\mathrm{Hz}$. The background can be further reduced at analysis level by selecting a fiducial volume in order to take advantage of the self shielding of liquid xenon. Furthermore, it is possible to discriminate between nuclear recoil and electronic recoil events. However, despite the large effort of reducing the background by detector design as well as rejecting it during analysis, there might be some remaining background and thus it is important to know precisely how large this contamination is. In the subsequent sections the expected number of remaining background events in the region of interest is estimated and the procedure of constructing a two dimensional background model used as input for the profile likelihood analysis is discussed.

3.3.1 Separation of electronic and nuclear recoils

Nuclear recoil (NR) interactions in liquid xenon can be distinguished from electronic recoils (ER) based on their charge-to-light ratio (S2/S1). This can be explained by their different ionization density and the different resulting track structures (see also section 2.2). As WIMPs are expected to scatter off the nucleus, the possibility to discriminate between ER and NR is an important tool to suppress a significant amount of background originating from γ and β radiation. In the following, the parameter to describe the discrimination between ER and NR is defined as

$$\log_{10}(\mathrm{cS2_{bot}}/\mathrm{cS1}) - \mathrm{ER\,mean(cS1)} \tag{3.1}$$

analogous to the representation used in [86]. “ER mean” is the energy dependent mean of the electronic recoil band and $\mathrm{cS2_{bot}}$ is the corrected S2 signal seen by the bottom PMT array, which is used since its response to S2 signals is more uniform than for the top PMT array, where mesh warping and non-working PMTs locally lead to larger corrections [77]. Plotting the discrimination parameter introduced above as a function of S1 energy results in a flat ER band centred around zero as is shown in figure 3.2 (black points).

NR events on the other hand have a smaller charge to light ratio and will end up below the ER recoil band, shown as red points in figure 3.2. The red line shows the 99.75 % rejection line, meaning that 99.75 % of the ER events are located above this line. The projection of the ER band on the y-axis can be well described by a Gaussian function as shown in figure 3.3. Thus, the fraction of ER events leaking below the 99.75 % rejection

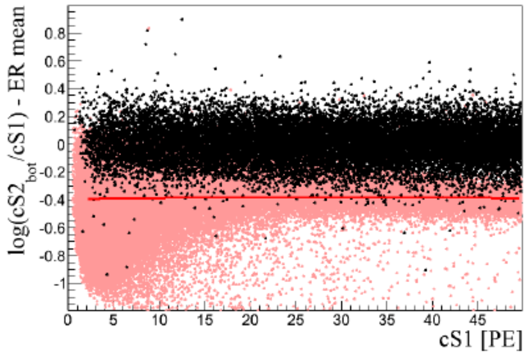

FIGURE 3.2: ER band from ^{60}Co and ^{232}Th calibration data in black and NR band from AmBe calibration data in light red. The ER rejection line at a level of 99.75 % is represented by the red line.

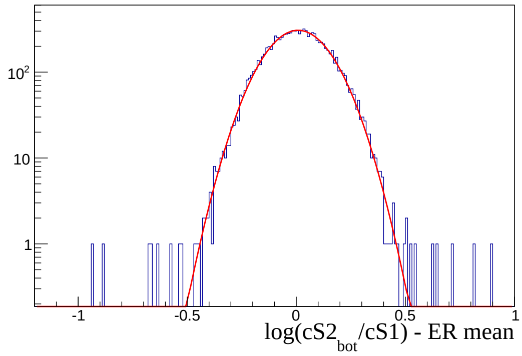

FIGURE 3.3: Projection of the ER band (figure 3.2) on the y-axis in blue and Gaussian fit shown in red. While the bulk of the band can be well described by this fit function, there are some remaining events in the tails that cannot be modeled by the Gaussian function.

line originating from the Gaussian tail is called "Gaussian leakage". Figure 3.3 also shows that some of the calibration events (blue histogram) show exceptional negative (and positive) discrimination values, which cannot be explained by the Gaussian tail and thus they are called "non-Gaussian leakage" or "anomalous leakage". Based on the Gaussian parametrization of the ER band an ER rejection level of 99.75 % can be achieved for run III while keeping a NR acceptance $> 30\,\%$ which is shown in figure 3.4 (red points).

The width of the ER and NR bands, which affects their separation and thus the ER rejection power, is determined by the fluctuations of the initially generated quanta as well as the statistical fluctuations in the process of detecting the signals. By increasing the light yield L_y (or charge yield) of the detector the latter can be reduced since more light (charge) quanta are detected at a given energy and thus the statistical fluctuations of the signal become less prominent. The effect of an increased L_y on the discrimination power against ER background has been studied in [76]. As expected the fraction of leaking events gets smaller with larger L_y (see figure 3.5). Increasing the discrimination

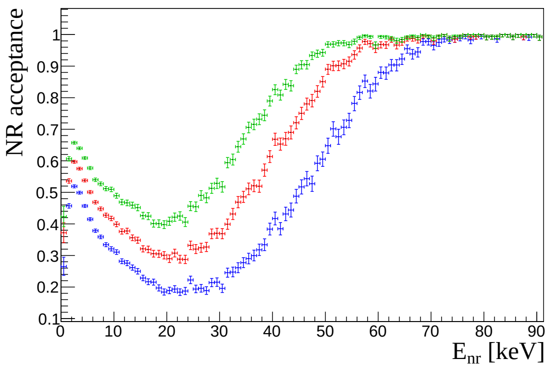

FIGURE 3.4: Acceptance of the nuclear recoil band depending on the S1 energy for different levels of ER rejection in run III. Green corresponds to an ER rejection power of 99.5 %, red to 99.75 % (also shown in figure 3.2) and blue to 99.9 %. In the case of 99.75 %, which is used to define the region of interest, the average NR acceptance in a region from 6.6 keV to 43.3 keV is ∼40 %.

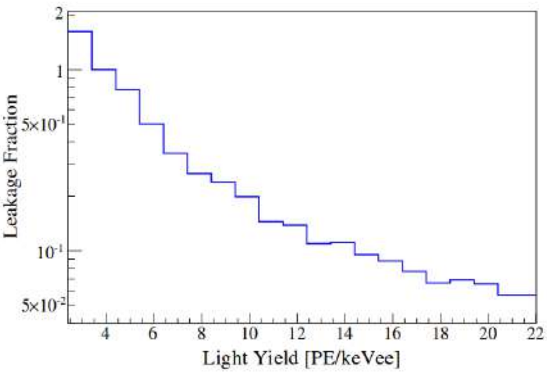

FIGURE 3.5: Illustration of the impact of the zero-field light yield L_y at 122 keV$_{\mathrm{ee}}$ on the ER rejection, assuming a constant NR acceptance of 30 %. The fraction of ER events leaking into a low energy WIMP search region is determined in a simulation and quoted relative to the leakage for a moderate light yield of 4.0 PE/keV$_{\mathrm{ee}}$. All other parameters which might have an impact on the ER rejection were kept constant. The fluctuations in the leakage fraction are purely statistical. Figure from [76].

power and thus lowering the ER background based on the charge to light ratio will be important for next generation multi-ton liquid xenon detectors [84].

3.3.2 Misidentified single-electron S2 events

During the analysis of ER calibration data it has been found that a significant fraction of the events that leak into the region of interest (i.e., below the 99.75 % rejection line) show an S1 peak which is misidentified by the XENON100 data processor Xerawdp. Those peaks are actually caused by single-electron S2 signals [103]. A typical waveform of such a misidentified S1 peak is shown in figure 3.6. Because the S1 and S2 peaks are not causally connected, the S2/S1 ratio can take any value and the event might leak into the NR band. For XENON1T a new data processor, pax, has been developed [129] which features improved S1 and S2 classification. Thus, in the course of this analysis a new cut has been defined based on the peak classification used in pax in order to reject misidentified S1 peaks and the related leaking events.

The new cut is based on the S1 peak width at 50 % peak area. As shown in figure 3.7, the requirement of a minimal width of 100 ns for S1 peaks results in a rejection of 9 out of the 10 leaking events due to misidentification found by visual inspection in the ER calibration data of run III. Furthermore, a simulation of single-electron S2 peaks

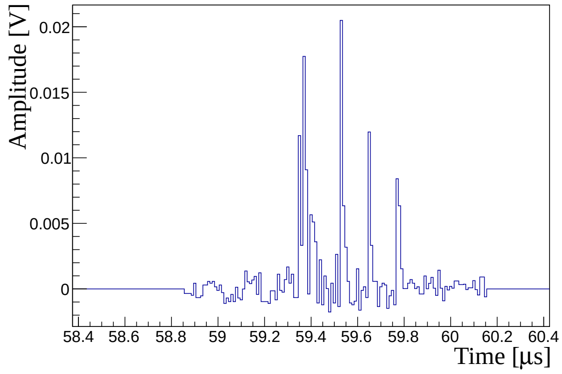

FIGURE 3.6: Example waveform of a single-electron S2 peak, misidentified as an S1 peak by Xerawdp. Thanks to an improved classification algorithm, those peaks are better identified by the new XENON1T data processor pax.

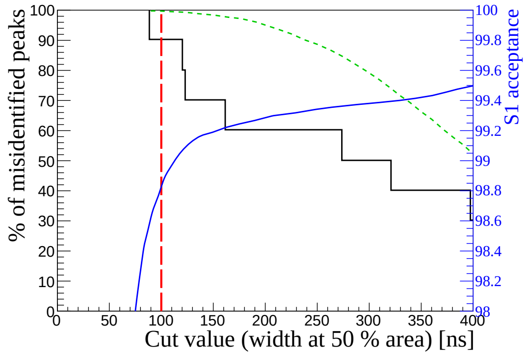

FIGURE 3.7: The left y-axis indicates the efficiency of tagging misidentified single-electron S2 peaks depending on the width at 50 % peak area determined by pax. The solid black line corresponds to peaks misidentified by Xerawdp and the dashed green line represents a simulated sample of single-electron S2 peaks. The blue curve (right axis) shows the corresponding acceptance of NR S1 peaks. The cut value used for runs II and III is set to 100 ns, indicated by the red dashed line. Data from J. Aalbers.

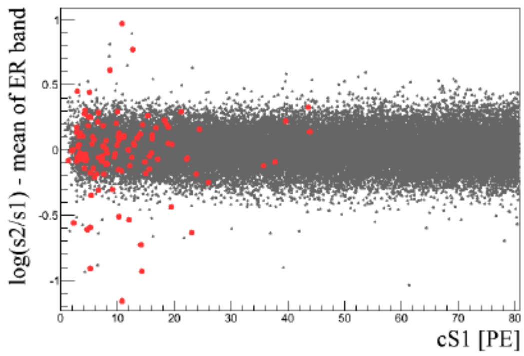

FIGURE 3.8: ER band from calibration data (gray points) shown together with events that are identified by the new cut developed in order to remove misidentified single-electron S2 peaks (red points). As expected, they are concentrated at lower energies where a misidentification is more likely to happen.

indicates that the efficiency of this cut in removing misidentified S1s is $> 90\,\%$, as shown by the green dashed line in figure 3.7. The overall acceptance for NR events is $> 98\,\%$ (blue line). Since at higher energies an S1-misidentification gets much more unlikely, these events are expected to be concentrated at lower energies. This is confirmed in figure 3.8, where the ER band is represented by the gray points and events that are identified by the new cut are shown in red. Since the raw data of the science run I was not available for re-processing, the new cut against misidentified single-electron S2s was only applied to the considerably longer runs II (post-unblinding) and III (on blinded data), reducing the number of events leaking below the 99.75 % ER discrimination line by $\sim 30\,\%$.

In order to form a fake interaction, a misidentified single-electron S2 peak has to be combined with a second accidental S2 peak and thus this background depends on the event rate. The ER background models introduced in the following sections are derived using ER calibration data and normalized to dark matter data based on the total number of events in a non-blinded region, called "scaling box". This approach assumes that the number of ER events leaking into the region of interest only depends on the total number of ER events and not on the event rate of each data sample. Therefore, it is important to remove events containing misidentified S2 peaks from the calibration sample since the event rate in calibration data is much higher than in dark matter data.

3.4 The box model

A first quantitative background estimate can be determined by defining a region of interest and calculating the expected number of events inside this region. The background estimate presented in this section refers to run III, but the principle can be applied to all three runs. The region of interest is defined by the S1 energy range of (3–30) PE corresponding to (6.6–43.3) $\mathrm{keV_{nr}}$. The upper boundary of the discrimination parameter is set to the 99.75 % ER rejection line, shown in figure 3.2 (red line), and the lower boundary by the 97 % NR acceptance defined on AmBe calibration data. Both NR background and ER interactions leaking into the NR band will contribute to the total expected background in this region.

Analogous to the run II procedure [86] the background contribution from NR interactions is derived from a Monte Carlo (MC) simulation [130], which calculates the expected neutron background from (α, n) and spontaneous fission reactions. The simulation relies on the measurement of intrinsic radioactive contaminations of all detector materials. These measurements have been carried out in advance. In addition, the neutron background induced by muons is estimated taking into account the muon energy and angular distribution at LNGS. SOURCES4A [131] in used to generate the neutron spectra and the rate of (α, n) and fission reactions, which are then used as inputs to a GEANT4 [132] simulation. The energy and angular distribution of the muons have been simulated using MUSUN and MUSIC [133], with GEANT4 used for the muon propagation. The resulting energy spectrum of the neutron background, shown as black line in figure 3.9, is converted from $\mathrm{keV_{nr}}$ to PE using the relative scintillation efficiency L_{eff} as defined in [86]. Poisson smearing is applied in order to account for the S1 energy resolution. For the NR background prediction presented in this section the smeared energy spectrum is taken from [130] and is multiplied by the NR acceptance of all run III selection criteria as well as the NR acceptance for the 99.75 % ER rejection line (see figure 3.4). The resulting spectrum, represented by the green histogram in figure 3.9, is integrated in the energy range of (3–30) PE, corresponding to the WIMP search region defined above, and multiplied by 34 kg $\times$ 153 days in order to take into account the total exposure of run III. In the region of interest this results in a nuclear recoil background expectation of $0.11^{+.07}_{-0.4}$ events where the errors are dominated by the uncertainties of the MC simulation.

The estimate of ER interactions leaking into the region of interest is based on ER calibration data, and normalized to run III using the number of events in a non-blind region of the dark matter data, the scaling box. The underlying assumption of this approach is that at low energies the ER background in dark matter data can be well represented by ^{60}Co and ^{232}Th calibration data. In figure 3.10 a comparison of the

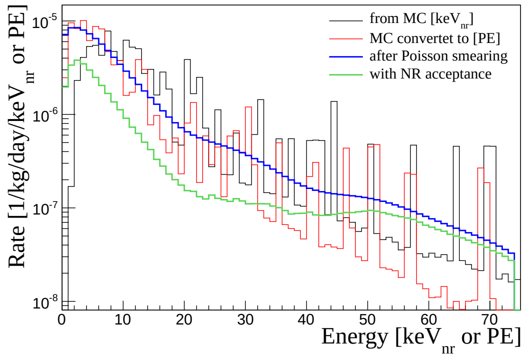

FIGURE 3.9: Monte Carlo simulation of the NR background [130]. The simulated energy spectrum in keV$_{nr}$ (black) is converted to PE (red) and Poisson smeared in order to account for the S1 resolution (blue). Finally, it is multiplied by the NR acceptance of the selection cuts, as well as the acceptance of the 99.75 % ER rejection line from figure 3.4 (green). The spikes at higher energies are due to the low statistics of muon-induced neutrons in the simulation.

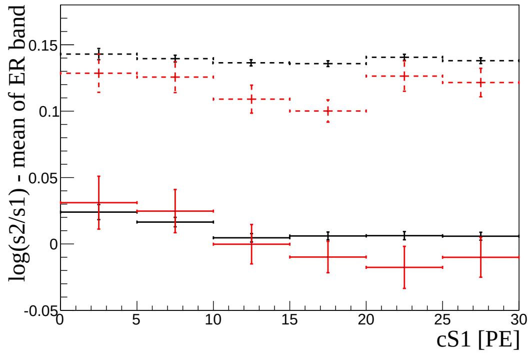

FIGURE 3.10: Comparison of the width (dashed lines) and the mean (solid lines) between the ER bands from dark matter (red) and ER calibration (black) data as a function of S1 energy. At first order the distributions of the different data sets agree with each other.

width and the mean between the ER bands from dark matter and ER calibration data is shown. It can be seen that at first order this assumption is true. There are, however, indications of differences between the two data sets, which are the subject of further investigations. Nevertheless, it is necessary to rely on ER calibration data sets in order to get an estimate of the expected ER background in the blinded region of interest. This is because the ER background does not only consist of the Gaussian contribution, which could be modelled by extrapolating the non-blinded dark matter data into the region of interest, but also consists of non-Gaussian background. A known origin of this anomalous background are double scatter events, scattering once inside the TPC and once in the charge insensitive region between the bottom PMT array and the cathode. This kind of background can also be calibrated using ^{60}Co and ^{232}Th calibration sources.

Assuming that the ER events in calibration and dark matter data follow the same distribution, the most basic background expectation inside the WIMP search region can be derived by counting the number of events in calibration data and normalizing it to dark matter data according to the total number of events inside the scaling box in each data set. In figure 3.11 the scaling box is shown by the dashed blue line, while the dashed red line represents the region of interest. The normalization factor derived using the scaling box is

$$\frac{\text{events in scaling box of DM data}}{\text{events in scaling box of calibration data}} = \frac{304\,\text{events}}{8738\,\text{events}} = 0.035 \pm 0.002 \qquad (3.2)$$

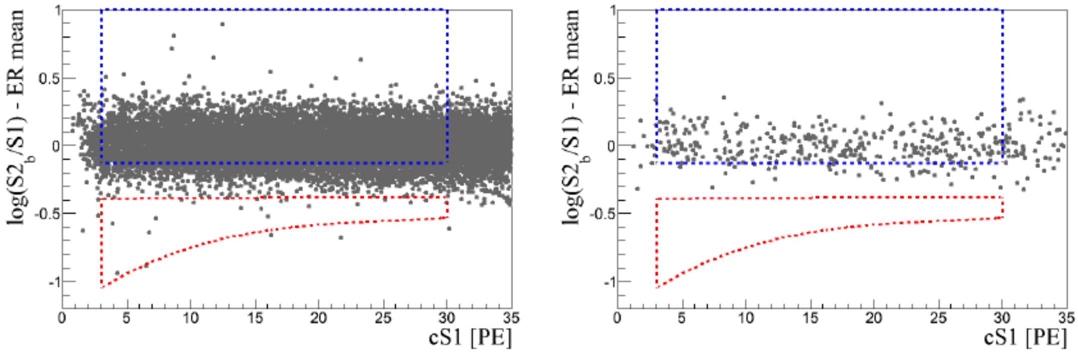

FIGURE 3.11: ER calibration data **(left)** and blinded dark matter data of run III **(right)**. The region of interest is indicated by the red dashed box with its upper boundary defined by the 99.75 % ER rejection line and its lower boundary given by the 3 σ quantile of the NR band. The energy interval of the search region is (3–30) PE, corresponding to (6.6–43.3) $\mathrm{keV_{nr}}$. The blue dashed box indicates a non-blinded region, scaling box, used to normalize the number of calibration events inside the region of interest to dark matter data.

where the error represents the statistical fluctuations in the number of observed events. Multiplying this factor with the number of calibration events found inside the region of interest results in a background prediction of

$$(19 \pm 4.4\,\text{events}) \cdot (0.035 \pm 0.002) = \mathbf{0.66 \pm 0.16}\,\text{events}. \tag{3.3}$$

Again the error represents the statistical uncertainty and does not take into account the systematic uncertainty of the underlying assumption. A summary of the prediction of both, the ER and NR background contributions can be found in table 3.3.

As this model provides an estimation of the total number of expected background events in the benchmark region of interest, it would be suitable for an analysis based on counting events such as the approach by Feldman and Cousins in [134]. This approach, however, does not take advantage of the fact that the distribution of the leaking events is not expected to be uniform inside the region of interest. Nevertheless, the box model provides an important quantification of the expected background prior to the unblinding of the dark matter data.

Background source	**Background prediction**
Nuclear recoil	$0.11^{+0.07}_{-0.4}$ events
Electronic recoil	0.66 ± 0.16 events
Total	$0.77^{+0.17}_{-0.4}$ events

TABLE 3.3: Summary of the background predictions for run III inside the region of interest. The NR background contribution is derived from MC simulation and the ER background prediction is based on the box model.

3.5 Two dimensional NR model and ER fit model

Since the Gaussian leakage mainly contributes to the upper part of the region of interest in figure 3.11, averaging the background over the whole region results in an overestimation of the background in the lower part where the separation between ER and NR interactions is the best. One possible way to take this into account in the analysis, and thus to improve the sensitivity of the experiment, is to perform a profile likelihood analysis. In order to use such an analysis a two dimensional model describing the distribution of the background has to be created.

Two dimensional NR model

The NR background model presented in this section has been developed by P. Di Gangi. As for the box model, the energy spectrum of the nuclear recoil background is generated using the MC simulation described in [130] (see figure 3.9). In order to derive a two dimensional model this energy spectrum, as well as the position distribution of the NR background from GEANT4, is used as input information for a MC simulation where (S1, S2) signal pairs are generated event-by-event (performed by Pietro Di Gangi). The procedure described here is similar to the light and charge signal generation from [54].The average number of available quanta in a NR interaction, $\langle N_Q \rangle$, is given by

$$\langle N_Q \rangle = \langle N_{\mathrm{ph}} \rangle + \langle N_{e^-} \rangle \,. \tag{3.4}$$

$\langle N_{\mathrm{ph}} \rangle$ is the mean number of generated photons defined as

$$\langle N_{\mathrm{ph}} \rangle = E_{\mathrm{nr}} \cdot L_{\mathrm{eff}} \cdot Ph_y^{122\,\mathrm{keV}} \cdot S_{\mathrm{nr}} \tag{3.5}$$

where E_{nr} is the recoil energy, L_{eff} the relative scintillation efficiency from [123], $S_{\mathrm{nr}} = 0.95$ the scintillation quenching for an electric field of 530 V/cm and $Ph_y^{122\,\mathrm{keV}} = 63.4\,\mathrm{ph/keV}$ is the photon yield at a gamma energy of 122 keV and zero field, estimated using a phenomenological model in NEST [108]. $\langle N_{e^-} \rangle$ is the mean number of generated electrons defined as

$$\langle N_{e^-} \rangle = E \cdot Q_y \tag{3.6}$$

where Q_y is the energy dependent charge yield derived in [95].

In order to take into account fluctuations in the amount of energy converted into the invisible heat channel the number of available quanta, N_Q, is drawn from a binomial distribution

$$N_Q = \mathrm{Binomial}(n = N_Q^{\mathrm{ER}}, p = \langle N_Q \rangle \,/\, \langle N_Q^{\mathrm{ER}} \rangle) \tag{3.7}$$

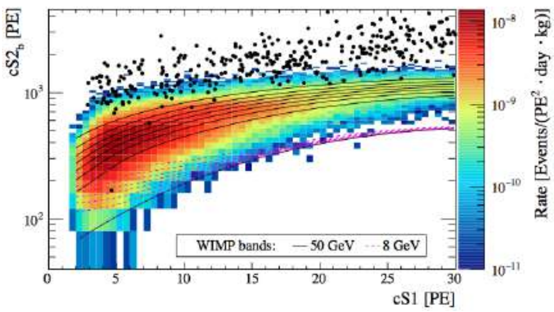

FIGURE 3.12: Two dimensional NR background model for run III based on MC simulation. The science data and signal bands, as in figure 3.21, are overlaid for reference. The black and magenta lines show the profile likelihood bands introduced in section 3.8. Figure from [75].

where $\left\langle N_Q^{\mathrm{ER}} \right\rangle = 72 \cdot E_{\mathrm{nr}}/\mathrm{keV}$ is the average number of produced quanta in a ER interaction. Subsequently, the number of generated photons, N_{ph}, is also sampled with a binomial distribution

$$\mathrm{Binomial}\left(n = N_Q, p = \langle N_{\mathrm{ph}} \rangle / \langle N_Q \rangle\right). \tag{3.8}$$

Finally, the number of generated electrons, N_{e^-}, is the difference between N_Q and N_{ph} whereby the anticorrelation between light and charge signal is taken into account.

N_{e^-} is converted into the detector observable $\mathrm{S2_{bot}}$ using the secondary scintillation gain for the bottom array $7.2 \pm 4.2\,\mathrm{PE}/e^-$. The cS1 signal is generated by multiplying N_{ph} with the probability for a photon to produce a photoelectron (PE). The position dependent light collection efficiency as well as the finite electron lifetime is taken into account and thus the output variables of the simulation are the corrected signals cS1 and $\mathrm{cS2_{bot}}$. The resulting two dimensional NR background model is shown in figure 3.12.

The expected NR background derived from the two dimensional NR model in the benchmark WIMP region is 0.09 ± 0.7 events. This number is compatible with the predicted $0.11^{+.07}_{-0.4}$ events based on the simulated (one dimensional) energy spectrum of the NR background presented in section 3.4.

The Gaussian ER background component

As for the box model, the ER background model is based on ^{60}Co and ^{232}Th calibration data normalized using dark matter data. However, this time the model is split into two parts: the Gaussian component and the non-Gaussian component.

In order to determine the Gaussian component the ER calibration data, shown in figure 3.11 (left), is split along the x-axis into slices of 1 PE width. The projection of each of these slices is fitted by a Gaussian function. The resulting parameters (amplitude, mean and σ, from top to bottom) are shown in figure 3.13. In order to get a smooth background model along both axes (discrimination parameter and S1) the extracted parameters are described by polynomial functions, represented by the solid red lines in

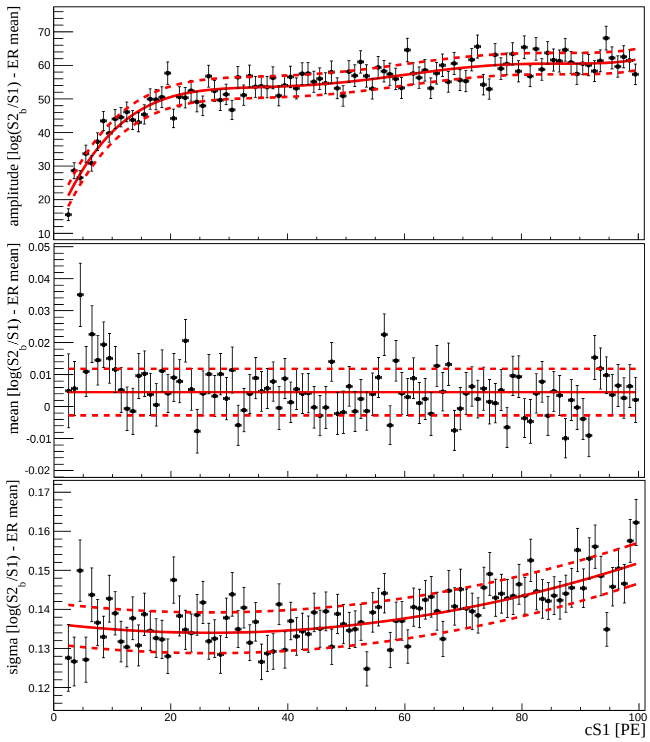

FIGURE 3.13: Amplitude (top), mean (middle) and sigma (bottom) of the Gaussian fits on the projection of the sliced ER band (from figure 3.2) for each S1 bin (black points). The error bars correspond to the fit error of each parameter. They are parametrized by a 5th order (amplitude), a 0th order (mean) and a 3rd order (sigma) polynomial function shown as solid red lines in order to get a smooth model of the Gaussian ER band. The red dashed lines represent a variation of the solid red line by the square root of the variance between the black points and the solid red curve.

figure 3.13. The dashed red lines in each plot of figure 3.13 represent the parametrization raised/lowered by the square root of the variance between the black points and the red solid line. Using the red functions in figure 3.13 the following three ER Gaussian models are defined:

1. The **central model** that uses the mean parametrizations (solid red functions) of figure 3.13, which is the actual model for the Gaussian ER component.
2. The **minimum leakage model** using the parametrization lowered/raised by the variance (red dashed lines) such that the leakage into the region of interest gets minimal.
3. The **maximum leakage model** using the parametrization lowered/raised by the variance (red dashed lines) such that the leakage into the region of interest gets maximal.

By integrating the central model in the region of interest the estimated ER background from the Gaussian contribution is 0.72 ± 0.17 events where the error represents the difference between the central model and the minimum/maximum leakage models. The final two dimensional model of the Gaussian ER background component is shown in figure 3.14, where the discrimination parameter on the y-axis has been transformed into $cS2_{bot}$ since this representation is used in the profile likelihood analysis (see section 3.8).

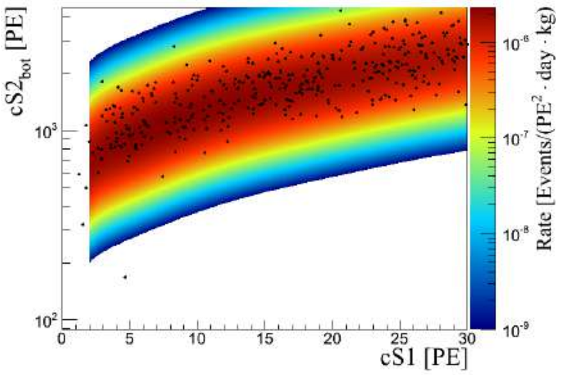

FIGURE 3.14: Two dimensional model of the Gaussian ER band, represented in $cS2_{bot}$ vs. cS1. This model is based on the parametrization of the Gaussian fits shown in solid red in figure 3.13. The Black points show the events from the dark matter run III.

The non-Gaussian ER background component

Even though the bulk of the ER band is well described by the Gaussian component of the background model there are some remaining events that cannot be described by the Gaussian model and need to be modeled independently. One possible source of this non-Gaussian background are events with incomplete charge collection. This might happen in the case of a double scatter event where one interaction is located inside the TPC and the other in a charge insensitive region, such as the region between the bottom PMT array and the cathode. Another possible source are accidental coincidence events, where a lone S1 (S1 without correlated S2) and a lone S2 are accidentally combined. This source is discussed in more detail in section 3.6. Figure 3.15 shows the number of ER calibration events between (3–20) PE (black points) depending on the distance from the mean of the ER band in units of σ of the Gaussian distribution together with the Gaussian background model in red. It can be seen that the data is well described by the Gaussian model up to a distance of $\sim 3\,\sigma$ from the mean of the ER band where the number of observed events starts to deviate from the prediction of the model. In figure 3.16 the number of events more than 3.5σ away from the mean of the ER band vs. their energy is shown by the black points. As there are very few events, the statistical error bars are quite large and the spectrum can be described by a zeroth order polynomial function (solid red line in figure 3.16). It is assumed that the non-Gaussian component is uniformly distributed along the discrimination parameter $\log_{10}(cS2_{bot}/cS1) - \mathrm{ER\,mean}$. Thus the non-Gaussian component can be modeled by a uniform distribution along both axes. In the benchmark WIMP this results in a background prediction of 0.08 ± 0.02, where the error is calculated by varying the constant fit along the cS1 axis by its fit error (see figure 3.16). As shown in figure 3.17 a good agreement between ER calibration data and the background model can be achieved by combining the Gaussian and the non-Gaussian components. The total ER background model (Gaussian plus non-Gaussian component) is shown in figure 3.18, where again the discrimination parameter on the y-axis is transformed to $cS2_{bot}$, the representation used in the profile likelihood analysis (see section 3.8). In contrast to the Gaussian-only model in figure 3.14, there is now

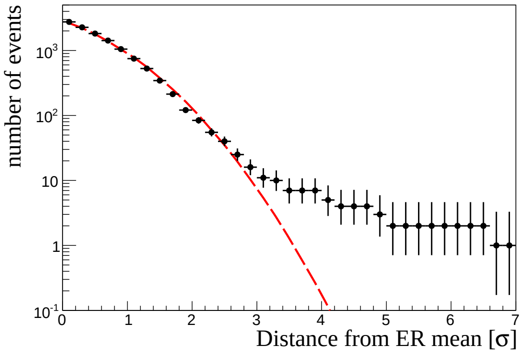

FIGURE 3.15: The number of observed ER calibration events integrated between (3–20) PE as a function of their distance to the mean of the ER band in units of σ of the Gaussian distribution (black points). The error bars correspond tot he 68 % Poisson probability region. $1\,\sigma$ for example, includes all events that are at least $1\,\sigma$ below the ER mean. A deviation from the Gaussian background model, shown in red, can be seen starting around $3\,\sigma$, which can be attributed to the non-Gaussian background component.

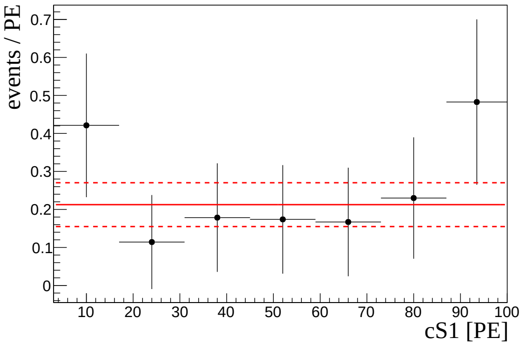

FIGURE 3.16: Number of events more than $3.5\,\sigma$ away from the mean of the ER band (see figure 3.15) vs. their energy. The non-Gaussian fit model is based on a constant fit of this energy distribution (red line), which is a suitable parametrization considering the large statistical errors. The fit error is shown by the red dashed lines.

a non-zero background prediction below the main ER band which is due to the added non-Gaussian component.

The total ER background prediction from the fit model in the benchmark WIMP region is 0.81 ± 0.17. This number is dominated by the Gaussian component with an expectation of 0.72 ± 0.17 while the non-Gaussian contribution is only 0.08 ± 0.02. In principle the contribution from the Gaussian component can be reduced by increasing the ER rejection power. A rejection level of 99.9 % instead of 99.75 % for example would result in a reduction of the Gaussian background component by $\sim 60\,\%$. However, this would also result in a reduction of the NR acceptance by $\sim 10\,\% - 15\,\%$ (see figure 3.4). In the framework of a profile likelihood analysis the ER rejection power does not have to be fixed since the method takes into account the two dimensional shape of the background.

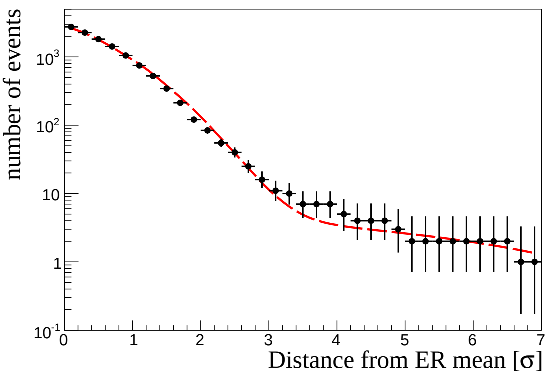

FIGURE 3.17: Similar to figure 3.15 the number of ER calibration events between (3–20) PE as a function of their distance to the mean of the ER band are shown as black points. The error bars correspond tot he 68 % Poisson probability region. The combined Gaussian plus non-Gaussian model is shown in red. A good agreement between the data and the combined model can be observed.

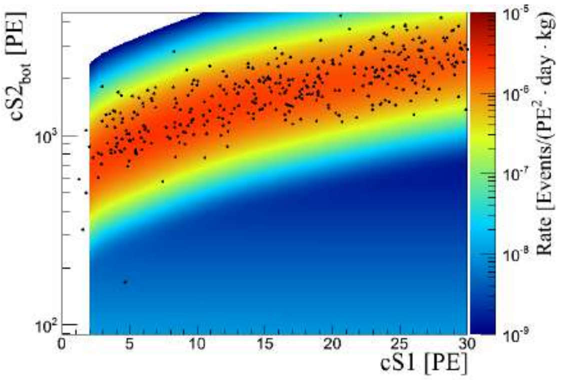

FIGURE 3.18: Combined Gaussian plus non-Gaussian fit model of run III. The color scale represents the expected event rate in [events/(PE$^2 \cdot$ day $\cdot$ kg)]. The non-Gaussian model is responsible for the non-zero background prediction below the ER band. The Black points show the events from the dark matter run III.

The total number of expected background events is compatible with the prediction of $0.66 \pm .016$ events derived by the box model. A summary of the two models can be found in table 3.4.

Model	**Gaussian component**	**Non-Gaussian component**	**Total ER background**
Box model	—	—	0.66 ± 0.16
Fit model	0.72 ± 0.17	0.08 ± 0.02	0.81 ± 0.17

TABLE 3.4: Summary of the run III ER background prediction based on the box model described in section 3.4 and the fit model described in this section. In case of the fit model the predictions are obtained by integrating the corresponding model-component in the region of interest defined by the energy interval (3-30) PE, the 99.75 % ER rejection line and the lower $3\,\sigma$ quantile from AmBe calibration data. The error of the Gaussian component is derived using the minimum/maximum leakage model and the error for the non-Gaussian component by varying the constant fit shown in figure 3.16.

3.6 Accidental coincidence and combined background model

One source of non-Gaussian background are accidental coincidence (AC) events where a lone S1 and a lone S2 peak are combined by chance and form a fake event. In [75] this source of background has been modeled for the first time for XENON100 (by Qing Lin). This data driven model is similar to the one developed in [135] and is based on the separate selection of lone S1 and lone S2 peaks. Lone S2s can be selected using the same S2 criteria as for S2 peaks of ordinary events with the additional requirement that there must be no S1 identified preceding the S2 peak. In order to get a lone S1 spectrum two regions are localized in the S2 vs.S1 plane consisting of lone S1 peaks, shown in figure 3.19. While the type A population mostly consists of AC events but has small statistics, the type B population has larger statistics but is contaminated by S1-S2 pairs where the S2 is caused by impurity photoionization preceding the S1 peak. These secondary S2s can be modeled by the rate difference between type A (AC events only) and type B (AC plus secondary S2s) events. the lone S1 distribution is obtained from type B events, after subtracting the contribution from secondary S2s. The final

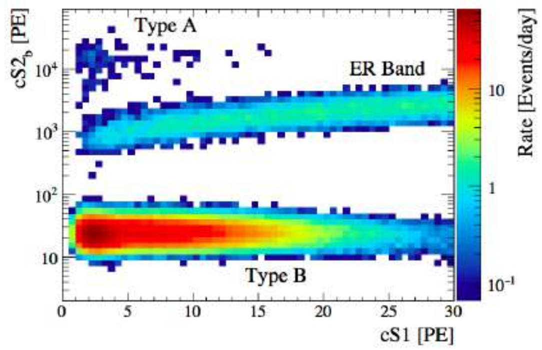

FIGURE 3.19: run III ER calibration data showing the event populations consisting of Type A and B lone S1s used for the accidental coincidence model [75]. A similar sample can be selected in the dark matter data set.

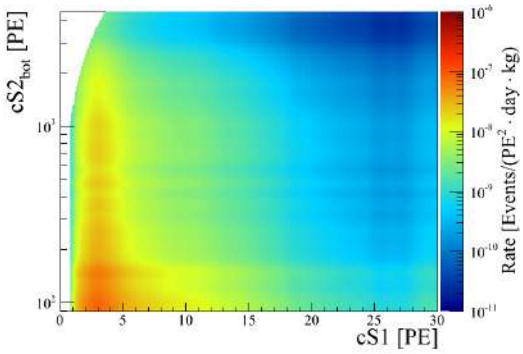

FIGURE 3.20: Accidental coincidence model of the non-Gaussian background component, obtained by multiplying the energy spectra of the lone S1 and lone S2 peaks.

AC model, shown in figure 3.20, is derived by multiplying the lone S1 and the lone S2 spectra.

The non-Gaussian background at low energies is well described by the AC model. At higher energies, however, the background is slightly underestimated. In contrast to the non-Gaussian model described in section 3.5 the AC model has an underlying theory and thus can be physically motivated. Therefore, for the analysis of run III and the reanalysis of run I and II the AC model is used in order to describe the non-Gaussian ER background at low energies, while the empirical model is used to account for the remaining background at higher energies. More specifically the final non-Gaussian ER background model is defined as

$$f^{\mathrm{ER}}_{\mathrm{NG}}(\mathrm{cS1},\, \mathrm{cS2}_{\mathrm{bot}}) = f_{\mathrm{AC}} + max(f_{\mathrm{AN}} - f_{\mathrm{AC}}, 0) \tag{3.9}$$

where f_{AC} denotes the AC model and f_{AN} the empirical non-Gaussian fit model described in section 3.5. The total background model f_b is defined by adding up the two dimensional nuclear recoil model f^{NR} and both electronic recoil components (Gaussian and non-Gaussian).

$$f_b = f^{\mathrm{NR}} + f^{\mathrm{ER}}_{G} + f^{\mathrm{ER}}_{\mathrm{NG}} \tag{3.10}$$

3.7 Sideband unblinding of physics run III

Like the selection criteria, the background model was developed while the dark matter data was still blinded in the benchmark WIMP region. In order to cross check and validate the background model of science run III a sideband unblinding outside the energy region of interest (30–100) PE was performed. A summary of the predictions of all background model components in the sideband region as well as the number of events found in the data can be seen in table 3.5. Since at high energies the non-Gaussian model $f_{\mathrm{NG}}^{\mathrm{ER}}$ defined in equation (3.9) is dominated by the empirical non-Gaussian model f_{AN} the predictions for $f_{\mathrm{G}}^{\mathrm{ER}}+f_{\mathrm{NG}}^{\mathrm{ER}}$, shown in table 3.5, are identical with the ones derived from the empirical fit model only. The NR background is not listed in this table, as at this energy it is negligible compared to the contribution of the ER background in the high energy region. Both models, the box model and the combined model, show an underprediction of the background in the studied sideband. The larger number of observed events for different ER rejection levels are correlate since for example the region defined by the 99.5 % rejection level includes both other regions. The probability of observing $\geqslant 3$ ($\geqslant 6$) events according to a Poisson distribution with a mean value of $\lambda = 1$ ($\lambda = 3$) is ~ 8 %. In case of the box model the underprediction is less significant due to its slightly higher prediction of ~ 4 events (at 99.5 % ER rejection). In this case the probability of observing $\geqslant 6$ events considering the prediction of ~ 4 events is ~ 21 %. The reason for the difference between the two models is that in the energy range (30–100) PE the Gaussian parametrization of the ER band does not work as well as in the range (3–30) PE, leading to an underestimation of the Gaussian leakage into the NR band. This, however, does not affect the box model since it does not rely on the assumption that the ER band can be parametrized by a Gaussian function. Thus the discrepancy between model and observation is probably due to a combination of statistical fluctuations and an uderprediction of the Gaussian leakage in the energy range of the side band, which is not the case in the benchmark WIMP region.

The issue of the underpredicion of the Gaussian leakage described above demonstrates the advantage of the box model. In order construct the fit model one needs to make assumptions on the shape of the ER background, which might introduce systematic uncertainties. The box model on the other hand only relies on the assumption that at low energies the ER background in dark matter data can be well represented by calibration data (which also applies for the fit model). Thus the box model is more robust against systematic uncertainties. Nevertheless, for the profile likelihood analysis a two dimensional model is needed and due to the physical motivation of the AC model

ER rejection level	**Prediction box model**	**Prediction $\mathbf{f_{G}^{ER} + f_{NG}^{ER}}$**	**data**
99.5 %	3.7 ± 0.3 events	2.9 ± 0.3 events	6 events
99.75 %	2.1 ± 0.2 events	1.6 ± 0.2 events	4 events
99.9 %	1.0 ± 0.1 events	0.9 ± 0.1 events	3 events

Table 3.5: Comparison of the run III ER background predictions from the box model (see section 3.4) and the Gaussian plus non-Gaussian model $f_{\mathrm{G}}^{\mathrm{ER}} + f_{\mathrm{NG}}^{\mathrm{ER}}$ (see section 3.6) in the sideband defined by the energy interval 30 PE < cS1 < 100 PE.

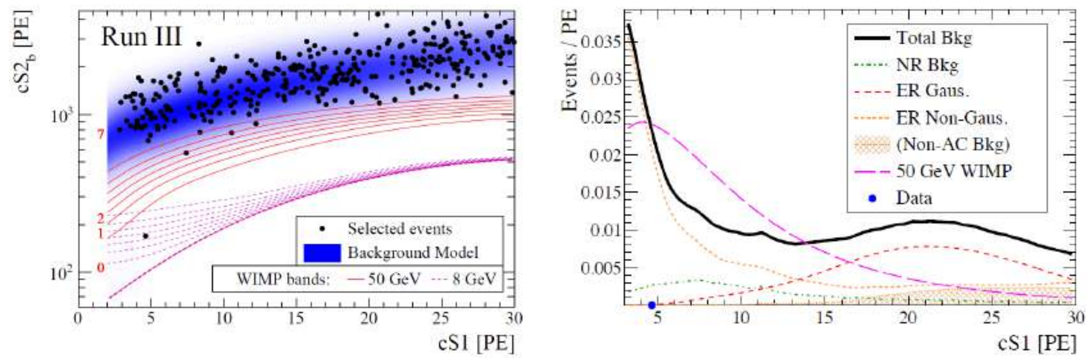

FIGURE 3.21: **(Left)** Example signal bands based on SI signal models for WIMP masses of $8\,\mathrm{GeV/c^2}$ (purple dashed lines) and $50\,\mathrm{GeV/c^2}$ (red solid lines with numbered labels). The shape of the background model is shown with a (blue) linear color scale. The run III science data are overlaid for reference. **(Right)** Expected event rates for profile likelihood band 0 from figure on the left for a $50\,\mathrm{GeV/c^2}$ WIMP and an assumed SI cross section of $\sigma_{\mathrm{SI}} = 10^{-45}\,\mathrm{cm^2}$ (long-dashed magenta line). The background contributions of run III from NR background, Gaussian leakage and non-Gaussian leakage (non solid colored lines) are shown together with their sum (solid black line). The non-Gaussian component consists of the AC-model (orange dashed) and the non-Gaussian fit model (diagonal line filled area) as described in the text. Figures from [75].

(section 3.6) the combined model (see equation (3.10)) is used as input instead of the empirical fit model only (section 3.5).

3.8 Profile likelihood analysis

The combined data of all three dark matter runs is analyzed by means of a profile likelihood (PL) ratio test statistic [136]. This section describes how the background model and its uncertainty are implemented in the analysis. The detailed procedure of the PL method is described in [137]. As in this reference, the S2 vs. S1 spectra are divided into eight bands in such a way that each band contains an equal number of expected signal events. In contrast to the procedure in reference [137], the banding is now based on a two dimensional signal model instead of AmBe calibration data, which already incorporates the combined acceptance of all applied selection criteria. As the distribution of the signal depends on the WIMP mass, this procedure is repeated for each mass m_χ. The bands for a WIMP mass of $8\,\mathrm{GeV/c^2}$ and $50\,\mathrm{GeV/c^2}$ are shown in figure 3.21 (left).

The likelihood function for each run i is then given by:

$$\mathcal{L}^i = \mathcal{L}_1^i(m_\chi; \sigma, N_b^i, \epsilon_b^{i,j}, t_{\mathcal{L}eff}, t_{Q_y}) \times \mathcal{L}_2^i(\epsilon_b^{i,j}), \tag{3.11}$$

where the extended likelihood function $\mathcal{L}_1^i$ contains the product over all bands j. $\epsilon_b^{i,j}$ is the background nuisance parameter for each band j, which is derived from the background

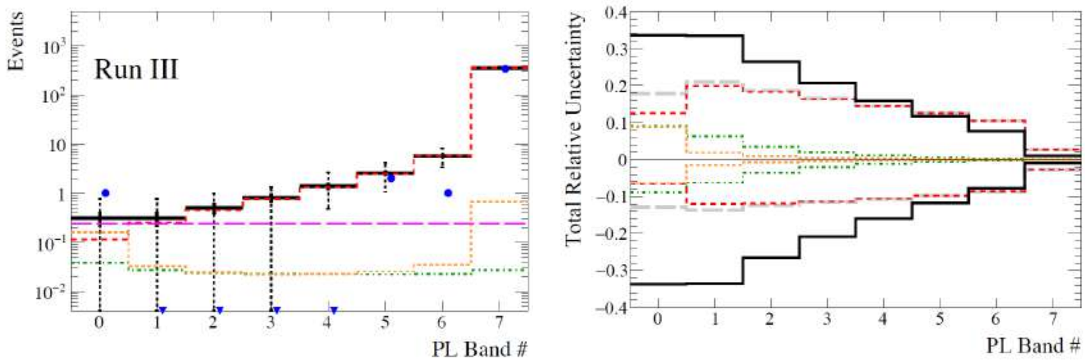

FIGURE 3.22: **(left)** Integrated event rates for each PL band assuming a 50 GeV/c^2 WIMP at $\sigma_{\mathrm{SI}} = 10^{-45}$ cm^2 in run III (long-dashed magenta line). The banding is similar to figure 3.21 (left). The total background is shown in black with error bars showing the 68 % Poisson probability region for the expectation. The individual components are the Gaussian ER band (red dashed), the non-Gaussian component (orange dashed) and the NR background (green dashed). **(right)** Total uncertainty for each background component and their quadrature sum (long-dashed gray line) in run III. The individual background components are the same as described above for the left figure. The Poisson error defined from ER calibration data (solid black line) is included in order to visualize the constraint term in equation (3.12). Figures from [75].

model. The background distribution along the cS1 axis (see black line in figure 3.21, right) is considered in the likelihood function for each band. The background distribution along cS2$_{\mathrm{bot}}$ is taken into account to some extend by the banding procedure since the expected background depends on the band. This can be seen in figure 3.22 (left) where the different background contributions in each band are shown for a WIMP mass of 50 GeV/c^2. By construction of the bands the expected signal (long-dashed magenta line) is the same in all bands. Due to the Gaussian distribution of the ER band the expected background is increasing towards PL band number seven which is closest to the ER bulk. The data points are shown as blue points.

The uncertainties of the background model, shown in figure 3.22 (right) are taken into account by varying $\epsilon_b^{i,j}$ within the constraints

$$\mathcal{L}_2^i = \prod_j \mathrm{Poiss}(m_b^{i,j} | \epsilon_b^{i,j} M_b^i), \tag{3.12}$$

where $m_b^{i,j}$ is the number of calibration events in band j and M_b^i the total number of calibration events. This parametrization of the uncertainty has been cross-checked by studying the systematic error of each background component and calculating their quadratic sum. As shown in figure 3.22 (right) the Poisson error overestimates the propagated errors and thus is conservatively used for this analysis.

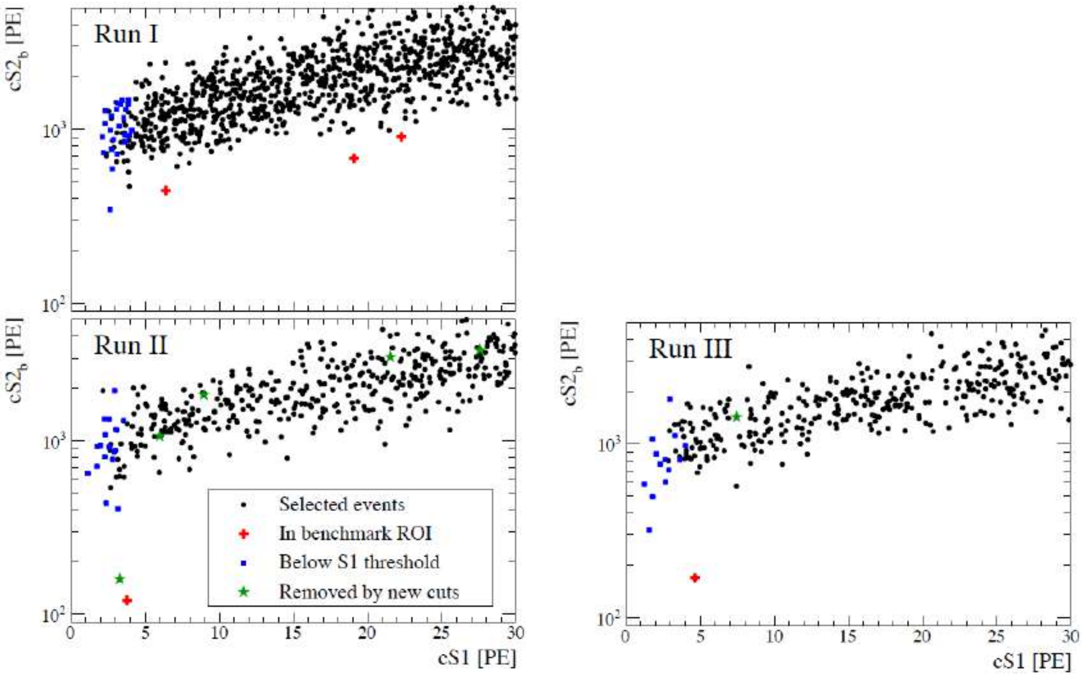

FIGURE 3.23: The $cS2_{bot}$ vs. cS1 for runs I, II and III science data passing all selection criteria (black circles; red crosses for dark matter candidates in the ROI). Events that fall below the S1 threshold of S1 = 3 PE (blue squares) are not used in the analysis. Events that were removed by the new "high S1 rate" and "improved S2 classification" cuts are also shown (green stars). The total number of events is summarized in table 3.1 on page 37. Figures from [75].

3.9 WIMP search results

For the profile likelihood analysis the combined background model defined in equation 3.10 has been used. A summary of the background predictions of all background components of this model and for all runs can be found in table 3.6. These predictions refer to the region of interest defined by the energy interval (3–30) PE, the 99.75 % ER rejection line and the lower $3\,\sigma$ quantile of the AmBe neutron calibration data. The NR background prediction in this table is taken from the simulation discussed in section 3.5. After unblinding run III and applying all selection criteria introduced in section 3.2 one event is observed in the region of interest, which is in good agreement with the background expectation of 1.0 ± 0.2 event. Due to the revised data selection, one of the two candidate events of run II, published in [86], is removed by the new data quality cut which excludes periods that show unusual high rates of lone S1 peaks (see section 3.2). The resulting observation of one event is still in agreement with the background expectation of 1.7 ± 0.3. In run I the same 3 events are observed as in [123], which is also close to the background expectation of 3.9 ± 0.5 events. The final selection of single scatter events in runs I, II and III are shown in figure 3.23.

By combining all three runs a total exposure of 17.6 tons $\times$ days has been accumulated during 477 live days spread over a time period of $\sim$ 4 years. The total number of

Run #	$\mathbf{f_{G}^{ER}}$ **[events]**	$\mathbf{f_{NG}^{ER}}$ **[events]**	**NR background [events]**	**Total background [events]**	**data [events]**
Run I	2.49 ± 0.47	1.27 ± 0.21	0.11 ± 0.08	3.9 ± 0.5	3
Run II	0.92 ± 0.21	0.58 ± 0.14	0.17 ± 0.12	1.7 ± 0.3	1
Run III	0.73 ± 0.17	0.19 ± 0.03	0.09 ± 0.07	1.0 ± 0.2	1

TABLE 3.6: Summary of background predictions and observed data for all three runs in the benchmark region of interest defined by the energy interval (3–30) PE, the 99.75 % ER rejection line and the lower $3\,\sigma$ quantile from AmBe calibration data.

5 observed events is consistent with the expected background level of 6.6 ± 0.6. By analyzing the total exposure by means of the PL analysis described in the previous section, a limit on the SI WIMP-nucleon cross section at 90 % confidence level is derived and shown in figure 3.24. The null result from this analysis confirms the absence of a WIMP dark matter signal. The XENON100 limit on the SI WIMP-nucleon cross section is improved by a factor of 1.8 at 50 GeV/c^2 with respect to the previous analysis of run II [86].

Furthermore, using the same statistical approach, improved upper limits on the SD WIMP-proton and WIMP-neutron cross sections are placed as shown in figure 3.25. At 50 GeV/c^2 the limit for the coupling to protons is improved by a factor of 1.7 and the coupling to neutrons by a factor of 1.8 with respect to the previously published XENON100 limits in [124].

By adding the third run to the previous run II the data taking period is increased by 271 days, which increases the sensitivity of the search for an annual modulation of the

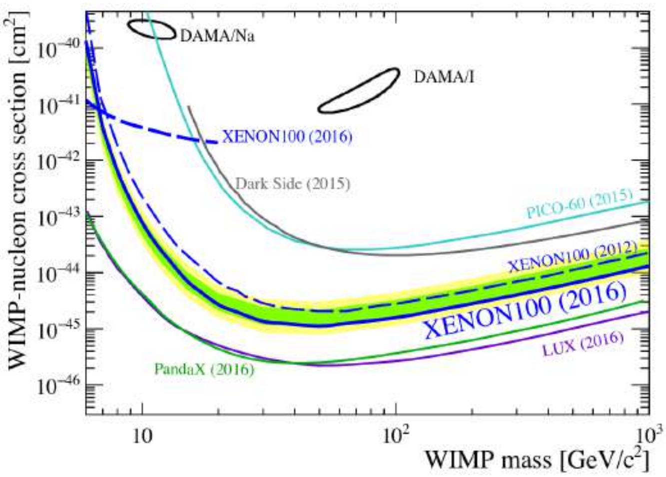

FIGURE 3.24: Spin-independent cross section limit at 90 % CL (blue line) and $1\,\sigma$ (green band) and $2\,\sigma$ (yellow band) expected sensitivity regions from the combined analysis of the three XENON100 science runs. For comparison, a subset of other experimental limits (90 %CL) and detection claims ($2\,\sigma$) are also shown [53, 55, 80, 86, 87, 138, 139]. Figure from [75].

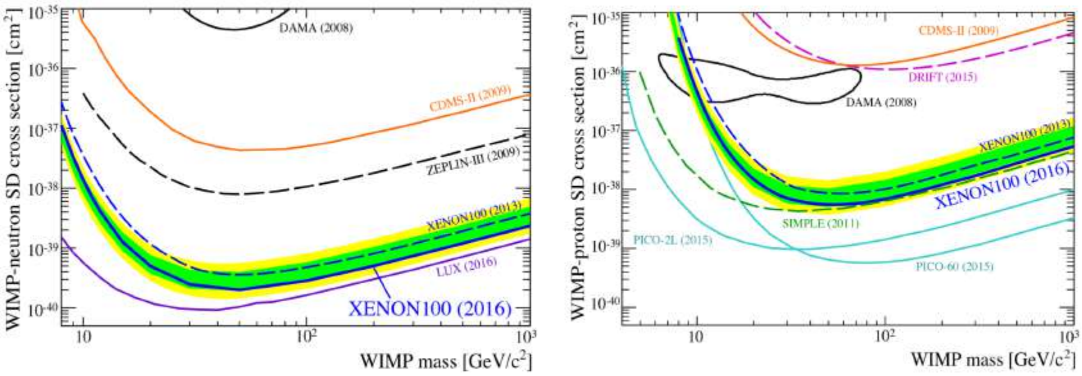

FIGURE 3.25: Spin-dependent cross section limit at 90 % CL (blue line) and 1 σ (green band) and 2 σ (yellow band) expected sensitivity regions from the combined analysis of the three XENON100 science runs. The left (right) panel shows the individual neutron (proton) only cross-sections. For comparison, other experimental limits (90 % CL) and detection claims (2 σ) are also shown [47, 50, 59, 124, 138, 140–143]. Figure from [75].

event rate in the ER background data. The corresponding analysis, previously published based on run II in [125], has been updated in [144].

Considering the null result of this analysis as well as even more stringent limits from other experiments [53, 80] it becomes clear that larger detectors at the ton-scale are required in order to potentially discover dark matter. Therefore, the first ton-scale LXe dark matter detector, XENON1T, has been constructed by the XENON collaboration. Currently the experiment is acquiring science data and a first result is expected soon.

Chapter 4

Magnetic inelastic dark matter interactions in XENON100

In the field of direct dark matter searches there is the longstanding detection claim by the DAMA/LIBRA collaboration [127]. They operate highly radiopure sodium iodide crystals with which they measure an annual modulation signal at a significance of $9.3\,\sigma$. This signal, however, is in conflict with the limits on the dark matter interaction rate from XENON100 [75], presented in the previous chapter, as well as from other direct dark matter experiments [53, 80]. Several alternatives to the classical WIMP scenario have thus been proposed in order to reconcile the null results of these experiments with DAMA/LIBRA. One of these models is magnetic inelastic dark matter (MiDM) proposed by Chang et al. [145].

In this chapter the first search for dark matter-induced delayed coincidence signals in a dual phase xenon time projection chamber is presented. This analysis uses a 224.6 day exposure from XENON100 science run II [86]. The MiDM model is described in section 4.1, the expected event rate is discussed in section 4.2 and the selection criteria used in the analysis of the data as well as their acceptance are introduced in section 4.3. The efficiency simulation of detecting the MiDM signature is described in section 4.4 and finally the result is presented in section 4.5.

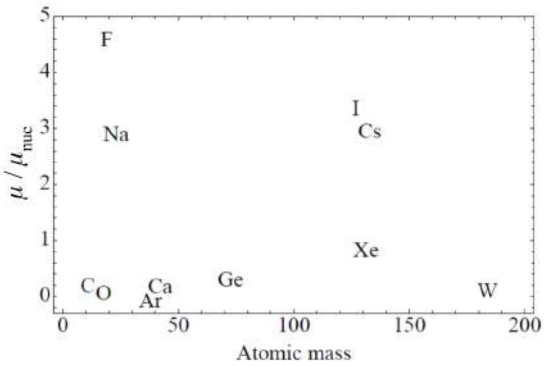

FIGURE 4.1: Weighted-atomic mass and weighted-magnetic dipole moment μ in units of the nuclear magneton μ_{nuc} of various dark matter search targets (C, O and Ca, Ar have been shifted slightly so as not to overlay each other). Figure from [145].

4.1 The magnetic inelastic dark matter model

The MiDM model approaches the discrepancy between the modulation signal of DAMA/LIBRA and the null results of other experiments by looking at the properties of the different detector targets and analyzing how they could influence the expected event rate in the detector. As shown in figure 4.1, iodine, used in DAMA/LIBRA, distinguishes itself from most other targets by its high atomic mass and high nuclear magnetic moment. These properties enhance the signal of MiDM compared to other targets, such as xenon. Similar to inelastic dark matter (iDM) [146], MiDM is based on the following three assumptions:

1. There is an excited WIMP state $\chi^{\star}$ with a corresponding mass splitting $\delta \sim \overline{\mu} v^2$, with the reduced WIMP-nucleus mass $\overline{\mu}$ and the WIMP velocity v.
2. Inelastic scattering against the nucleus $\chi + N \longrightarrow \chi^{*} + N$ has to be allowed .
3. Elastic scattering $\chi + N \longrightarrow \chi + N$ must be forbidden or highly suppressed.
4. It is assumed that WIMPs have a non-zero magnetic dipole moment μ_{χ}.

The finite mass splitting δ requires a minimal velocity for a WIMP to scatter off a nucleus, given by

$$v_{\mathrm{min}} = \frac{1}{\sqrt{2 M_N E_{\mathrm{nr}}}} \left(\frac{M_N E_{\mathrm{nr}}}{\overline{\mu}} + \delta \right). \tag{4.1}$$

M_N is the mass of the target nucleus, E_{nr} the recoil energy and $\overline{\mu}$ is again the reduced mass of the WIMP-nucleus system. This restriction favors heavy targets such as iodine used in DAMA/LIBRA, as the WIMP spectrum gets shifted to higher energies. Due to the magnetic dipole moment of the WIMP the model features dipole-dipole (DD) as well as dipole-charge (DZ) interactions between the WIMP and the target nucleus. These interactions favor iodine thanks to its large nuclear magnetic moment compared to most targets typically used in dark matter experiments. Taking into account the high mass number and the large magnetic moment of iodine, MiDM opens up new parameter space for the DAMA/LIBRA modulation signal which is not in conflict with other null results [145, 147].

MiDM interactions produce two distinct signatures. The first is a single-scatter nuclear recoil signal from the WIMP-nucleus interaction. Because of equation (4.1) this signal has a higher mean recoil energy E_{nr} than the "standard" spin-independent scatter process. The second signature is the de-excitation of the WIMP after a lifetime $\tau = \pi/(\delta^3 \mu_\chi^2) \approx \mathcal{O}(\mu\mathrm{s})$. During this period, the WIMP travels a distance of $\mathcal{O}(\mathrm{m})$ given the mean velocity of the Sun with respect to the WIMP halo. The de-excitation leads to the emission of a $\mathcal{O}(100\,\mathrm{keV})$ photon which can scatter off the dark matter target as well, inducing an electronic recoil signal. This combination of a low-energy nuclear recoil followed by a significantly larger electronic recoil produces a unique double-scatter signature. The rather large size of the cylindrical XENON100 TPC ($\sim$30 cm diameter and height) allows the first-ever search for these signatures, as illustrated in figure 4.2. Thanks to the low background expectation for this channel, the fiducial target could be increased to 48 kg which is 40 % more than employed for previous searches using the same dataset [86, 125, 126], thereby increasing the detection efficiency for the MiDM-interaction. In order to compare our result to the DAMA/LIBRA signal the analysis is focused on two WIMP masses, 58.0 GeV/c^2 and 122.7 GeV/c^2, which correspond to the best-fit results from [147] to explain the DAMA/LIBRA modulation within the MiDM model. The first mass yields the best fit for an iodine quenching factor of $Q_{\mathrm{I}} = 0.09$ [148], the second one for a more recently measured value of $Q_{\mathrm{I}} = 0.04$ [149].

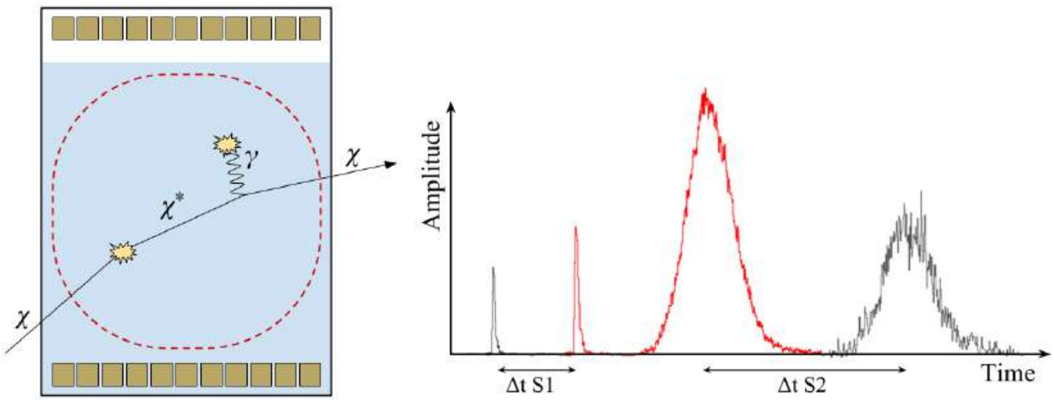

FIGURE 4.2: **(Left)** The expected signature from the interaction of magnetic inelastic dark matter consists of a primary WIMP-nucleon scattering (NR signal) and the subsequent decay of the excited WIMP, leading to a γ-emission (ER signal in TPC). In the analysis both interactions have to happen within the 48 kg fiducial volume illustrated by the red dashed line. **(Right)** Illustration of the expected PMT waveform corresponding to the interaction shown on the left. Peaks corresponding to the NR (ER) interaction are shown in black (red). The narrow peaks on the left are S1 signals, the wider ones on the right S2 signals. The first S1 peak always corresponds to the NR interaction.

4.2 Expected event rate

MiDM is expected to scatter off the target nuclei with a rate given by equation (4.2) [150], where m_χ denotes the dark matter mass, m_N the mass of the target nucleus and $f(\mathbf{v})$ the WIMP velocity distribution. The local dark matter density is taken to be the standard value of $\rho_{DM} = 0.3\,\mathrm{GeV/cm^3}$ [34] . Finally the term $\frac{d\sigma}{dE_{\mathrm{nr}}}$ represents the differential cross-section for MiDM-nucleus scattering, consisting of the DD and the DZ contributions:

$$\frac{dR}{dE_{\mathrm{nr}}} = \frac{\rho_0}{m_N m_\chi} \int_{v_{min}}^{v_{max}} v f(\mathbf{v}) \frac{d\sigma}{dE_{\mathrm{nr}}} d^3v, \tag{4.2}$$

$$\frac{d\sigma}{dE_{\mathrm{nr}}} = \frac{d\sigma_{DD}}{dE_{\mathrm{nr}}} + \frac{d\sigma_{DZ}}{dE_{\mathrm{nr}}}. \tag{4.3}$$

The complete expression of the two contributions (DD and DZ) are [145]

$$\frac{\mathrm{d}\sigma_{DD}}{\mathrm{d}E_{\mathrm{nr}}} = \frac{16\pi\alpha^2 m_N}{v^2} \left(\frac{\mu_N}{e}\right)^2 \left(\frac{\mu_\chi}{e}\right)^2 \left(\frac{S_\chi+1}{3S_\chi}\right) \left(\frac{S_N+1}{3S_N}\right) F_D^2(E_{\mathrm{nr}}), \tag{4.4}$$

$$\begin{aligned} \frac{d\sigma_{DZ}}{dE_{nr}} = \frac{4\pi Z^2\alpha^2}{E_{nr}} \left(\frac{\mu_\chi}{e}\right)^2 \Bigg[1 - \frac{E_{nr}}{v^2}\left(\frac{1}{2m_N} + \frac{1}{m_\chi}\right) \\ - \frac{\delta}{v^2}\left(\frac{1}{\mu} + \frac{\delta}{2m_N E_{nr}}\right)\Bigg] \left(\frac{S_\chi + 1}{3S_\chi}\right) F^2(E_{nr}), \end{aligned} \tag{4.5}$$

where μ_χ is the magnetic dipole moment of the WIMP and μ_N the magnetic dipole moment of the target nucleus. In the case of xenon there are two isotopes with a non-zero magnetic moment, ^{131}Xe and ^{129}Xe, which make xenon sensitive to DD interactions. Nevertheless, in contrast to iodine, DD coupling is subdominant for xenon targets and DZ scattering contributes roughly 80 % to the total rate [151]. $F^2(E_{\mathrm{nr}})$ is the Helm form-factor [150] and $F_D^2(E_{\mathrm{nr}})$ the magnetic dipole form-factor. The spin of the WIMP is set to $S_\chi = 1/2$, α denotes the fine structure constant and S_N is the nuclear spin of xenon.

The three free parameters in the analysis are the WIMP's mass m_χ, magnetic dipole moment μ_χ and mass splitting δ. The expected energy spectrum for a given set of parameters $(m,\ \mu_\chi,\ \delta)$ is calculated as in [147], using a modified Mathematica notebook originally provided by the authors of [152, 153].

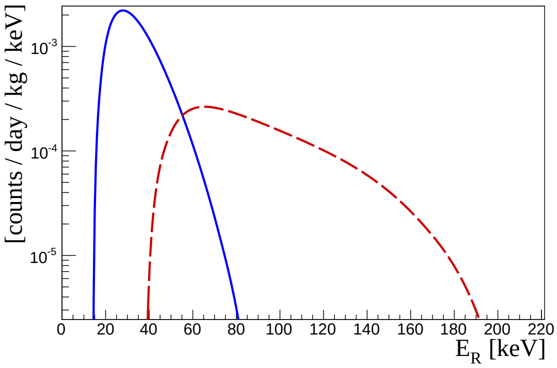

FIGURE 4.3: Expected energy spectra in counts per day (cpd) per kg and keV for the two sets of parameters (m_χ, μ_χ, δ), corresponding to the benchmark cases 1 (blue) and 2 (red). The energy spectrum is calculated using the software tools from [147] and agrees with the distributions shown in their publication.

Figure 4.3 shows the expected nuclear recoil energy spectra for the two benchmark cases corresponding to the DAMA/LIBRA best fit values for the different quenching factors Q_I:

1. $Q_\mathrm{I} = 0.09$: $(m_\chi = 58.0\,\mathrm{GeV/c^2},\ \mu_\chi = 0.0019 \cdot \mu_\mathrm{nuc},\ \delta = 111.7\,\mathrm{keV})$
2. $Q_\mathrm{I} = 0.04$: $(m_\chi = 122.7\,\mathrm{GeV/c^2},\ \mu_\chi = 0.0056 \cdot \mu_\mathrm{nuc},\ \delta = 179.3\,\mathrm{keV})$,

with the nuclear magneton μ_nuc. Both spectra agree with the ones presented in [147] and start well above the XENON100 energy threshold of $6.6\,\mathrm{keV_{nr}}$ [86]. This analysis is thus not limited by the lower energy threshold. For the two cases shown in figure 4.3 the expected number of events before applying any selection cuts (beside a 48 kg fiducial volume cut for the NR interaction) can be calculated by integrating the energy spectrum in the considered energy range of $(10 - 200)\,\mathrm{keV}_{nr}$. For the full exposure of $48\,\mathrm{kg} \times 224.6\,\mathrm{days} = 10.8\,\mathrm{t} \times \mathrm{days}$, the expected number of events is ~ 520 events for the first benchmark case and ~ 180 events for the second benchmark case. These numbers will be reduced mainly by the efficiency of also detecting the de-excitation inside the 48 kg fiducial volume as well as by the acceptances of the selection cuts introduced in the next section.

4.3 Data analysis

The MiDM event topology exploited in this analysis is a NR interaction followed by an ER induced by the photon of energy δ emitted in the WIMP de-excitation. Thus the following three chronological sequences of S1 and S2 signals can possibly occur in XENON100:

1. $\mathrm{S1_{NR}} \longrightarrow \mathrm{S1_{ER}} \longrightarrow \mathrm{S2_{NR}} \longrightarrow \mathrm{S2_{ER}}$
2. $\mathrm{S1_{NR}} \longrightarrow \mathrm{S1_{ER}} \longrightarrow \mathrm{S2_{ER}} \longrightarrow \mathrm{S2_{NR}}$

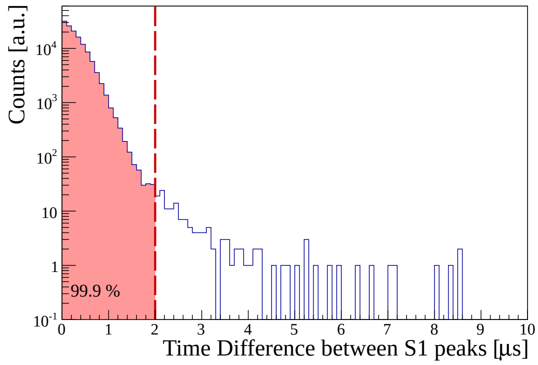

FIGURE 4.4: Time difference between the two S1 peaks for the first benchmark case. The maximal allowed time difference of 2 μs coveres 99.9 % of all potential signals. This distribution was generated using the efficiency simulation described in section 4.4.

3. $\mathrm{S1_{NR}} \longrightarrow \mathrm{S2_{NR}} \longrightarrow \mathrm{S1_{ER}} \longrightarrow \mathrm{S2_{ER}}$.

Since only single scatter NR events are expected in a “standard” WIMP analysis [86], the XENON100 data processor, xerawdp [77], does not search for further scintillation signals after the first large S2 peak. Thus, the second S1 peak in the third topology will be missed. Therefore, only the first two cases are considered in this analysis. The example shown in figure 4.2 would correspond to case 2.

This very distinct “delayed coincidence” event topology of two S1 signals followed by two S2 signals allows the removal of most of the backgrounds. The very abundant double scatter processes from Compton-scattering, γ-radiation, or neutrons are completely irrelevant for this analysis once a minimal time separation Δt between the two S1 peaks is required, as these peaks coincide for double scatters. We select events with $\Delta t > 50$ ns, the minimum time difference at which two S1 signals can be separated with 100% efficiency, as will be shown later. However, since xerawdp only separates S1 peaks with $\Delta t > 500$ ns, the requirement on the presence of a second S1 peak is omitted from the initial event selection and only enforced later, as described in section 4.3.3. The maximum Δt is 2 μs, which covers the longest possible track of a WIMP inside the target considering its velocity distribution and the dimensions of the detector (see figure 4.4). The signal loss due to these cuts, as well as the impact of ignoring the third event topology listed above, is taken into account by the efficiency simulation described in section 4.4.

In order to be able to separate the S2 peaks with high efficiency, a minimum time difference of 3.5 μs between the two charge signals is required (based on waveform watching campaigns). The signal acceptance loss due to this requirement is again taken into account by the efficiency simulation. We also place quality cuts on the minimum height and area of the smaller S2 peak and obtain the efficiency of these cuts from ^{241}AmBe neutron data (as the smaller S2 peak will certainly be from the NR interaction). The overall efficiency to detect two S2 peaks that meet these three requirements is > 94 %.

We additionally apply some of the data quality cuts, which were already used for previous analyses [86, 111] and which were now adapted for double-scatter interactions. Their acceptance is close to 100%. In this analysis, nuclear recoils are searched for in the energy range of $E_{\mathrm{nr}} = (9.7 - 200)\,\mathrm{keV_{nr}}$ and mass splittings in the energy range of $\delta = (30 - 200)\,\mathrm{keV_{ee}}$. Both energy scales are based on the S1 signal, with the relative scintillation efficiency $\mathcal{L}_{\mathrm{eff}}$ defined as in [86] and the electronic recoil scale from [29].

The interaction type (NR or ER) of the S1 peaks is determined by their time-order (NR followed by ER). The S2 peaks, on the other hand, can be assigned to their corresponding S1 peak based on their energy, this will be discussed in section 4.3.2. The pairing of the S1 and S2 peaks allows the discrimination between ER and NR interactions based on the charge to light ratio. Thus, we require additionally that the interaction leading to the first S1 must fall into the NR region, which has been defined based on ^{241}AmBe calibration data. A cut defining this region has a flat acceptance of 95%. In the following sections the analysis steps and cuts are discussed in more detail.

4.3.1 Requirement on S1 PMT multiplicity

A population of S1 peaks has been found in the run II dark matter data, selected for this analysis, where the scintillation light is only seen by few PMTs, which is unusual for S1 peaks. As shown in figure 4.5 this population lies outside the expected distribution of S1 peaks surviving the standard WIMP analysis cuts used in this analysis [75]. Further investigations show that the same population is also mainly seen by the top PMT array, illustrated in figure 4.6. These are both indications that these events are happening in the gas phase just below the top PMTs and thus are seen mainly by the top array and only by a few PMTs. In order to reject this population, a cut with an acceptance of 99 % has been defined based on the PMT multiplicity of S1 peaks shown by the red dashed line in figure 4.5.

4.3.2 Fiducial volume and energy cuts

Due to the specific signature of the MiDM model, gamma backgrounds originating from detector materials can be reduced to sub-dominant level (see section 4.3.7). Thus external background is not limiting this analysis. Therefore, the larger fiducial volume defined in [123] can be used. It contains 48 kg of xenon instead of the 34 kg target used in the single scatter dark matter search of [86]. Both interactions (NR and ER) are required to take place inside this fiducial volume. Using a larger volume enhances the sensitivity to MiDM thanks to the larger target mass for the initial interaction and the larger volume for detecting the de-excitation signal. The de-excitation of the WIMP is

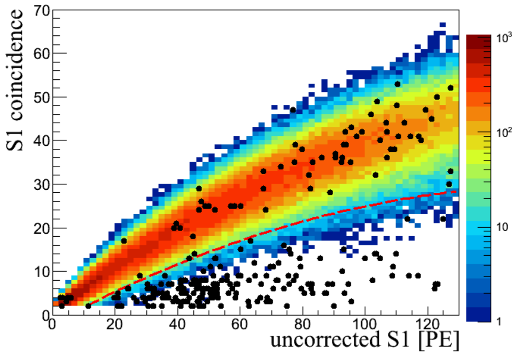

FIGURE 4.5: PMT multiplicity for S1 peaks as a function of uncorrected S1 energy for events passing all standard WIMP analysis cuts (colored histogram) overlaid by the events from the MiDM selection (black points). Below the 99 % quantile (red dashed line) a population of events can be seen outside the main distribution.

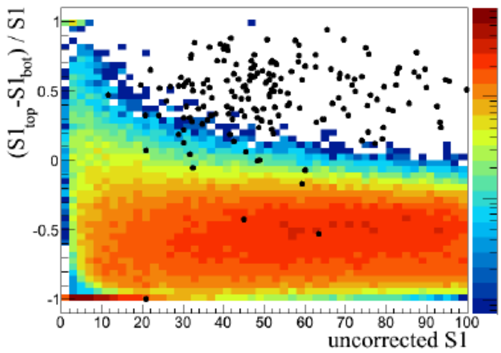

FIGURE 4.6: Fraction of S1 light seen by the top PMT and the bottom PMT array. The event population identified in figure 4.5 (black points) shows an unusually large fraction of the light seen by the top PMT array, indicating that these are interactions happening in the gas phase. The colored histogram again shows the distribution of events passing all standard WIMP analysis cuts.

expected to happen shortly after the primary interaction and most of the time the data processor will not be able to separate the two S1 peaks. This means that the larger S1, originating from the de-excitation, has to serve as t_0 in order to calculate the drift time and consequently the z-position for both interactions (the NR and the de-excitation). However, the fact that the processor cannot separate the two S1s means that their time difference is < 500 ns. Therefore using the larger S1 in order to calculate the z-coordinate for both events will introduce only a small error ($\sim 0.5\,\mu\text{s} \cdot 1.73\,\text{mm}/\mu\text{s} = 0.8\,\text{mm}$) and the fiducial volume cut can still be applied to both interactions.

Finally, a lower and an upper energy boundary is applied to both S2 peaks:

- **energy cut on larger S2:** $3000\,\text{PE} < \text{cS2}_{\text{bot}} < 90000\,\text{PE}$.
- **energy cut on smaller S2:** $\text{cS2}_{\text{bot}} < 3000\,\text{PE}$,

where cS2_{bot} denotes the bottom array S2 signal corrected for the finite electron life time. Usually the S1 signal is used as a proxy for the energy (such as in [75]). However, in our case the energy cuts are defined on the S2 peaks, since the two S1 peaks might be merged by the data processor and initially not both energies are available. The upper boundary on the smaller S2 is chosen such that 100 % of NR events are accepted up to $S1 = 154\,\text{PE}$ (see figure 4.7). This corresponds to an energy of $200\,\text{keV}_{\text{nr}}$ and thus the full energy ranges of the expected NR spectrum for both benchmark cases (shown in figure 4.3) are covered.

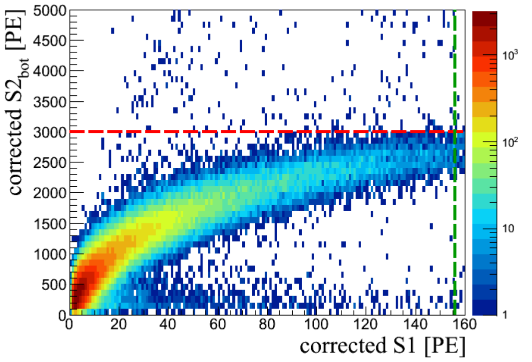

FIGURE 4.7: Distribution of nuclear recoil events from AmBe calibration data with the maximum allowed NR S1 energy indicated by the dashed green line. The maximum energy of 3000 PE of the smaller S2 peak is shown by the dashed red line.

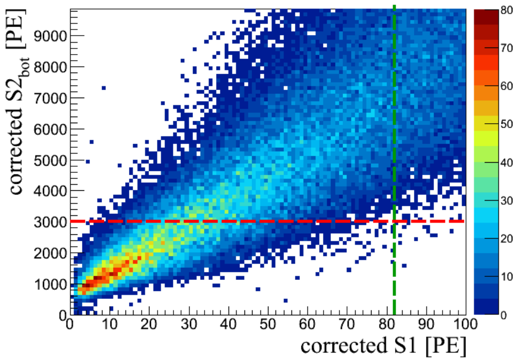

FIGURE 4.8: S1 vs. S2 distribution from ER calibration data. The lower energy cut on the larger S2 peak (de-excitation) of 3000 PE is indicated by the red dashed line. In order to always get the corresponding S1 peak the lower S1 energy limit is chosen to be 82 PE which corresponds to an energy of 30 $\mathrm{keV_{ee}}$.

Also requiring that the larger S2 peak is greater than 3000 PE ensures that it corresponds to the ER interaction, while the smaller S2 corresponds to the NR interaction. Since it is known that the first (second) S1 peak corresponds to the NR (ER) it is now possible to pair S1 and S2 peaks which is needed to discriminate between ER and NR interactions. The lower energy limit on the charge signal of the de-excitation also defines the minimal δ that can be probed. In order to be sure to always detect the S1 as well as the S2 of the ER interaction, the lowest probed δ in this analysis is chosen to be $\delta = 30\,\mathrm{keV_{ee}}$. This 30 $\mathrm{keV_{ee}}$ corresponds to an S1 energy of 82 PE [29], for which the corresponding S2 is always larger than 3000 PE, as can be seen in figure 4.8. The upper boundary on the larger S2 (which is from the de-excitation) is defined on the 236 keV line from the activated xenon and is chosen such that it is possible to probe mass splittings up to $\delta = 200\,\mathrm{keV_{ee}}$. This is high enough in order to cover both benchmark cases. A summary of all cuts used in this analysis is shown in table 4.1. The number of remaining events after applying the basic S1 and S2 cuts, after adding the fiducial volume cut and after applying all cuts is summarized in table 4.2. At this point all remaining events have two S2 peaks that fit the energies expected from MiDM and at least one real S1 peak. However, they still are not searched for a second S1 peak, which will be discussed in the next section.

4.3.3 Searching for second S1 peak

The efficiency of xerawdp to separate two S1 peaks is 100 % if they have a time difference greater than 500 ns. The raw data of all remaining 2835 events (see table 4.2) is therefore searched for an additional scintillation signal preceding the largest S1 peak found by

Selection criteria	**Acceptance**
No signal in active xenon veto around TPC.	100 %
Rough energy boundaries for larger S1 peak, 2 PE < S1 < 700 PE.	100 %
Require signal in the top PMT array for both S2 peaks.	100 %
Remove events with more than two S2 peaks.	100 %
Drift time should not be bigger than maximum drift time.	100 %
Energy boundaries on larger S2 (3000 PE < $cS2_{bot}$ < 90000 PE).	100 %
Energy boundary on smaller S2 ($cS2_{bot}$ < 3000 PE).	100 %
Cut away S1 peaks only seen by few PMTs (gas events).	99 % by definition
Primary interaction has to fall into NR band.	95 % by definition.
S1 peak has to be seen in more than one PMT.	energy dependent, see section 4.3.6.
Threshold for S2 Height > 0.14 V.	
Threshold on both S2 peaks, S2 > 500 PE.	
Minimum time distance between S2 peaks of 3.5 μs.	see efficiency simulation, section 4.4
Fiducial volume cut (using larger S1 as t_0 for both interactions).	

Table 4.1: Summary of selection criteria used in this analysis.

Cut	**Remaining events**
S1 and S2 cuts	102758
+ fiducial volume cut	60699
+ Energy boundaries on S2 peaks	2835

Table 4.2: Remaining events after applying basic S1 and S2 cuts, after adding fiducial volume cut and after all cuts are applied.

the data processor using a custom developed code. Searching for a second, smaller S1 peak immediately ($\sim$ 30 ns) after the main S1 is not possible due to the decay of the primary scintillation signal and since the remaining waveforms often show some bipolar signals. This, however, does not affect the sensitivity of this analysis since the NR energy spectrum ends below the expected energy of the de-excitation. Thus the NR S1 peak has to be smaller and also has to come before the main S1 which corresponds to the larger ER signal. In order to search the raw data of the remaining events from table 4.2, a new processor has been developed based on the existing waveform viewer "Xedview". This modified Xedview (ModX) searches for excursions above a certain threshold in the sum waveform, as well as in all individual channels. As illustrated in figure 4.9 the search is performed in a time window up to 500 ns prior to the main S1 peak. In this time interval ModX uses a sliding window of 50 ns in which the following criteria have to be simultaneously fulfilled to claim the detection of a second, smaller S1 peak:

- **PMTs multiplicity** > 2 (within a window of 50 ns and excluding noisy PMTs)
- **peak height** > 70 **ADC counts** $\Leftrightarrow \sim 0.01$ V (in sum waveform)

While the multiplicity requirement is the same as used in [86], the minimal peak-height of 70 ADC counts is motivated by figure 4.10. This plot shows the S1 peak-maximum for events of at least 5 PE $\approx$ 10 $\mathrm{keV_{nr}}$ which is the lower limit for the integration of the NR

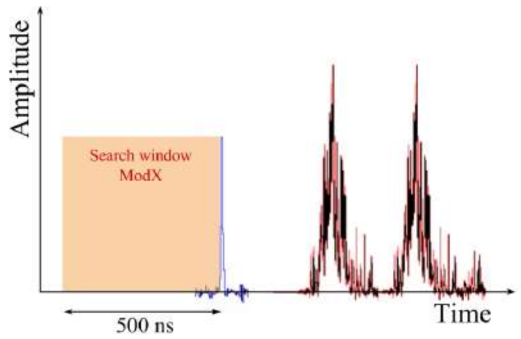

FIGURE 4.9: All events where only one S1 is found by the XENON100 data processor are specifically searched for a second S1 peak within 500 ns prior to the main S1 using the software tool ModX.

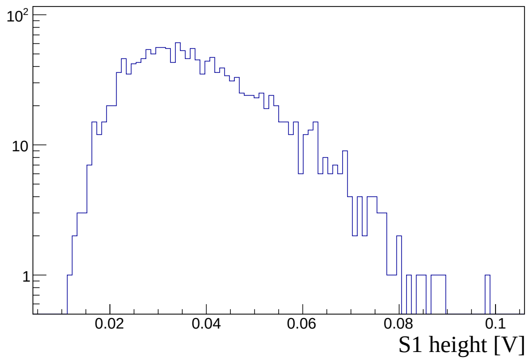

FIGURE 4.10: Height of S1 peaks with an energy of $5\,\mathrm{PE} < S1 < 10\,\mathrm{PE}$. It is always larger than 0.01 V, corresponding to 70 ADC counts.

energy spectrum. In addition ModX calculates the gain-corrected S1 area of the peaks by summing up all PMTs above the threshold in a window of ± 15 samples around the peak maximum (but not closer than 3 samples to the main S1 peak).

Similar to xerawdp, ModX will also lose efficiency in separating S1 peaks if their time difference Δt gets too small. Thus it is important to calculate the efficiency as a function of Δt. In order to do this two different populations of waveforms containing a single S1 peak are selected from ^{60}Co calibration data using all cuts from [86]. The two samples contain S1 peaks in the following energy ranges:

1. $5\,\mathrm{PE} < S1 < 10\,\mathrm{PE}$
2. $195\,\mathrm{PE} < S1 < 200\,\mathrm{PE}$.

They represent the extreme case of a large S1 signal from the de-excitation and a very small S1 belonging to the NR interaction, which should be the most difficult case to separate the two peaks. In a second step the waveforms are randomly stitched together (one low energy S1 preceding a high energy S1) while varying the time difference between the two peaks from 1 to 50 samples (corresponding to 10 to 500 ns). For each time difference 900 different waveforms are generated. Two example waveforms with different time differences can be found in figure 4.11. Finally, these waveforms are searched for the small S1 peak before the big S1 using ModX. The resulting peak finding efficiency as a function of the time difference is shown in figure 4.12. ModX is able to detect the first S1 peak with 100 % efficiency for time differences ≥ 4 samples. In the analysis, a larger minimal time difference of 5 samples = 50 ns is required and thus not affected by this efficiency. The loss of signal acceptance due to the minimal time difference is taken into account by the efficiency simulation described in section 4.4.

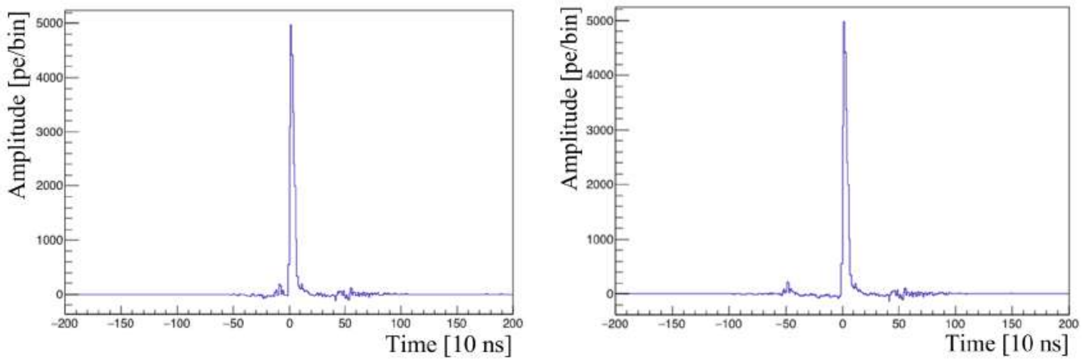

FIGURE 4.11: Artificially generated waveforms to test the efficiency of ModX in separating two S1 peaks depending on their time difference (see figure 4.12). In the two plots the same two S1 peaks are stitched together with a time separation of 10 samples (left) and 50 samples (right).

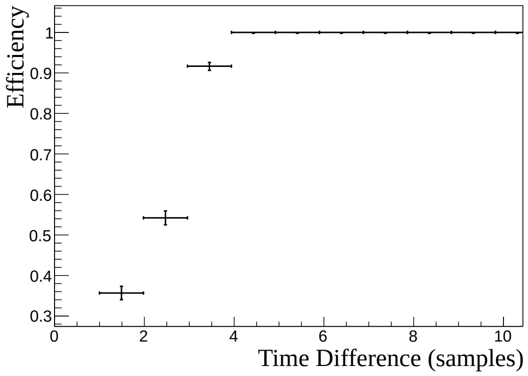

FIGURE 4.12: Peak finding efficiency of ModX as a function of time difference between the S1 peaks.

4.3.4 Efficiency of identifying both S2 peaks

Since the standard WIMP analysis searches for single scatters, the performance of xerawdp in detecting two S2 peaks in a single event had not yet been investigated. Especially after big S2 peaks (due to their photo-ionization tails) subsequent S2 peaks might be missed as xerawdp was not designed and tested for this kind of search. Figure 4.13 shows a typical waveform after a high-energy S2 peak. It can be seen that there are a lot of small S2 peaks (mostly single electron S2) that are missed by xerawdp. The basic principle of estimating the efficiency of the processor to find both S2 peaks is to search the sum waveforms of a subset of the data using a software tool and to check how many S2 peaks xerawdp finds and how many it misses. In the following, this process is described in more detail.

For the MiDM analysis it is not crucial to go to very small energies, and in order to ensure that the second S2 peak is found by xerawdp, the following two requirements on the S2 peaks are added:

- S2 Height $> 0.14\,\mathrm{V}$
- $\mathrm{S2} > 500\,\mathrm{PE}$

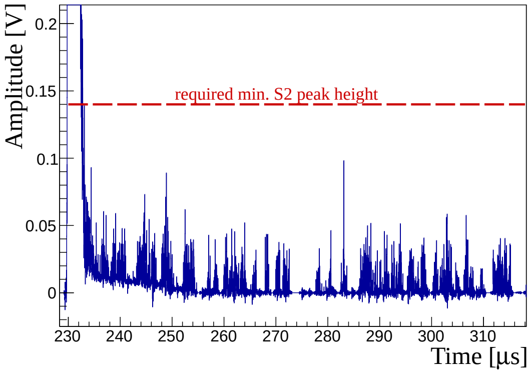

FIGURE 4.13: Typical waveform after a high energy S2 peak. The small S2 peaks after the main S2 are mainly due to single electron S2s and are often missed by xerawdp. Thus a minimum peak height of 0.14 V indicated by the red dashed line is required in order to get a higher efficiency of detecting the second S2 peak, even after large charge signals.

The height of the S2 is directly measured in the sum waveform. The S2 energy is approximated by converting the integral of the sum waveform into PE using the average PMT gain of $2 \cdot 10^6$. In a visual inspection of waveforms it has been determined that in many cases it is not possible to separate S2 peaks closer than $3.5\,\mu$s after a large S2 peak. Thus the time difference between the two S2 peaks is additionally required to be $\Delta t > 3.5\,\mu$s. The loss in signal acceptance due to this condition is $\sim 10\,\%$ and is taken into account by the efficiency simulation described in section 4.4.

The data used to extract the efficiency of identifying both S2 peaks is AmBe calibration data and the cuts are the same as for the MiDM analysis except that there is no requirement for a second S2 peak, as the second S2 peak might have been missed. The problem of missed S2 peaks is expected to be most prominent after high-energy S2 peaks and less dominant after low-energy S2s. Thus, the study is divided into two categories covering the whole energy range of this analysis:

1. $200\,\mathrm{PE} < \mathrm{cS2_{bot}} < 70000\,\mathrm{PE}$
2. $70000\,\mathrm{PE} < \mathrm{cS2_{bot}} < 90000\,\mathrm{PE}$

Table 4.3 shows the number of S2 peaks (besides the main S2) found in these events. The efficiency is calculated by dividing the number of peaks found by xerawdp by the total number of peaks fulfilling the above requirements. As expected for events with a large primary S2 the efficiency is lower because of the large tail in the waveform after those peaks. Since the difference is rather small, the efficiency is assumed to be 0.94 for the full energy range.

4.3.5 Result of data selection

After applying all selection criteria described above (see table 4.1), and after searching for a second S1 peak using ModX, there are four remaining events, shown in figure 4.14

$cS2_{bot}$ **Energy range**	**Peaks found by xerawdp (beside main S2)**	**Missed peaks**	**Calculated efficiency**
(70000–90000) PE	121	7	0.94 ± 0.02
(200–70000) PE	103	3	0.97 ± 0.02

TABLE 4.3: Efficiency of xerawdp of finding other S2 peaks beside the main S2 for two different energy ranges.

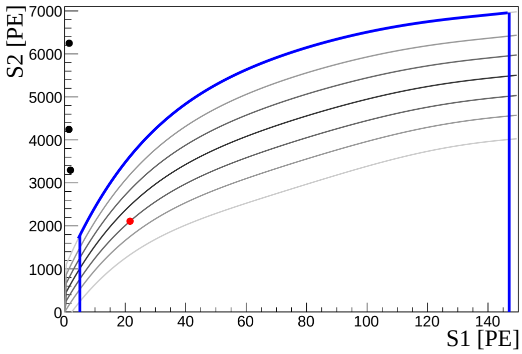

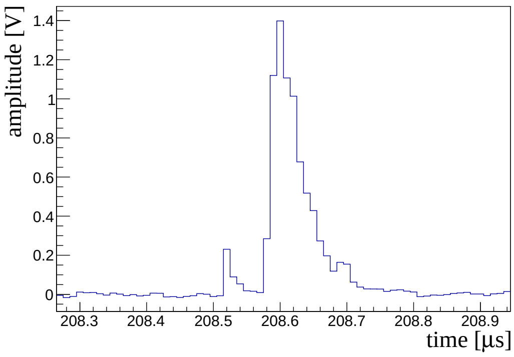

FIGURE 4.14: **(left)** The region of interest (ROI) for the NR signal of a MiDM interaction is defined by the 95% NR acceptance cut (top blue line) and the S1-energy interval (left and right). The gray lines show the ±20%, ±35% and ±45% quantiles of the NR region as defined by AmBe neutron calibration data. No events remain in the ROI after applying all cuts (on all four S1 and S2 peaks). Three events (black dots) appear at very low S1, outside of the ROI. Visual inspection indicates that their S1 peak is due to electronic noise. One event (red dot) lies inside the ROI but cannot be due to MiDM as it is kinematically forbidden due to it's high mass splitting. **(right)** Waveform of the leaking event from figure on the left (red point) showing the two successive S1 peaks. This event is kinematically forbidden due to its high mass splitting > 200 keV corresponding to the large second peak in this plot.

left. Three of them appear above the 95 % NR acceptance line and a visual inspection of their waveforms shows that the small "S1 peak" found by ModX is actually just noise. One event appears below the 95 % NR acceptance line. Its waveform is shown in figure 4.14 right. In this event there are indeed two S1 peaks. However, the larger S1 peak has a corrected energy of 630 PE (calculated by xerawdp). This corresponds to a mass splitting above 200 keV and is thus kinematically forbidden for WIMP masses of $m = 58$ GeV and $m = 122.8$ GeV. In summary, there are zero events left fulfilling all the requirements for MiDM with an S1 time difference of $50\,\text{ns} < \Delta t < 2\,\mu\text{s}$.

4.3.6 Cut acceptances

In contrast to most other cuts, the signal acceptances of the selection criteria on the S2 size and height depend on the S1 energy. Their acceptance is estimated using NR data from AmBe calibration, as in fact they only cut on the NR interaction since the S2 peak from the de-excitation has to be larger than $cS2_{bot} > 3000$ PE. The NR sample is selected using all selection criteria from [86] and the acceptance is derived as a function of S1

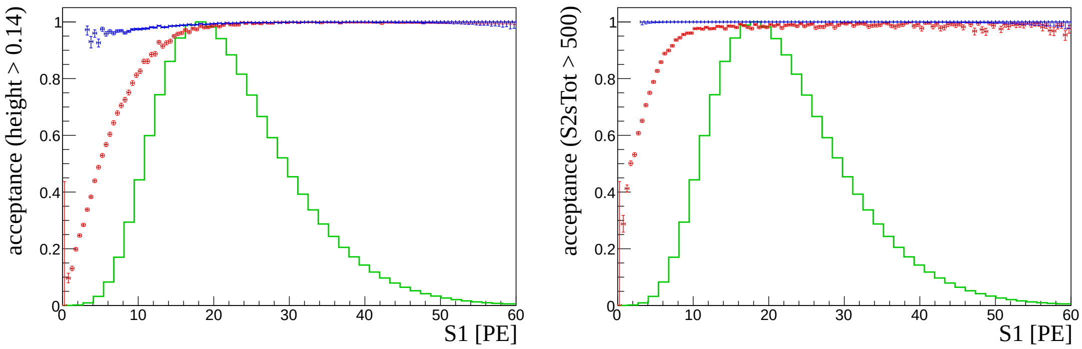

Figure 4.15: Acceptance of requirement on the height (left) and on the size (right) of the smaller S2 signal, derived using the signal model simulation of [75] (blue) and from AmBe calibration data (red). In green the expected NR energy spectrum of the first benchmark case is shown for comparison.

energy by calculating the fraction of events passing the criteria on the S2 size or height. The result is shown in figure 4.15 in red. The acceptance has been double checked for the considered parameter space based on the signal model simulation from [75] instead of AmBe data: with this simulation, S2-height vs. S1 and S2 vs. S1 spectra are generated using the MiDM energy spectrum from figure 4.3 as input. The acceptance based on the signal model is shown in figure 4.15 in blue. It can be seen that the acceptance derived from AmBe data is smaller than the one using the simulation and thus is more conservative. In the most extreme case the difference of the integrated energy spectrum after applying the acceptance of each method is no more than $\sim 6\,\%$. The impact of an acceptance increased by $6\,\%$ on the result of this analysis is very small and thus the more conservative acceptance derived on AmBe data is used as it is technically much more straightforward. The selection of the NR sample at low energies is already affected by the S2 threshold defined in [86]. Thus the acceptance of this threshold is taken into account as well. Furthermore, the requirement that an S1 has to be seen by more than one PMT is adopted from the standard single scatter WIMP analysis and its acceptance is taken from [86]. The combined cut acceptance, derived by multiplying the individual components, is shown in figure 4.16 in blue. The low-energy drop is due to the requirements on height and area of the smaller S2 signal. The constant acceptance loss at higher energies is mainly due to the efficiency to find two appropriate S2 peaks (94%) and the requirement that the first interaction falls into the NR region (95%). Since the expected NR spectra from MiDM are shifted to higher energies the low-energy acceptance-loss has only little impact on the analysis.

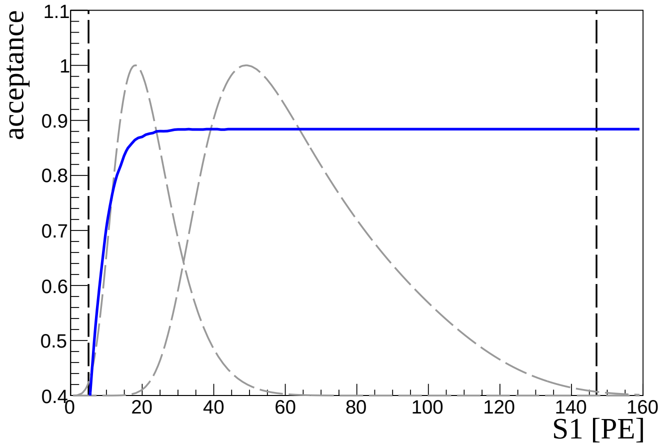

FIGURE 4.16: Combined cut acceptance as function of the NR interaction's light signal (blue). The expected MiDM spectra from figure 4.3 are shown for comparison by the gray dashed lines. The vertical lines indicate the analysis energy range of $E_{\mathrm{nr}} = (9.7 - 200)\,\mathrm{keV_{nr}}$.

4.3.7 Expected background

The following discussion of possible backgrounds that could mimic the expected signal from MiDM is partially based on the work of M. v. Sivers. In contrast to a profile likelihood analysis, the maximum gap method [154] used in this analysis does not require a background prediction. Nevertheless, it is important to estimate how many events that could mimic the MiDM signal are expected. In this section, possible sources contributing to the MiDM background are discussed and the expected number of events for the total exposure of 10.8 tons $\times$ days is estimated. A summary of the backgrounds surviving all selection criteria described above can be found in table 4.4. The individual processes are discussed in more detail below. In principle, these backgrounds could be further lowered by requiring a larger spatial distance between the two interaction vertices. However, due to the exponential decay time spectrum of the de-excitation, such a condition would significantly affect the detection efficiency.

Background source	**Expectation**
Pileup between NR and ER events	$\mathcal{O}(10^{-9})$ events
Pileup between two ER events	$\mathcal{O}(10^{-4})$ events
Pileup between ER double scatter events and lone S1	$\mathcal{O}(10^{-2})$ events
Kr-85 decay	$\mathcal{O}(10^{-9})$ events
^{212}BiPo and ^{214}BiPo decays	~ 0.16 events

TABLE 4.4: Summary of possible background sources and their estimated contribution.

Pileup between NR and ER events

One possible source of background is a random pile up of an actual NR interaction followed by an ER interaction. The rate of ER single scatter events can be estimated by applying the cuts for the MiDM event selection except that in this case only one S1 and one S2 peak is allowed. For our data set this results in 64896 events, corresponding to an ER single scatter rate of $\sim 3.4 \times 10^{-3}$ Hz (the exposure is 224.6 days). According to [86] the expected number of single scatter NR events in the 34 kg fiducial volume and an energy region of $(6.6 - 30.5)\,\mathrm{keV_{nr}}$ is $0.17^{+0.12}_{-0.07}$ events. This number has to be scaled to the 48 kg volume and extended up to 200 $\mathrm{keV_{nr}}$ which results in $\mathcal{O}(1)$ expected NR events in run II. This number is conservative since the energy spectrum of the NR-background is steeply falling at higher energies as can be seen in figure 3.10. Thus the expected number of accidental coincidence events within 2 μs between a single scatter NR and ER event is $\mathcal{O}(10^{-9})$, which is negligible.

Pileup between two ER events

This source of background is also caused by accidental pile up of events. However, this time two ER interactions are involved, which means that the first ER has to leak into the NR band in order to mimic a NR interaction. Based on the single scatter ER rate of 3.3×10^{-3} Hz from above the expected number of accidental coincidences within 2 μs in run II is $\mathcal{O}(10^{-4})$ events. This is negligible even without taking into account any ER/NR discrimination power.

Pileup between ER double scatter event and lone S1 peak

Another source of possible background is pileup between an ER double scatter event producing one S1 peak and two S2 peaks and a lone S1 peak (a S1 signal without a corresponding S2). In the accidental coincidence background model for the run combination described in section 3.6, the rate of lone S1 peaks in run II has been calculated to be ~ 4.4 Hz. After applying all cuts from this analysis there are 2835 events left, as shown in table 4.2. Even though some of those events might already have a second S1 peak, they mainly consist of events containing a single S1 and two S2 peaks. Thus, the expected number of this kind of accidental coincidences within 2 μs for run II is $\mathcal{O}(10^{-2})$ events. In fact, the contribution of this background is even smaller, as the first S1 peak paired with the smaller S2 has to mimic a NR interaction.

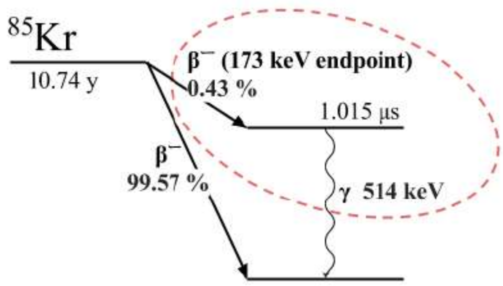

FIGURE 4.17: Decay scheme of ^{85}Kr. The potential background originates from the β-decay with an endpoint energy of 173 keV and its successive emission of a 514 keV gamma, marked by the dashed circle. The mean lifetime of this decay is comparable to the decay time of MiDM.

^{85}Kr decay

One major intrinsic background in XENON100 is ^{85}Kr which is present in $^{\mathrm{nat}}$Kr at a ratio of $^{85}\mathrm{Kr}/^{\mathrm{nat}}\mathrm{Kr} = 2\cdot 10^{-11}$ [155]. As can be seen in figure 4.17, ^{85}Kr decays into ^{85}Rb via β-emission in 99.57 % of the cases. In contrast to the standard WIMP analysis, this decay is not a problem for MiDM as it is removed by the requirement of two S2 peaks. However, with a branching ratio of 0.43 %, ^{85}Kr may also decay via a β-decay with an endpoint energy of 173 keV followed by emission of a 514 keV gamma (half-life 1.01 μs). In run II of XENON100 the typical atmospheric $^{\mathrm{nat}}$Kr/Xe concentration of ppm was reduced to (19 ± 4) ppt using cryogenic distillation [86]. The expected number of ^{85}Kr decays emitting a β and a delayed γ is estimated to be 15 events in the entire dataset. This number is further reduced by the following cuts:

- By linearly interpolating the position and resolution of the 236 keV and 662 keV peaks from activated xenon, the $\mathrm{cS2_{bot}} < 90000$ PE cut on the larger S2 is estimated to cut 6.3 σ below the 514 keV line. This leads to a suppression of the ^{85}Kr background by a factor of $\sim 10^{10}$.
- S1 time difference cut $50\,\mathrm{ns} < \Delta t < 2\,\mu\mathrm{s}$ removes 29 % of the ^{85}Kr events.
- The β decay from ^{85}Kr would have to leak in the NR region in order to mimic the primary NR scatter.

In summary, the expected background introduced by delayed coincidence decay from ^{85}Kr is $\mathcal{O}(10^{-9})$ events.

^{212}BiPo and ^{214}BiPo decay

Another background source are the decays from the ^{220}Rn and ^{222}Rn daughters. Possible sources of the intrinsic radioactive Rn are emanation from the detector components, and diffusion through the vacuum seals. The decay chain of ^{220}Rn (^{222}Rn) is shown in

Chain	**Isotope**	**Decay**	**Half-Life**	α **[MeV]**	β **Endpoint [keV]**	γ **[keV]**
^{220}Rn	^{212}Bi	$\beta^-(+\gamma)$	60.55 min	—	2252, 1525	727, 1620, ...
	^{212}Po	α	299 ns	8.785	—	—
^{222}Rn	^{214}Bi	$\beta^-(+\gamma)$	19.9 min	—	3270, 1540, 1505, ...	609, 1764, ...
	^{214}Po	α	163.6 μs	7.69	—	—

TABLE 4.5: Summarized decay modes of the ^{212}BiPo and ^{214}BiPo decay. Data from [156].

figure 4.18 with the relevant background (the "BiPo decays") coming from the consecutive decay of ^{212}Bi (^{214}Bi) and ^{212}Po (^{214}Po), summarized in table 4.5. By tagging their delayed coincidence signal we expect a total of 2400 (14000) events from ^{212}BiPo (^{214}BiPo) decays inside the 48 kg fiducial volume. These are conservative numbers due to the assumption of a uniform distribution of the interactions inside the TPC, although in reality most BiPo events are observed close to the cathode. These numbers are further reduced by the following cuts:

- The time difference cut on the S1 peaks $50\,\text{ns} < \Delta t < 2\,\mu\text{s}$ rejects 12 % of all ^{212}BiPo and 99.2 % of the ^{214}BiPo events.
- The β^- would have to leak into the NR region, which is suppressed by a factor of 0.27.
- The energy cuts, since especially the α-peaks have quite high energies and only a small fraction is leaking into the energy region considered in this analysis.

In order to get an estimate of the expected BiPo background a simulation has been performed in which S1 energies for the β and the α-particle of the BiPo events are generated according to the energy distribution from a XENON100 BiPo data sample. In each event, the $S1_\beta$ and $S1_\alpha$ are checked for leakage into the energy region of interest for the MiDM analysis ($S1_\beta < 150\,\text{PE}$ and $S1_\alpha < 700\,\text{PE}$). Furthermore, the β has to fall into the NR band, which further suppresses the background by a factor of 0.27. In total 10^8 events have been simulated. The resulting number of background events is then normalized to the total number of expected BiPo events in run II. The resulting background expected from BiPo-decay is 0.166 ± 0.008 events and thus the total expected background is entirely dominated by this component.

4.4 Efficiency simulation

This section is based on the documentation of the efficiency simulation that has been developed for the MiDM analysis by M. v. Sivers (following a similar simulation by Itay

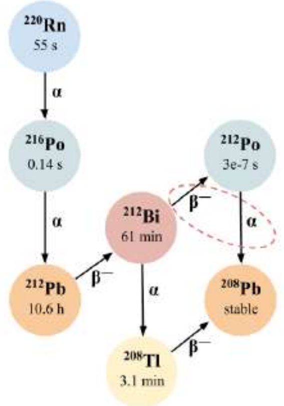

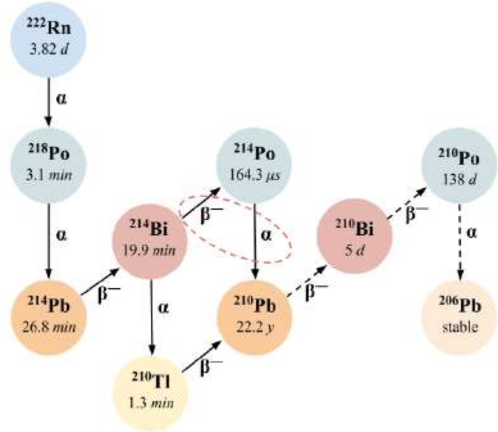

FIGURE 4.18: Decay scheme of ^{220}Rn (left) and ^{222}Rn (right). The potential background originates from the consecutive β-decay of ^{212}Bi (^{214}Bi) and α-decay of ^{212}Po (^{214}Po), marked by the red dashed circles.

Yavin used in [157]). The lifetime of the excited WIMP is given by $\tau = \pi/(\delta^3\mu_\chi^2) = \mathcal{O}(\mu\mathrm{s})$ and leads to a decay length in the order of a few meters. This simulation calculates the efficiency ϵ to detect the photon inside the 48 kg fiducial volume. The full path of the WIMP is simulated, including the locations of the NR interaction and the de-excitation. The finite acceptances of the minimum time difference of 3.5 μs between the S2 peaks and the decay time $50\,\mathrm{ns} < \Delta t < 2\,\mu\mathrm{s}$ condition are also taken into account. Since the mean free path of the photon is only ~ 2 mm at 100 keV and in the same region as the position resolution it is neglected and the position of the WIMP de-excitation is taken as the ER interaction point. The following steps are performed in the simulation:

1. Generate the initial velocity vector of the WIMP $\vec{v}_\chi$
2. Choose an interaction point for the scattering $\vec{x}_0$, assumed a uniform distribution inside the detector due to the small cross section.
3. Calculate the velocity vector after scattering $\vec{v}'_\chi$
4. Generate a random lifetime Δt of the excited WIMP from an exponential distribution with a decay time given by $\tau = \frac{\pi}{\delta^3\mu_\chi^2}$
5. Calculate the point of de-excitation $\vec{x}_1$.

The differential rate of WIMPs $\frac{d\sigma}{dE_\mathrm{R}}$ is given by equation (4.2) and the sample probability density function (PDF) can be expressed as

$$\mathrm{samplePDF}(E_\mathrm{nr}, v_\chi, \cos\Theta) = v_\chi f(\vec{v}_\chi)\frac{d\sigma}{dE_\mathrm{nr}}. \tag{4.6}$$

For a xenon target dipole-charge interactions (see section 4.2) contribute about 80 % of the total MiDM rate [151]. Thus, the cross section in the simulation is approximated by this contribution only, since it is technically much more straightforward to implement. The effect of this simplification has been studied by calculating the efficiency for the case of dipole-dipole interactions, using an approximation for the form factor F_{D} (see equation (4.4)). This study showed that taking into account the dipole-dipole contribution results in a small increase of the efficiency. In the relevant parameter space (where the analysis is most sensitive) the increase is at most 2 %. The dipole-charge cross section is given by

$$\frac{d\sigma_{DZ}}{dE_{\mathrm{nr}}} \propto \frac{1}{E_{\mathrm{nr}}}\left[1-\frac{E_{\mathrm{nr}}}{v_\chi^2}\left(\frac{1}{2m_N}+\frac{1}{m_\chi}\right)-\frac{\delta}{v_\chi^2}\left(\frac{1}{\overline{\mu}}+\frac{\delta}{2m_N E_{\mathrm{nr}}}\right)\right]F(E_{\mathrm{nr}})^2. \tag{4.7}$$

The Helm form factor $F(E_{\mathrm{nr}})$ can be parametrized in the following way

$$F(E_{\mathrm{nr}}) = 3\exp\left(-\frac{q^2s^2}{2}\right)\frac{\sin(qr)-qr\cdot\cos(qr)}{q^3r^3} \text{ with} \tag{4.8}$$

$$q=\sqrt{2m_N E_{\mathrm{nr}}}, \quad r=\sqrt{R^2-5s^2}$$
$$R=1.2A^{1/3}s, \quad s=\frac{1}{0.197\,\mathrm{GeV}}.$$

Finally, the velocity distribution $f(\vec{v}_\chi)$ in the reference frame of the earth can be expressed as

$$f(\vec{v}_\chi)d^3v_\chi \propto \exp\left(-\frac{v_\chi^2}{v_0^2}\right)\exp\left(-\frac{2v_\chi v_{obs}}{v_0^2}\cos\Theta\right)v_\chi^2 dv_\chi. \tag{4.9}$$

Using the sample PDF of equation (4.6) E_{nr}, $\cos\Theta$ and v_χ are drawn. The velocity vector is then given by

$$\vec{v_\chi} = v_\chi(\sin\Theta\cos\phi, \sin\Theta\sin\phi, \cos\Theta)$$

with the azimuth angle between WIMP and observer ϕ being drawn from a uniform distribution $[0, 2\pi]$. All kinematic constraints on E_{nr}, $\cos\Theta$ and v_χ are taken into account. The velocity of the outgoing WIMP is calculated in the center of mass (COM) frame where the magnitude is given by

$$v'_{\chi,COM} = f\frac{\overline{\mu}v_\chi}{m_\chi}. \tag{4.10}$$

$\overline{\mu}$ is the reduced mass of the WIMP-nucleus system and $f=\sqrt{1-\frac{2\delta}{\overline{\mu}v^2}}$. The azimuth angle after the scattering is again drawn from a uniform distribution $[0, 2\pi]$ while the polar angle is calculated by

$$\Theta_{COM} = \cos^{-1}\left(f^{-1}\left(\frac{m_N E_{\rm nr}}{\overline{\mu}^2 v^2} - 1 + \frac{\delta}{\overline{\mu} v^2}\right)\right). \tag{4.11}$$

Finally, by choosing the lifetime Δt from an exponential distribution with a decay time given by $\tau = \frac{\pi}{\delta^3 \mu_\chi^2}$, the interaction point of the de-excitation is calculated as

$$\vec{x}_1 = \vec{x}_0 + \vec{v}^{\,\prime}_\chi \cdot dt. \tag{4.12}$$

At this point, all relevant properties are simulated and the efficiency ϵ is calculated as the ratio $N_{\rm selection}/N_{\rm all}$, where $N_{\rm all}$ is the number of all events with the NR interaction inside the 48 kg fiducial volume. $N_{\rm selection}$ is the number of events fulfilling the following conditions:

1. The initial NR and the subsequent de-excitation are inside the 48 kg fiducial volume.
2. The first S2 comes after the second S1, otherwise the second S1 would be covered by the S2 peak (corresponding to sequences 1 and 2 introduced in section 4.3).
3. The time difference between the S2 peaks is larger than $> 3.5\,\mu$s.
4. The time difference between the S1 peaks is $50\,\mathrm{ns} < \Delta t < 2\,\mu$s.

The resulting efficiencies for the two benchmark cases motivated by the best-fits to DAMA/LIBRA are shown in figure 4.19. The main reason for the higher ϵ in the case of $m = 122.7\,\mathrm{GeV/c^2}$ is the shorter lifetime due to the higher mass splitting δ and the higher WIMP magnetic moment μ_χ.

After applying all cut acceptances introduced earlier as well as the efficiency from figure 4.19, 7 signal events are expected for benchmark case one and ~ 34 signal events for benchmark case two for the full XENON100 exposure of 10.8 tons $\times$ days.

4.5 Result and conclusions

After applying the data selection cuts described in section 4.3, no MiDM candidate event has been found in the XENON100 science run II dataset with a total exposure of 10.8 ton $\times$ days (see figure 4.14). We thus calculate an upper limit on the interaction strength using the maximum gap method [154]. Figure 4.20 shows the resulting limits for

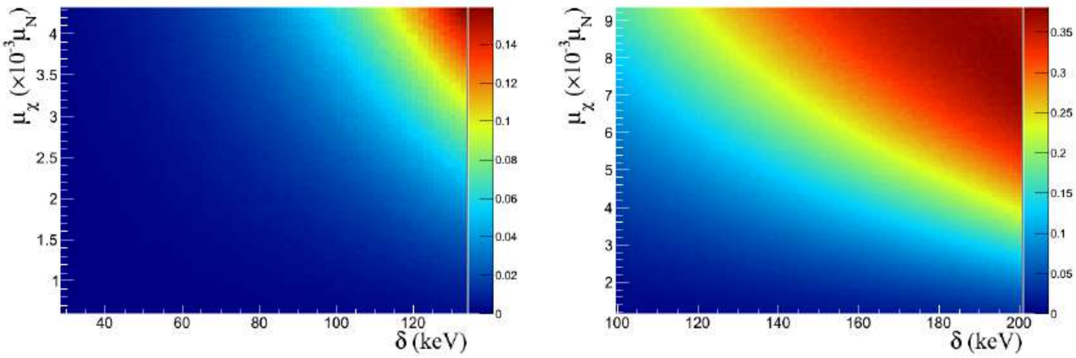

FIGURE 4.19: Efficiency (given by the color scale) for detecting both, the NR and the de-excitation ER signal, inside the 48 kg fiducial volume of XENON100 for a wide range of mass splittings δ and WIMP magnetic moments μ_χ (in units of the nuclear magneton μ_{nuc}). It is shown for the two benchmark cases, corresponding to WIMP masses of $m = 58.0\,\mathrm{GeV/c^2}$ (left) and $m = 122.7\,\mathrm{GeV/c^2}$ (right) [147]. For $m = 58.0\,\mathrm{GeV/c^2}$, the efficiency is significantly smaller, mainly due to the smaller δ and μ_χ which leads to a longer lifetime τ and thus to a longer mean path length until the WIMP de-excites.

the two masses, $m = 58.0\,\mathrm{GeV/c^2}$ (benchmark case 1) and $m = 122.7\,\mathrm{GeV/c^2}$ (benchmark case 2), together with the 68 % and 95 % confidence level regions for DAMA/LIBRA taken from [147]. The 68% DAMA/LIBRA contour is excluded for any of the two benchmark cases and the 95 % contour is completely ruled out in the second benchmark case. As this analysis relies on the detection of both interactions (NR and ER de-excitation), an approach which has not yet been pursued in a dark matter analysis so far, the sensitivity towards lower mass splittings is not competitive to previous results presented in [147] where only the NR interaction is taken into account. However, at higher δ and thus shorter lifetimes of the excited WIMP, a significant improvement of the limits on the MiDM interaction strength is achieved. While for $Q_{\mathrm{I}} = 0.09$ the DAMA/LIBRA best-fit region has already been ruled out in [147], our new analysis now also completely excludes the modulation signal being due to MiDM assuming the newer value of the quenching factor of $Q_{\mathrm{I}} = 0.04$ and covers previously unexplored parameter space above $\delta \approx 155\,\mathrm{keV}$.

The sensitivity of this type of analysis will be greatly improved for current ton-scale (e.g., XENON1T [54]) and future multi-ton dual-phase LXe TPCs (e.g., XENONnT [54], LZ [81] and DARWIN [84]). This is not only due to the increased target mass, but also thanks to the higher probability of detecting the de-excitation inside the larger active volume. Furthermore, XENON1T has a significantly reduced Rn background, which is the dominant contribution in this analysis. The specific MiDM signature of two S1 followed by two S2 signals differs significantly from the most common backgrounds and leads to a very low background expectation while exploiting a large fraction of the target mass.

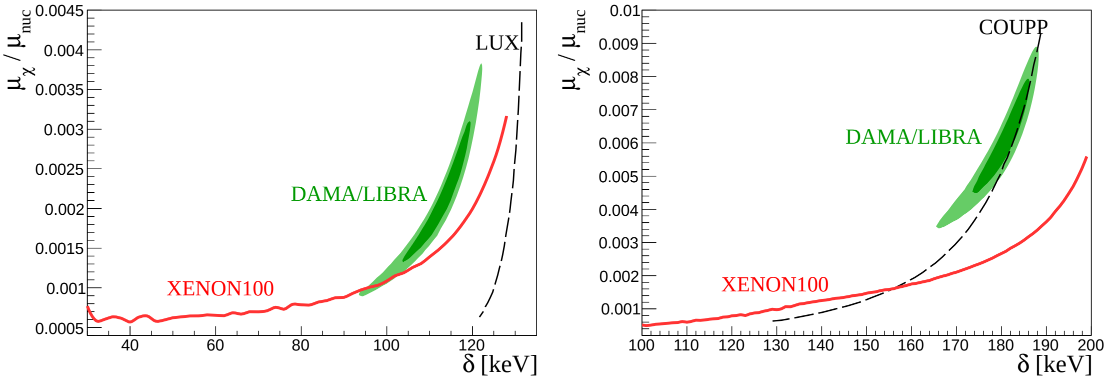

FIGURE 4.20: The exclusion limit (at 90% confidence level, CL) on MiDM interactions from run II of XENON100 is shown by the red curve for WIMP masses of $m = 58.0\,\mathrm{GeV/c^2}$ (left) and $m = 122.7\,\mathrm{GeV/c^2}$ (right). Also shown are the 68% (dark green) and 95% (light green) CL regions of the best fit to the DAMA/LIBRA modulation signal [147]. Limits calculated in [147] using results from LUX and COUPP are shown for comparison (dashed lines). For a WIMP mass of $m = 122.7\,\mathrm{GeV/c^2}$ (right), the XENON100 result based on the search for two subsequent signals is superior to the previous result above $\delta \approx 155\,\mathrm{keV}$ and rules out the entire best-fit region.

Chapter 5

Vetoes for the XENON1T data acquisition system

Considering the null result from [75] as well as from other experiments [53, 80] it becomes clear that the sensitivity of dark matter detectors have to be increased in order to open up the chance of a dark matter detection. As part of the XENON program the first ton-scale direct dark matter detector, XENON1T, has been built, and is currently running at LNGS in Italy. The goal of this detector is to improve the sensitivity to spin-independent WIMP interactions by two orders of magnitude with respect to XENON100 [54]. The main improvements of XENON1T are its larger target mass and lower background rate. Furthermore, the data acquisition system (DAQ), comprising the digitization, event triggering and processing of the data, has been improved. This new system allows to calibrate at higher rates, to lower the digitization threshold as much as possible and provides a more flexible event trigger. In section 5.1 the new XENON1T DAQ is introduced. In section 5.2, 5.3 and 5.4 the design and realization of a high energy veto system as well as a busy-veto are described.

5.1 Data acquisition in XENON1T

For XENON1T the DAQ has been newly designed compared to XENON100 to meet the needs for the new experiment. One of the main design goals was to lower the trigger threshold as far as possible in order to increase sensitivity to low energy interactions. This is important because the expected WIMP energy spectrum decreases exponentially (see figure 1.5). The event trigger of XENON1T is preformed by a software algorithm on a PC after the full waveform of all 248 PMTs (plus 6 diagnostic PMTs) has been read out from the digitizers. In order to enable this, a high data throughput ($\sim 300\,\mathrm{MB/s}$)

Figure 5.1: XENON1T data acquisition system. The first rack from the left contains the PCs and the two following racks contain the hardware to readout the signals from the TPC (i.e.,amplifiers and digitizers). In the background the data acquisition system of the muon veto can be seen.

for the digitizer read out is required, in particular when calibrating the detector at high rates. The full waveform is needed for possible reviews of events leaking into the region of interest. Finally, in view of XENONnT the DAQ should be scalable to the future upgrade without major modifications. The DAQ includes a busy-veto, which ensures that new data is only "accepted" if all digitizers are able to record it, and a high energy veto (HEV), which can be used in calibration data in order to reject high energy events before they are read out. In the following the XENON1T DAQ is introduced and it is shown how the above requirements are addressed as well as where the veto system (consisting of the busy-veto and the HEV) fits into this picture.

The DAQ is controlled via a web application that allows users to start/stop runs in various operation modes. Furthermore, there are several monitoring features on the web interface, such as detailed information about the status of the DAQ, an online oscilloscope and diagnostic information on the trigger data. These features provide immediate feedback on the acquired data. The paradigm of the DAQ is to have a continuous, trigger-less readout of all channels at a threshold of $\sim 0.3\,\mathrm{PE/channel}$. This is realized by a parallel readout of the digitizer by several PCs controlled by one reader software. The read-out data is stored into a data base and triggered by a software trigger on a computer farm, which searches the data base for physical events. Only the raw data of events triggered by this software is permanently stored while the rest of the data is discarded. A picture of the new XENON1T DAQ system is shown in figure 5.1.

The data flow in the XENON1T DAQ is illustrated in figure 5.2, starting from the PMTs inside the TPC. The PMT signals are amplified by a factor of ten using Phillips 776 NIM amplifiers. These amplifiers have two outputs per input, one of which is used for

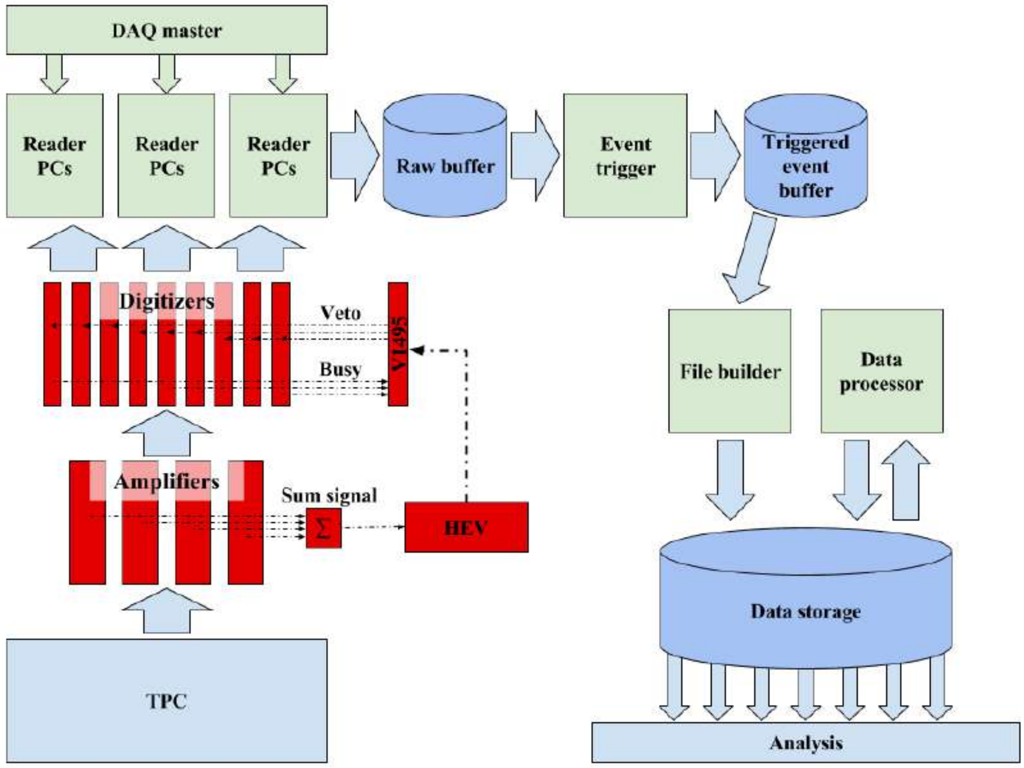

FIGURE 5.2: Simplified illustration of the data flow in XENON1T. Steps involving hardware other than computers are shown in red and subsequent software processes are shown in green. The high energy veto (HEV), which is used in calibration runs to reject high energetic events, is connected in parallel to the main readout chain in order to inhibit the read out of high energy events online on the digitizer boards.

the high energy veto described in the following sections. The other output is used to digitize the amplified signals by CAEN VME V1724 Flash ADCs with a sampling rate of 10 ns, a 14 bit resolution, a dynamic range of 2.25 V and an input filter of 40 MHz.

The digitizers are working with a new firmware, custom developed for XENON1T by CAEN and the Bern group. This firmware allows to read out the detector in two different modes. In the first mode, all channels are triggered simultaneously by an external trigger. This feature is used in order to perform PMT gain calibrations using LED pulses, since it is known when the LED pulse is generated. The second mode, the self trigger mode, allows to trigger each channel individually using an independent threshold for every PMT. This mode is used for dark matter and calibration data taking in order to read out the relevant signals of all channels. Furthermore, using this mode it is possible to lower the threshold as much as possible depending on the noise level of each channel. These individual thresholds are called self-trigger thresholds. After being read out, the data is stored in a raw buffer based on the open source data base MongoDB [158]. The data in the raw buffer consists of time snippets from all individual channels enclosing an excursion above their self-trigger threshold. The actual triggering and subsequent

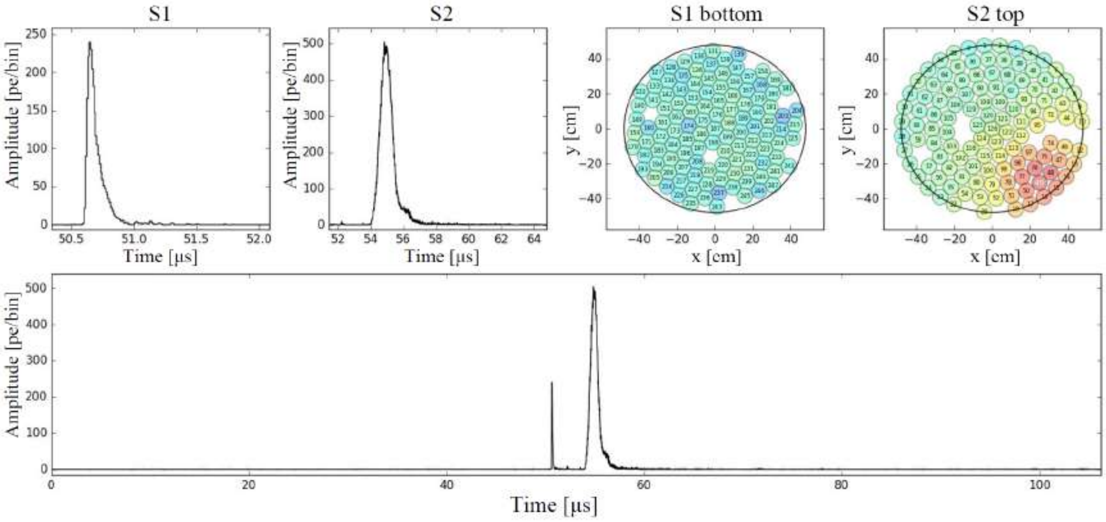

FIGURE 5.3: First event from XENON1T with field, showing an S1 and S2 pair. This event has been recorded and triggered by the new XENON1T DAQ system and processed by the new data processor pax. In the bottom panel the sum waveform of all PMTs are shown while the two top-left panels show a zoom-in on the S1 and S2 peak. In the two top-right panels the S1 hitpattern of the bottom PMTs and the S2 hitpattern of the top PMTs are shown. The color scale indicates the amount of light seen by the individual PMTs where red indicates a large signal.

definition of physical events is done on software level, by scanning the raw buffer for clusters of individual PMT signals occurring at the same time. The raw data of the triggered events is then permanently stored to disk from which it is read and processed by the new XENON1T data processor, pax [129].

In order to lower the data rate during calibration runs a HEV has been designed, which is incorporated in parallel to the main readout chain between the amplifiers and the digitizers (see figure 5.2). The HEV allows to reject high energy events before they are read out and stored to the raw buffer and thus it reduces the data load on the DAQ. Furthermore, using the HEV results in a higher fraction of relevant low energy data compared to the total amount of data since only high energy events are discarded while low energy events are being recorded as usual. During dark matter data taking the HEV is switched off and all events are stored to disk in order to not loose any information. In section 5.2 and 5.3 the HEV is discussed in detail.

An important aspect to manage high rates in calibration mode is the parallelization of the digitizer readout, which is realized by the custom-developed ADC readout software kodiaq [159]. The "DAQ master" of this software controls eight ADC readout PCs (slaves) that are simultaneously reading the 262 channels from the 33 V1724 digitizer boards. It furthermore ensures that the ADC boards are strictly time-synchronized, which is required for a parallel readout. With this configuration the design read-out speed of above 300 MB/s can be achieved. For XENONnT the DAQ will be adopted

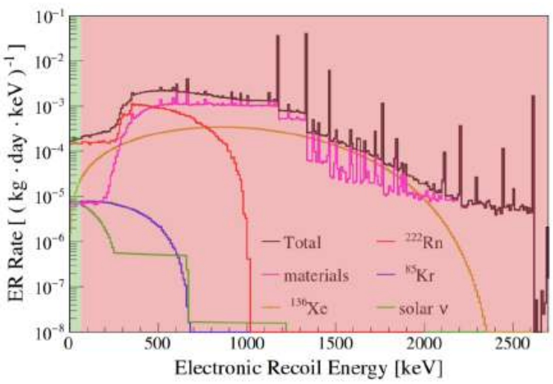

Figure 5.4: Simulated energy spectrum of the total ER background rate of XENON1T in a 1 t fiducial volume (black) and the individual components (colored lines). Due to the WIMPs exponentially falling energy spectrum the region of interest is located at very low energies, indicated by the green area, while all the "high energy" part (red area) is of limited interest. Hence, while calibrating the detector a high energy veto can be used in order to reduce the load on the DAQ and allow higher calibration rates. Figure modified from [54].

by further parallelization of the read-out. Since the digitizers are readout in parallel and independently of each other, it is important to ensure that the complete data from all ADCs is available. At high rates it may occur that the internal buffer of a digitizer gets full and thus it is not able to accept any more data. In such cases the busy-veto guarantees that all digitizers stop data taking since this data would be incomplete. The busy-veto is described in more detail in section 5.4. The first XENON1T event with drift field, containing an S1 and S2 pair is shown is shown in figure 5.3. This event has been recorded on the 18th of May 2016 by the new DAQ system introduced in this section.

5.2 High energy veto design studies

Since the WIMP search region is located at low energies (below $15\,\mathrm{keV_{ee}}$) this is the most crucial energy region to be calibrated. Calibration events at higher energies are of rather limited use. This is illustrated in figure 5.4, which shows the simulated background spectrum of XENON1T [54] where the vast majority of events are outside the region of interest marked in green. As a high data throughput is one of the prerequisites of the DAQ, and since a large fraction of the data is due to high energy S2 peaks and their photo-ionization tails, it is beneficial to inhibit those peaks before they are read out from the digitizers. Due to drift times up to $\sim 650\,\mu$s in XENON1T a HEV based on the S1 peak, as realized in XENON100, would yield in a much higher dead time compared to a veto based on S2 peaks (see discussion below). Thus, in order to maximize the data throughput and to minimize the dead time the approach based on S2 peaks has been chosen.

The HEV is based on the attenuated analog sum of the bottom PMTs. This sum signal is processed by an ADC equipped with a Field Programmable Gate array (FPGA) (see section 5.3.2) which makes the decision if an event should be vetoed or not and transmits the veto signal to the digitizers. Since the veto signal from the HEV has to reach the digitizers before they start to read out the relevant peak, the read out decission is delayed in the digitizers by several μs within a ring buffer. The firmware of the HEV also provides the possibility to veto events based on their radial position. Especially in case of calibration campaigns with external sources this feature reduces the number of events from interactions near the edge of the detector while recording all events closer to the center of the detector, which is the most crucial part. The functionality of the HEV board and the development of its FPGA firmware will be discussed in more detail in sections 5.3.

Several aspects have been considered in the realization of the veto, such as what signal the veto should be based on, how long the veto should be activate, and if a veto depending on the radial position is possible. These studies are based on XENON100 data as they were done before XENON1T was constructed. Nevertheless, the conclusions can be applied to XENON1T since the expected behaviour of the studied parameters in XENON1T is essentially the same as in XENON100. In the following these analyses and their implications on the veto design are discussed.

High energy veto based on S1 vs. S2

In XENON100 the HEV is based on S1 peaks whose amplitudes exceed a certain threshold [77]. The drawback of this method is that after each high energy S1 the full drift time plus the length of the S2 plus its after-pulse tail has to be vetoed since the depth of the interaction is not known at this point. For XENON1T this aspect becomes relevant because the drift time is considerably longer and the activity of external calibration sources needs to be much stronger in order to get reasonable statistics in the center of the detector. Furthermore, vetoing only the S2 peak allows in principle to calibrate in pile up mode. Thus, the HEV is based on the S2 peak, which makes it unnecessary to veto the entire drift time between S1 and S2 peaks.

The effect of vetoing HE-events based on their S1 vs. S2 has been studied using a simulation. In this simulation events are generated with different time differences (i.e., different calibration rates) following the NR energy spectrum from AmBe calibration data of XENON100. The drift time of the simulated events is distributed uniformly between $(0-500)\,\mu$s, representing the assumed maximum drift in XENON1T. Next, the HEV is determined once based on the S1 and once on the S2 peaks. The threshold is chosen to be S1 $>$ 300 PE and S2 $>$ 100000 PE which roughly corresponds to the same energy in XENON100. In the case of the S1-veto the veto length is set to 1 ms in order to cover the full drift length plus an S2 tail of 500 μs. For the S2-veto the veto length

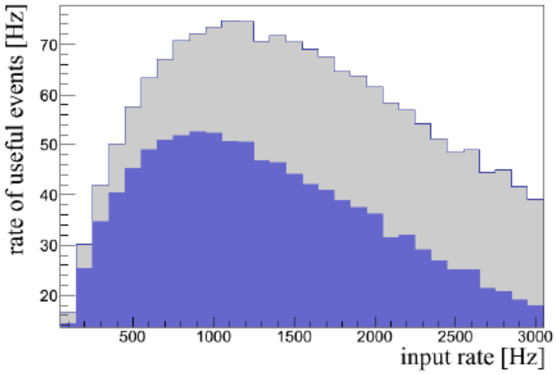

FIGURE 5.5: Simulated rate of useful events (no pileup and not affected by HEV from other events) depending on the input event rate for a HEV based on the S1 (blue) and S2 (gray). The veto length is kept constant at a value of 1000 μs (S1-veto) and 500 μs (S2-veto) motivated by the maximum drift time in XENON1T of $\sim 500\,\mu$s.

is set to $500\,\mu$s as it only has to cover the S2 tail. The resulting events are labeled as good if:

1. It is not a high energy event.
2. There is no time overlap with other events.
3. The S1 and S2 peaks do not fall inside the veto of another event (i.e., the information of all peaks are available).

In figure 5.5 the rate of good events depending on the total event rate is shown for both veto options. The rate of good events increases following the increasing total event rate until it reaches a maximum due to pile up and the overlap of vetoes initiated by other HE-events. As expected, the S2-veto yields a higher rate (about $2\times$ larger) of useful events at a given input rate compared to the S1-veto. Thus, for XENON1T it is beneficial to design a HEV based on the S2 peak, which becomes possible due to the new CAEN digitizer firmware that allows the readout to be delayed for up to $10\,\mu$s. For the current configuration of XENON1T this effect might be even more prominent, as the maximum drift time is around $\sim 650\mu$s.

Veto length

A significant amount of the digitized data volume comes from the photo-ionization tails following the S2 peaks, which is why it is important to veto these tails as well. This tail contains almost no useful information (except for some dedicated analyzes such as the study of single electron charge signals in [160]). It is expected that the length of the tail depends on the energy of the preceding S2 peak, since higher energy means that more light is available to potentially ionize metal surfaces and impurities. In figure 5.6 the correlation between the S2 energy and the length of its tail is shown using data from XENON100. The y-axis represents the amount of "activity" in the waveform after a

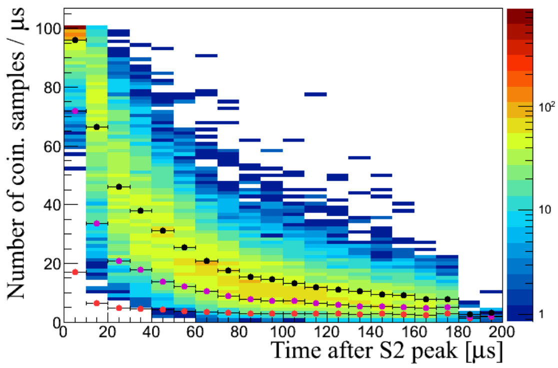

FIGURE 5.6: Decay of tails after S2 peaks with an S2 energy of (20000-40000) PE (red), (60000-80000) PE (magenta) and (100000-120000) PE (black). The colored histogram is the distribution from which the black profile is drawn. The y-axis represents the "activity" in the waveform after a certain amount of time described in more detail in the text. For higher energies a larger activity can be observed. The drop at 180 μs is due to the maximum drift length.

certain amount of time. This activity is quantified by the number of samples per μs with a coincidence level of at least two PMTs. In order to be in coincidence, two PMTs need to have an excursion above 30 ADC counts from baseline within a time window of four samples ($\triangleq$ 40 ns). The maximum of this parameter is 100 samples/μs as at this value all PMTs are in coincidence. The drop after $\sim$ 180 μs is due to the maximum drift length of XENON100, when all ionization electrons that constitute the S2 tail have reached the top of the TPC and a drop of the activity inside the TPC is expected. Figure 5.6 shows that in order to minimize the dead time due to the HEV a veto-length depending on the S2 energy is beneficial. However, there needs to be a new study based on XENON1T data, since the S2 tails might behave differently due to the lack of metal surfaces inside the TPC and the different level of purity.

Study on position depended veto

Due to the self shielding of xenon, external calibration sources will introduce many more events at the edge of the detector than in its center. Thus, in order to obtain reasonable statistics in the fiducial target the number of events acquired at large radii will be much higher than needed. To reduce the amount of data, and to enlarge the data throughput, S2 peaks located in the outer layer of the detector could be vetoed before being read out just like high energy S2s. However, as shown in figure 5.7, a radial veto can lead to a potentially dangerous event topology originating from double scatter events with only one S2 being vetoed and thus imitating a single scatter event (one S1 and one S2) resulting in a wrong S2/S1 ratio. This problem can be solved by keeping the binary information that a veto was issued in the data stream and rejecting events that contain a veto in the analysis. A veto on the radial position can be realized by summing up two groups of PMTs from the top PMT array, the outer most PMT ring and a second group located closer to the center. This has been tested on processed data from XENON100 where the top PMT array is split into two groups (outer ring and center PMTs) and the fraction of the signal seen by the outer ring divided by the center PMTs is compared to the reconstructed radius of the events. In figure 5.8 the resulting distribution is shown for a selection of single scatter events. A clear correlation between the outer and the inner signal of the S2 peak and the radius can be seen, which allows the definition of a radial cut based on this ratio. In summary, an online radial-veto based on such a parameter is possible if the information about an occurring veto is kept for the analysis.

5.3 Realization of the high energy veto

The HEV of XENON1T reduces data-volume by vetoing tails from S2 peaks. It also has to veto the S2 peak itself, since it contributes significantly to the total amount of digitized data. In order to do this the veto decision needs to be made before the data is actually read out by the reader PCs (see illustration in figure 5.2). The firmware of the CAEN V1724 digitizers, used for the XENON1T DAQ, was designed to put the digitized data into a ring buffer which is read out after a delay of up to 10 μs. The veto decision has to be made within this time period, which is one of the main reasons why the HEV logic is implemented on an FPGA since they are very fast. Another big advantage of an FPGA is that their firmware can be simply reprogrammed and readjusted as new needs arise during detector operation. Furthermore, using an FPGA with a custom developed firmware allows to implement all the specific features, such as an energy dependent veto length, online pulse shape discrimination and the possibility to veto events close to the detector's surface. The working principle of an FPGA is introduced in section 5.3.2.

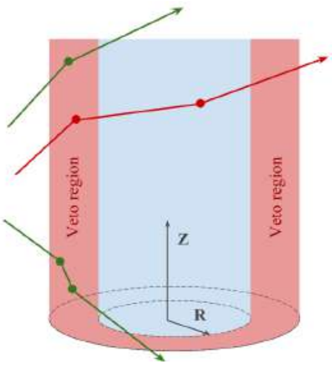

FIGURE 5.7: Illustration of possible event topologies resulting from a veto based on the radial position of S2 peaks. A potentially dangerous topology is generated if only one S2 of a double scatter is being vetoed and thus looks like a single scatter containing one S1 and one S2. A solution for this problem is to keep the information that there was a veto in the data stream and reject such events later in the analysis.

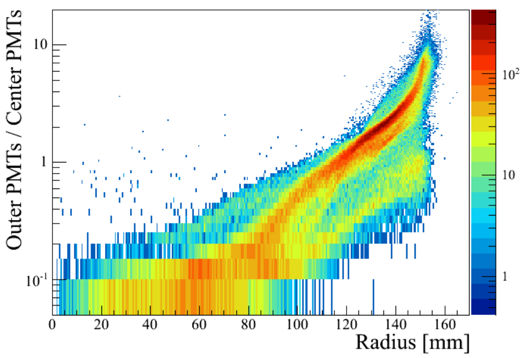

FIGURE 5.8: Distribution of single scatter events from XENON100 showing the S2 signal seen by the outer ring of the top PMT array divided by the center PMTs vs. reconstructed radius. The correlation between these two parameters allows the definition of a radial cut.

Similarly to XENON100, the input signal for the HEV of XENON1T is the sum of all bottom PMTs. The bottom PMTs are used because their response to S2 peaks is more uniform and the measured sum signal is less affected by non-working PMTs and small deformations of the gate and the anode, which leads to (x-y) position dependent differences in the S2 amplification.

5.3.1 Attenuated sum signal of bottom PMTs

The sum signal of the bottom PMT array is realized by using one of the two outputs from the Phillips 776 amplifiers and summing them up in three stages of Phillips 740 linear fans:

1. **First stage:** 121 inputs from the bottom array are summed up in groups of four on 8 Phillips 740 modules resulting in 31 output channels.
2. **Second stage:** 31 inputs (outputs from first stage) are summed up in groups of four on two Phillips 740 modules resulting in 8 output channels. The input of theses two modules are attenuated by a factor of 31.25 (described below).
3. **Third stage:** The remaining 8 input channels (outputs from second stage) are summed up on one Phillips 740 module to the final sum signal used for the HEV.

The NIM modules have a range up to only 2.5 V and the dynamic range of the digitizer on the HEV board is 2 V. Therefore, the sum signal needs to be attenuated. In order to get a first idea of the required attenuation factor, the height of S2 peaks is analyzed using data from XENON100. At $\sim 1000\,\mathrm{keV}$ the height of the bottom PMTs is below $\sim 100\,\mathrm{V}$ as shown in figure 5.9. Assuming similar S2 signals in XENON1T in terms of height (due to the same S2 generation condition), the attenuation factor should be $A \approx \frac{80\ V}{2.5\ V} = 32 \approx 30\,\mathrm{dB}$ in order not to saturate the NIM modules up to 1000 keV. Based on this rough estimation Π-pad attenuators, as shown in figure 5.10, have been added to the inputs of the second stage of the Phillips 740 linear fans. This attenuator can be described by the two equations $R_1 = \frac{A^2-1}{2A}$ and $R_2 = \frac{A+1}{A-1}$, with $R_1 = 820\,\Omega$ and $R_2 = 56\,\Omega$. Solving these equations results in a theoretical attenuation factor of $A = 31.25$. The attenuator has been tested by recording the same signal, once routed through a normal and once through an attenuated channel. The resulting spectra of the signal height are fitted by a Gaussian function and by comparing the mean of this Gaussians an attenuation factor of $A = 30.8$ is measured, which is close to the theoretical one.

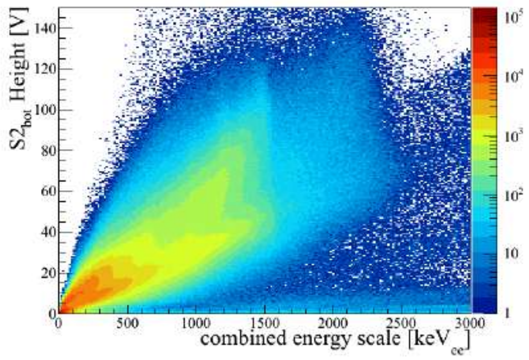

FIGURE 5.9: S2-height of bottom array signals as a function of their energy (data from XENON100). In order to not exceed a height of 2.5 V up to 1000 keV, and assuming similar signals in XENON1T, an attenuation of $A \approx \frac{80\ V}{2.5\ V} = 32$ needs to be achieved.

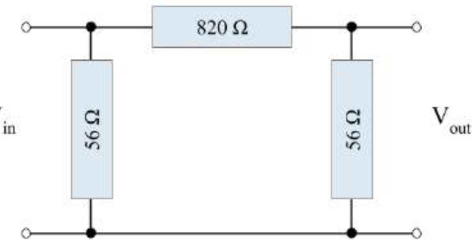

FIGURE 5.10: $\Pi-$pad attenuator with a nominal attenuation factor of $A = 31.25$ designed for XENON1T. The sum signal of the bottom PMT array is attenuated by means of this attenuator.

5.3.2 Operation principle of an FPGA

The HEV is realized on a Field Programmable Gate Array (FPGA), due to their features of being fast and flexible. The working principle of an FPGA is introduced in this section and the specific hardware used for the HEV is introduced in the next section. An FPGA mainly consists of three types of elements: arrays of basic logic blocks, I/O pads in order to communicate with the "outer world" and programmable interconnections between the different blocks as illustrated in figure 5.11. Programming the FPGA chip means telling it what the logic blocks should do and how they should be connected with each other. These "rules" for the logic blocks and connections are implemented in a firmware, which can be installed on the FPGA chip. The possible complexity of the firmware for a certain chip is usually defined by the number of logic blocks and I/O ports. Depending on the FPGA chip they may also contain some more sophisticated elements, such as block memory units (BRAM) or other hard wired functions. Such functions have an increased speed compared to building them out of basic elements.

FPGAs are programmed using a Hardware Description Language (HDL), such as Verilog or VHDL, which is used for the XENON1T HEV. In order to compile these languages and configure the chips, a development environment from the FPGA manufacturer is needed. For the firmware discussed here, this environment is called ISE from Xilinx since a Spartan-6 FPGA from this manufacturer is used in the veto module introduced in section 5.3.3.

In figure 5.12 a very basic scheme of a programmable logic block is shown. It consists of three different elements, a programmable look up table (LUT), a register that can be used as flip-flop or as latch and a multiplexer. The LUT can be configured in order to

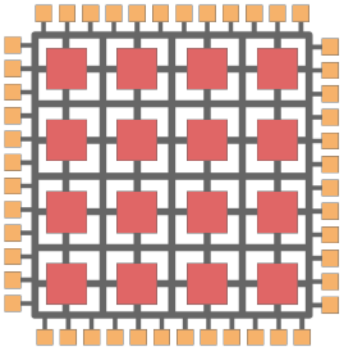

FIGURE 5.11: Simplified view of an FPGA consisting of logic blocks (red squares), also shown in figure 5.12, interconnecting lines (gray) and the IO ports ensuring the communication with the outside world (orange). The possibilities of an FPGA are mainly defined by the number of logic blocks and IO ports.

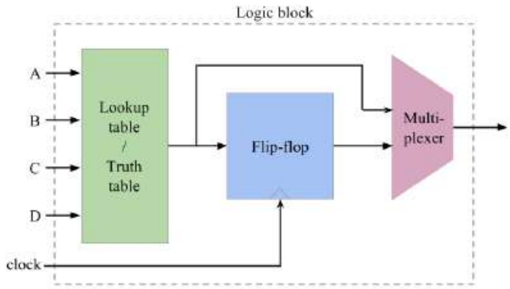

FIGURE 5.12: Simplified scheme of a logic block element from an FPGA. The four inputs are connected to a programmable logic lookup table. The output of this table can either be routed directly to the output of the logic block or through the flip-flop.

implement any desired logic, such as $(A \wedge B) \vee (C \wedge D)$, that combines the four inputs $A - D$. The output of the LUT is routed to the flip-flop as well as to the multiplexer. Finally, the multiplexer defines if the output of the LUT or the one of the flip-flop is sent to the output of the logic block. This is a rudimentary example of a logic block which can be much more sophisticated in today's FPGAs. In a more general way one can think of the FPGA as kind of a "rack" in which different modules, such as counters, logic modules, etc. can be inserted. In VHDL these modules are called components and can be implemented independently of each other. Analogous to hardware modules, these components have inputs and outputs that can be connected to each other. The transition of the signals is not continuous but is a step by step movement synchronized by a common clock sent to the flip-flop.

5.3.3 The DDC-10 board and its firmware

The hardware used for the HEV is the DDC-10 board from SkuTek[1]. It consists of a 14 bit analog to digital converter (ADC) with 10 input channels, an FPGA chip (Spartan-6 LX 150) and an on-board processor (Blackfin 561) running embedded Linux, all hosted on the BlackVME S6 motherboard. There are four NIM inputs, four programmable NIM outputs and several interfaces such as VME, USB-2, RS-232 and gigabit Ethernet. A picture of the board and a simplified block diagram of its components can be seen in figures 5.13 and 5.14. The DDC-10 can be used as a standalone component and comes with an FPGA firmware and a web interface, which runs on the Blackfin and can be accessed via any web browser. Therefore, the DDC-10 module is ready to use for many

[1]http://www.skutek.com

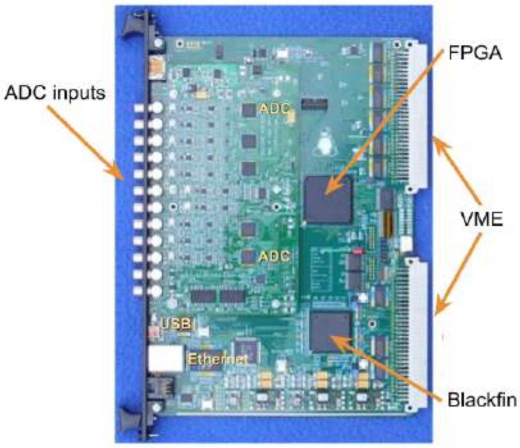

FIGURE 5.13: Figure of the SkuTek DDC-10 board with its individual components.

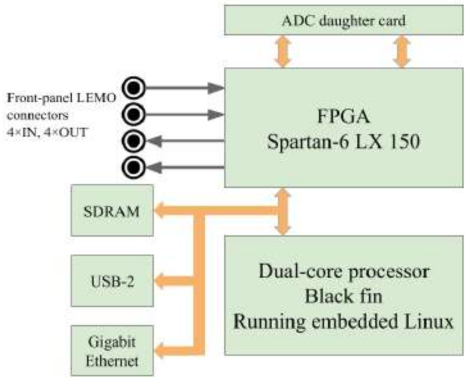

FIGURE 5.14: Simplified block diagram of the DDC-10 architecture. The central components are the microprocessor Blackfin, running embedded Linux, the Spartan-6 FPGA from Xilinx and the daughter card hosting a 10 channel 14 bit ADC connected to the FPGA chip.

applications as it is delivered. However, the real advantage of the DDC-10 board is the possibility to implement a custom firmware, which provides many more possibilities and is necessary in order to meet all requirements of the HEV.

As the HEV should only trigger on high energy S2 peaks a rough energy estimation and peak classification on the DDC-10's FPGA is needed. In order to meet this requirement, three peak parameters are extracted by the firmware developed within this thesis: the rise time, the pulse width at half maximum and the integral of the peak. Each of these parameters is calculated in standalone components that run in parallel in order to minimize the processing time. Furthermore, there is a component which collects all the information and decides whether a veto has to be issued or not, based on the settings defined in the configuration file of the DAQ. Ideally the veto trigger always happens at the same time with respect to the beginning of the peak, thus a so called "veto delay" is implemented. This delay has to be roughly the same (or less) as the delay of the ring buffer in the CAEN V1724 digitizers in order to prevent the DAQ of recording the full S2 peak. In addition, the delay should be longer than the time needed to derive the peak parameters as they are used in order to make the veto decision. As shown in figure 5.15 the start time of a peak is defined as the time where the sum-signal exceeds the threshold defined in the settings. Furthermore, the scheme indicates at what time the different peak parameters are available in order to make the veto decision.

A block diagram of the firmware with its connections to the outside world is shown in figure 5.16. The HEV is used as a standalone board, which means that it runs independently from the rest of the DAQ after it has been initialized at the beginning of each run. There are many parameters implemented in the different components that can be set without updating the firmware. These parameters are included in the configuration file of the DAQ software kodiaq and are sent to the Blackfin micro processor by the DAQ master over an SSH connection before the actual data taking starts. This allows to set different parameters for different purposes. The Blackfin itself has access to the control register and block RAM (BRAM) of the FPGA where the settings are stored. The control register and the BRAM are both elements of the FPGA that allow storage of some data. However, the way they can be accessed to read and write data is different. The control register of the firmware has only 16 bits and can be accessed as read/write from both the Blackfin and the FPGA sides. In contrast to the BRAM, the

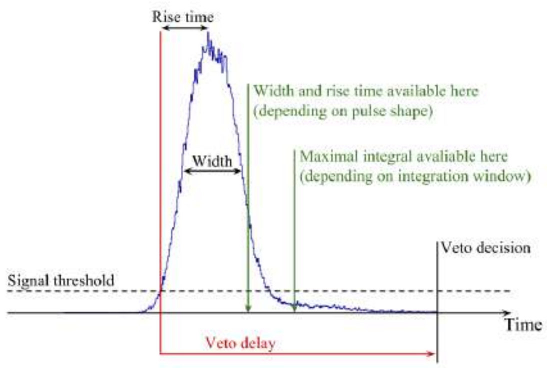

Figure 5.15: Illustration of different peak parameters implemented in the HEV and when they become available in order to make the veto decision. A veto delay can be set in order to ensure that all information is available for the veto decision. The raw data is delayed on the CAEN V1724 ADCs until the veto decision is available.

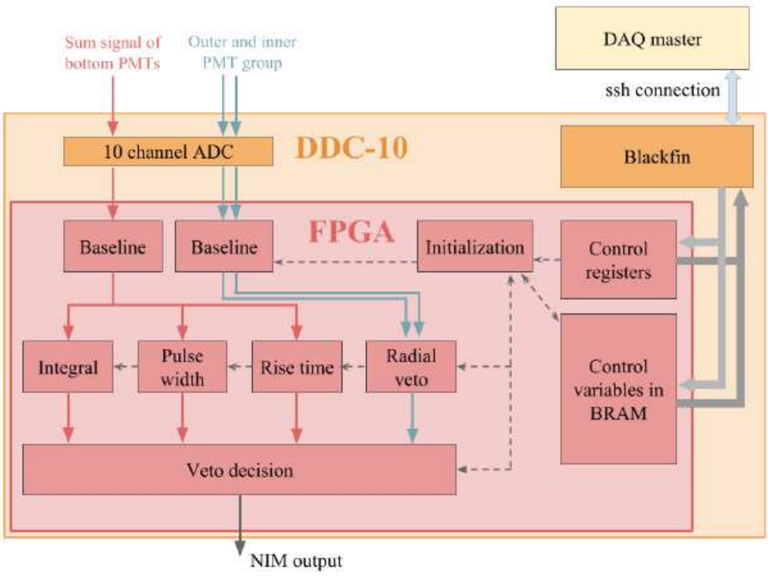

Figure 5.16: Block diagram of the HEV firmware. The FPGA and components of the firmware are shown in red, elements embedded into the whole DDC-10 board are represented in orange. The veto decision is based on the peak information collected by the individual firmware components (integral, pulse width, rise time, radial veto). A detailed description of each component can be found in the text. The input signal is the sum of all bottom PMTs (red arrows) and two summed PMT groups of the top PMT array in the case of the radial veto component (dark cyan arrows). The communication between the micro processor Blackfin and the DAQ master takes place over SSH.

Parameter	Description
Signal polarity	Defines whether the input signal is positive (0) or negative (1).
Integration window	The time window for the integration in units of [10 ns].
Veto delay	The time that will elapse after a peak started until the veto starts [10 ns]. It has to be at least 50 ns larger than 'integration window'. See figure 5.15.
Signal threshold	A peak starts as soon as the signal exceeds the signal threshold [ADC counts].
Integral threshold	The threshold for the HE events. All events with an integral above this value will be vetoed. [ADC counts]
Width cut	Cut for the discrimination between S1 and S2 based on the peak width. If the peak width is smaller than the width cut value the peak is classified as S1 peak. [10 ns]
Risetime cut	Cut for the discrimination between S1 and S2 based on the rise time. If the rise time is smaller than the rise time cut value the peak is classified as S1 peak. [10 ns]
Component status	With this parameter it is possible to turn the different components on(='1') or off(='0'). Integer values from 0-7 are allowed. The firmware will read it as binary number where bit1 = risetime, bit2 = width, bit3 = integral, bit4 = ring veto
p_0–p_2	Three parameters for the polynomial function which defines the veto length based on the S2 energy (see equation (5.2)).
$K_{\text{outer ring}}$	Factor used for the radial position veto multiplied with the signal of the outer PMT group (see equation (5.1)).
$K_{\text{inner ring}}$	Factor used for the radial position veto multiplied to the signal of the inner PMT group (see equation (5.1)).
Pre-scaling	Pre-scaling factor. Every "x"th event that would be vetoed passes the veto.

Table 5.1: Table of all parameters of the HEV that can be set in the configuration file of the DAQ system without updating the firmware. Every time a new run is started these settings are passed over to the DDC-10 board.

FPGA has access to all registers simultaneously and a change of their values is recognized at any time. Thus, it can be used to initiate the firmware to start a process (e.g., to read the BRAM). The BRAM, on the other hand, has much more memory compared to the control register but to access the content of the BRAM the firmware needs to read the every bit one at a time. Thus, the content of the memory can be changed without being immediately noticed by the FPGA. The HEV firmware is designed such that the Blackfin writes all the settings to the BRAM and then triggers one bit of the control register in order to tell the FPGA to read the new settings from the BRAM. In table 5.1 a summary of all available settings is shown. The individual components of the firmware and the parameters of the table are described in more detail in the following.

Initialization component

All parameters from table 5.1 can be set in the configuration file of the DAQ system. In order to do this, kodiaq opens an SSH connection to the onboard processor (Blackfin) of the DDC-10 board and transmits the parameters. Blackfin then writes them to the BRAM and triggers one bit of the control register in order to tell the firmware to read the memory. The BRAM is then accessed by the "initialization component" and the parameters of the firmware are set correspondingly.

Baseline component

The baseline component has two purposes. First, it calculates the baseline and second it continuously subtracts the baseline from the incoming ADC signal such that the subsequent components always receive the baseline corrected signal. The baseline is determined every time the HEV is initialized by the DAQ master (i.e., every time a new DAQ run is started). It is calculated by adding up the raw ADC signal of 64 samples (640 ns) and dividing the result by 64. The summation time is hard coded and therefore can only be changed in the firmware code, which requires recompilation of the code and an update of the FPGA. The summation must be a multiple of two since a division by a power of two is relatively easy to realize on an FPGA compared to division by an arbitrary number. In order to avoid distortion of the baseline due to a peak, that might appear during the baseline calculation, the current signal is always compared to the one 30 ns before. If the difference of these two signals is larger than 100 ADC counts (12.2 mV) the baseline calculation routine starts over again. The baseline component also checks if positive or negative signals are expected depending on the setting of the 'signal polarity' parameter and inverts the signal if the parameter is set to positive signals. The output of this component is the baseline corrected ADC signal, which is always negative.

Integration component

This component continuously sums the ADC samples within a given floating time window defined by the parameter 'Integration window' and forwards the result to its output. This is achieved by adding the new sample at every time step while subtracting the oldest one.

Width component

Since S2 peaks are much broader than S1 peaks, the width is a powerful discrimination parameter. The width component calculates the peak width at half maximum in the following way: As soon as the signal exceeds the signal threshold all subsequent ADC sample are stored. The time step at which the signal drops again below half of the peaks maximum is taken as 'right edge' of the width. At that time it is assumed that the peak maximum has been found and the width component searches the buffered ADC samples and looks for the one that exceeds half of the peak maximum for the first time. This time is taken as the 'left edge' of the width. The width output is defined by the difference of the two edges.

Rise time component

S2 peaks have a larger rise times ($\mathcal{O}(100)$ ns) than to S1 peaks ($\mathcal{O}(10)$ ns). Therefore, the rise time of a peak is also a good discrimination parameter between S1 and S2 signals. The rise time represents the time from the starting point of the peak (first sample which is above the signal threshold) to the peak maximum. In order to be sure that the peak maximum has been found the rise time is only available for the veto decision component once the width of the peak has been found, which means that the signal has already dropped to 50 % of the peak maximum.

Radial veto

For calibration runs with external sources most of the events are located at the edge of the detector while the center has fewer events due to the self shielding of xenon. The radial veto implemented in the DDC-10 firmware provides a possibility to cut events at large radii before reading them out. Two additional digitizer inputs of the DDC-10 board are allocated for the radial veto. The sum-signal of two groups of PMTs can be connected to these channels, e.g., the outermost PMT ring and the second outermost ring of the top array. Each time the signal of the outer PMT ring exceeds the signal threshold the radial veto component starts to sum up the waveform of the outer and the inner PMT group. After the integration the following condition is checked

$$S_{\text{outer ring}} \cdot K_{\text{outer ring}} > S_{\text{inner ring}} \cdot K_{\text{inner ring}}, \tag{5.1}$$

where S is the integral of the outer/inner PMT group and the factors K can be set in the configuration file. If this condition is fulfilled, the event is assumed to be located in the outer part of the detector and is vetoed.

Veto decision and veto length

All peak properties, width, rise time and integral, are collected in the veto decision component, where the final veto decision and the veto length are computed. This component continuously monitors the baseline and as soon as it exceeds the signal threshold a new peak starts. At this time the veto delay is initiated and the component starts to collect the peak properties as they become available. Once a peak start is identified the output of the integral component is read out continuously and scanned for its maximum until the veto delay is over. As illustrated in figure 5.15 on page 97 the rise time and the width of the peak are available simultaneously as soon as the signal drops below 50 % of the peak maximum. If the integral maximum exceeds the threshold set in the configuration file, the event is categorized as possible HE event.

The decision whether a veto is triggered or not is based on the output of the four components introduced above (rise time, width, integral and radial position), depending on whether they are activated or not. The four components are connected by the following logic:

$$(\text{width} \wedge \text{rise time} \wedge \text{integral}) \vee (\text{radial position})$$

If a component is turned off in the configuration file it does not appear in the above logic. The individual conditions are true if:

- Rise time: the peak's rise time is larger than the rise time cut variable (discriminates S1 from S2).
- Width: the peak's width is larger than the width cut variable (discriminates S1 from S2).
- Integral: the maximum of the peak integral is above the integral cut variable (tags high energy events).
- Radial position: the fraction of light seen by the outer PMT group compared to the inner one is larger then the fraction defined in the settings. Furthermore, the width of the peak has to be larger than the width setting in order to ensure that only S2 peaks are considered by the radial veto.

The HEV firmware is able to veto the digitization of peaks for a flexible amount of time. This feature allows events with higher energies to be vetoed for a longer time than events with lower energies since the activity in the detector after an S2 peak depends on energy. The veto time is calculated by a 2nd order polynomial function where all parameters of the function are set in the configuration file within a range of $3 \cdot 10^{-15}$–32767. The argument of this polynomial function is the integral maximum of the peak (representing the energy) scaled down by a factor of 1024. Thus, for each peak the veto length is calculated by

$$p_2 \cdot \left(\frac{I_{\max}}{1024}\right)^2 + p_1 \cdot \left(\frac{I_{\max}}{1024}\right) + p_0 = \text{veto length}\,[10\,\text{ns}] \tag{5.2}$$

where the parameters p_0, p_1 and p_2 are set in the configuration file. A second order polynomial function has bee chosen since the energy dependent "activity" due to the photo-ionization tail after an S2 peak in XENON100, which is discussed in section 5.2, can be approximated by this function.

5.4 Busy-veto and acquisition monitor

In order to transfer PMT data from the digitizers to the reader machines, up to eight V1724 digitizer boards (=64 channels) are daisy chained via optical link and read out by one PC. The maximal readout speed of the optical link is 80 MB/s and thus, if the load is equally distributed, each board can be read out at 10 MB/s. Divided by eight channels, a read out speed of 1.25 [MB/s] = 625 [k samples/s] per channel can be achieved. In calibration mode this amount of data can be exceeded by the high event rate and the large photo-ionization tails following S2 peaks. The V1724 boards have an internal memory buffer of 1 MB/channel. This memory buffer allows data to be acquired continuously for at least 5 ms at which point the memory will be filled and the board cannot accept any more data until the buffer is cleared by the reader. In order to guarantee acquisition of large chunks of data with all channels, even if the input rate exceeds 1.25 MB/s (per channel), a busy-veto is implemented, which will be discussed in the following section.

Whenever the internal buffer of a digitizer is full (or close to full), it raises a busy signal and does not accept any more data. The busy states of all digitizers are available via an LVDS output on the front panel of the boards. The actual logic of the busy-veto is incorporated in a V1495 module from CAEN. The V1495 is a general purpose VME board with several I/O channels (LEMO and LVDS), where custom logic functions can be programmed on an FPGA. A block diagram of the busy firmware developed within this thesis can be seen in figure 5.17. In this firmware all busy outputs from the digitizers are combined by an OR-gate and the output of this logic-gate is distributed to the veto input of all V1724 ADCs, which enables to block the data acquisition on the digitizers. This set-up ensures that as long as at least one digitizer is busy, all of them stop taking data, because data with missing channels cannot be used for analysis. Since different digitizers could go busy shortly one after another this could result in a busy-veto constantly going on/off for short periods, which would significantly reduce the amount of useful events since many of them would contain a busy signal. In order to avoid this situation, a minimal busy length of 1 ms is implemented in the V1495 firmware. The intention of this is to allow the reader software to clear the memory buffer of the busy boards before resuming data taking such that a longer period can be recorded afterwards which contains full events without any busy-vetoes. If it occurs that after this 1 ms one (or more digitizers) is still busy the veto gets extended until the busy of all boards is off. As the digitizers only have one veto input in order to inhibit data taking, the HEV and the busy-veto are combined by an OR-gate on the V1495 firmware.

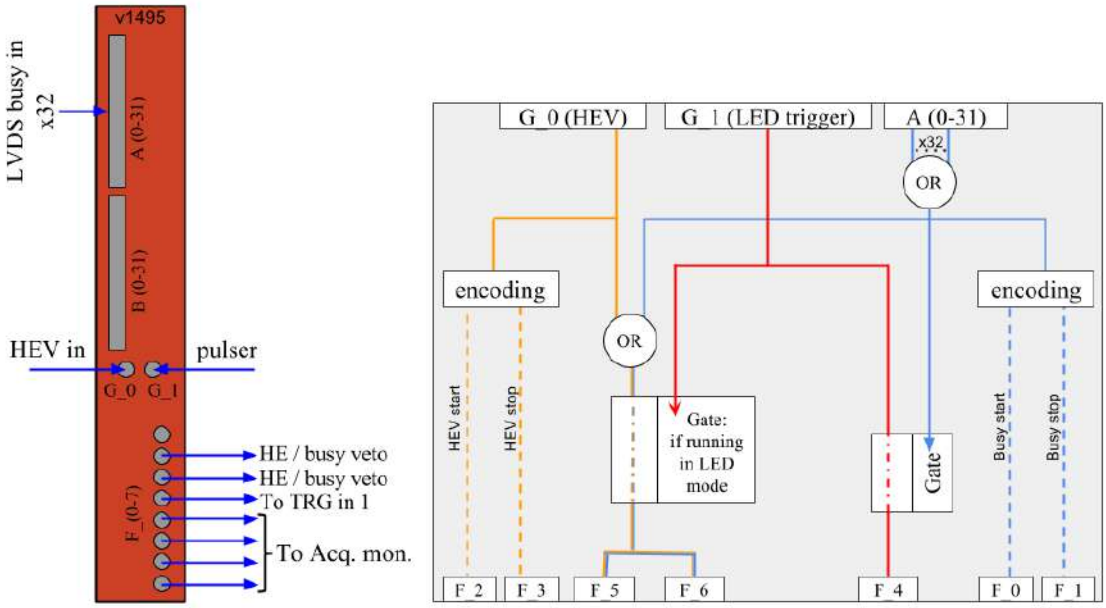

Figure 5.17: Block diagram of the busy firmware implemented on the CAEN board V1495. This board handles the logic of combining the busy signals of all digitizers with the HEV signal from the DDC-10 board. Furthermore, it encodes the busy/HEV into a start/stop signals on separate channels, which are sent to the acquisition monitor. If the detector is running in LED calibration mode the veto input of the digitizers is used as input for the external trigger. Thus, the trigger signal is also routed through the V1495 and is inhibited whenever a board gets busy.

For LED calibration the digitizers are triggered externally by a logic pulser signal which is routed through the V1495. The busy-firmware has two different sets of logic implemented: one for the self-trigger mode of the digitizers and one for external trigger. By checking the input from the LED trigger for incoming pulses it verifies in which mode the DAQ is running and which logic should be applied. During LED calibration the veto input of the digitizers is allocated by the CAEN firmware as input to trigger the digitizers. Thus, in LED mode the V1495 does not send any veto to the digitizers and in case of an occurring busy-veto, the LED trigger is blocked (and thus data taking stopped) for the duration of the veto.

Due to the fact that the HEV and the busy-veto might remove only parts of events it is important to be able to check if there was a veto during or close to an event while analyzing the data. This information is also needed to calculate the dead time of the DAQ. Therefore, both veto signals, HEV and busy-veto, are split into two output channels where one channel sends a short NIM pulse at the start time of the veto and the other at the stop time, resulting in four channels (HEV start/stop and busy start/stop). These four channels are recorded by a dedicated digitizer called “acquisition monitor”. By only recording the start/stop signals, the amount of data from these channels is minimal but contains all the relevant information. As the information of the acquisition monitor should always be available it is excluded from the veto system introduced above

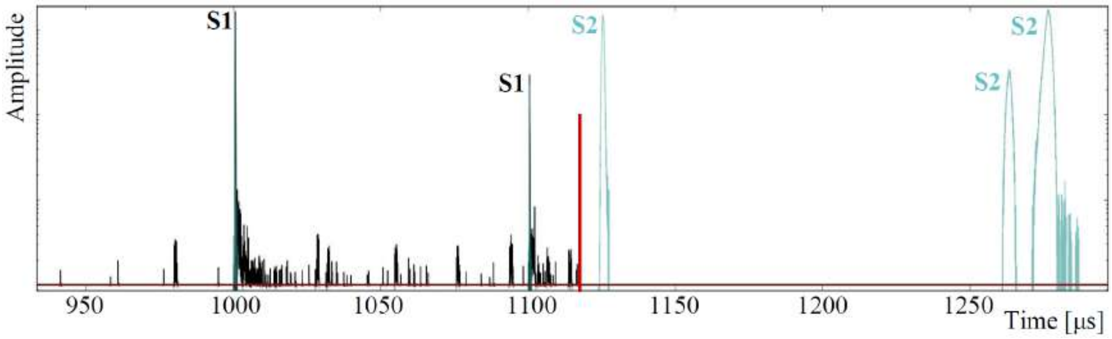

FIGURE 5.18: Waveform of an event containing a busy-veto. The black line shows the digital sum waveform of all TPC PMTs. The red vertical line indicates the start time of the busy-veto, recorded by the acquisition monitor. After the busy-veto started, no more data from the individual PMTs is available since the digitizers are vetoed. The analog sum signal (cyan line), recorded by the acquisition monitor, is still available and shows three S2 peaks happening during this period.

and keeps taking data during any veto happening. In order to prevent the monitoring digitizer going busy itself, it is read out by its own reader machine at up to 80 MB/s.

In addition to the veto information, the acquisition monitor records the TPC sum-waveform used as input signal for the HEV. The information of this channel is particularly useful during periods when the data acquisition was vetoed since large signals are still visible. In figure 5.18 the waveform of an event containing a busy-veto is shown. In this event it can be seen, that during the busy-veto, when the individual PMT channels are blind, the analog sum waveform is still recorded by the acquisition monitor, which reveals three S2 peaks occurring during the veto. Finally, one channel of the acquisition monitor records the signal from the Cherenkov muon veto detector trigger. Even though not every trigger is induced by a muon, this information can be used in order to quickly check if any uncommon occurrence might be related with a muon passing the detector. Furthermore, it can also be used for synchronisation with the muon veto system.

5.5 High energy veto performance test

The energy threshold above which a S2 peak is blocked by the HEV is motivated by the analysis and given in units of PE, calculated by the XENON1T data processor pax. It might depend on the different calibration sources or different purposes of the calibration. Since the peak integral estimated by the HEV is based on the uncorrected attenuated sum signal of the bottom PMT array, it will be different from the S2 peak area derived by pax. Thus, the relation between these two values needs to be calibrated. In order to perform this calibration, a data set has been acquired where the HEV-signals are recorded by the acquisition monitor but the peaks are not vetoed and thus all the

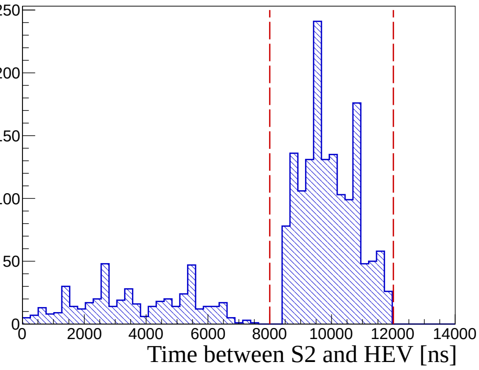

FIGURE 5.19: Time difference between the S2 peak and the starting point of the HEV. According to the settings on the DDC-10 board the HEV is expected to start $8\,\mu$s after the S2 peak. The reason why it is not a delta peak at $8\,\mu$s is that the left edge of an S2 peak in pax is not necessarily the same as the one derived in the HEV. The red dashed lines indicates the time region used in order to select HEV peaks.

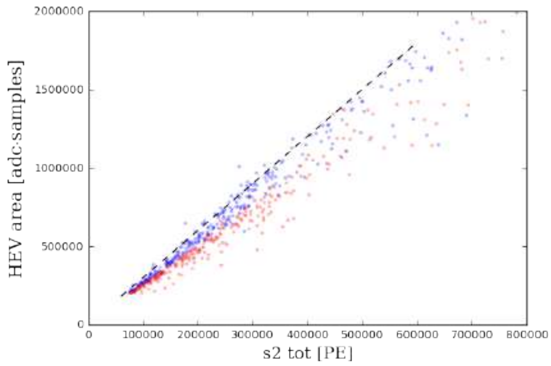

FIGURE 5.20: Correlation of the total area in PE from pax and the area calculated by the DDC-10. Blue points represent peaks with a smaller width than peaks shown as red points. It can be seen that the S2 area estimated by the DDC-10 of peaks with a large width is biased towards lower values as the integration window of the HE-veto does not cover the full peak. The black dashed line shows the correlation from equation (5.3).

information is available in the processed data. The following cuts are used in order to select S2 peaks that triggered the HEV:

1. There has to be an S2 peak within the event identified by pax.
2. There must be no other S2 peak in the event.
3. The HEV should start after the expected delay of $8\,\mu\text{s} < \Delta t < 12\,\mu\text{s}$.

The third cut, illustrated in figure 5.19, shows the start position of the HEV with respect to the position of the S2 peak. Since the veto delay in this data is set to $8\,\mu$s it should in principle always start at exactly this position. The reason for the spread is that the S2 position derived by the HEV is not necessarily the same as the one derived by pax. The HEV searches close to the rising edge while pax defines the peak time more towards the center of the peak. Figure 5.20 shows the remaining events after applying the above cuts with the S2 energy from pax on the x-axis and the integrated sum waveform from the HEV on the y-axis. The latter is inferred from the length of the veto, which is directly proportional to the integral if the parameters from equation (5.2) are set to $p_2 = 0,\ p_1 = 1,\ p_0 = 0$. The black dashed line indicates the linear relation between the S2 area calculated by pax and the one from the DDC-10 board and thus can be used in order to derive the HEV threshold to be set for a certain S2 size given in PE. The functional form of this line is:

$$A_{\text{DDC}-10}(\text{S2}_{\text{tot}}) = 3 \cdot \text{S2}_{\text{tot}}. \tag{5.3}$$

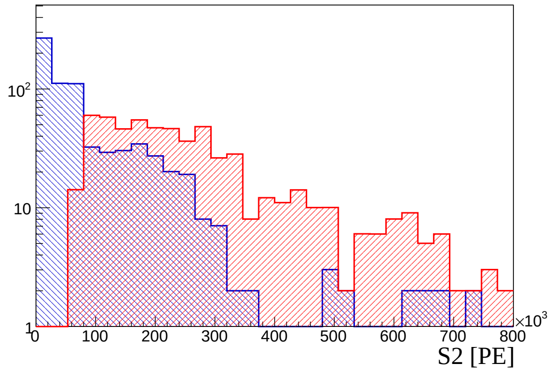

FIGURE 5.21: S2 energy spectrum from XENON1T. S2 peaks where the HEV did not fire are represented by the blue histogram and peaks where the HEV did fire by the red histogram. The HEV starts to fire at a well defined S2 energy, corresponding to the threshold set to 66000 PE. The somewhat slow fall-off of the blue spectrum is due to the spread of events seen in figure 5.20

The data points do not appear on a sharp line because the integration window of the HEV might not cover the full S2 peak which leads to an underestimation of the area. This can be seen by the fact that peaks with a larger width (figure 5.20, red points) show a larger bias in the area calculation compared to the peaks with a smaller width (blue points). Furthermore, the area calculation by the DDC-10 is only based on the uncorrected sum signal of the bottom PMTs. In figure 5.21 an S2 energy spectrum is shown where the blue histogram represents S2 peaks where the HEV did not fire and the red histogram peaks where the HEV did fire. The threshold used in this run was 66000 PE (derived from equation (5.3)). As expected the HEV starts to fire at a well defined S2 energy corresponding to the threshold. On the other hand, the blue spectrum, where the HEV did not fire, does not fall off as quickly at the threshold energy. This is expected because of the spread of events seen in figure 5.20. In this test the HEV removed $\sim 70\,\%$ of all S2 peaks above the HEV-threshold.

Conclusion and future improvements

In this chapter the veto system for the DAQ of XENON1T has been introduced. This veto system consists of a high energy veto in order to reject events outside the energy region of interest during calibration campaigns to reduce the data load on the DAQ. Furthermore, it features a busy-veto which inhibits data taking if the memory-buffer of one or more digitizers is full and cannot store additional data. Both vetoes are realized by means of custom-developed FPGA firmware codes. Currently, the veto system is installed and is in use as part of the XENON1T DAQ. The fact that both vetoes are implemented on an FPGA makes them very flexible regarding future upgrades since the firmware can be updated at any time. In the following, possible future improvements of the veto-system are outlined.

Currently, the minimal length for the busy-veto is hardcoded on the firmware of the V1495 to be 1 ms. Even though updating the firmware in order to change this parameter is not a major effort, it would be more practical to be able to change the minimal length of the busy-veto by setting a value in the register such that the parameter can be defined by kodiaq at the start of a run. In fact, the ideal design would be not to veto for a constant time window but to inhibit data taking until the memory buffer of all digitizers (not only the ones that went busy) are cleared again. However, the implementation of this approach is not straightforward as it requires to monitor the state of all memory buffers. In principle, this could be done by the reader PCs. However, this would take a non-negligible amount of time. Ideally, the V1724 digitizers should activate a signal on one of their LVDS outputs if their buffer is empty or only filled up to an adjustable threshold. Similarly to the busy-output, this signal could be monitored by the V1495 board, which then could extend any busy-veto until all boards are cleared.

In order to increase the flexibility of the HEV, it could be useful to implement the possibility of vetoing events based on their S1 peaks. This feature could be used for example in case of an ER calibration with an internal ^{220}Rn source [116]. In addition to the γ-decays, this source will also induce many interactions from α-decays. Since these α-events have a much lower S2 signal than ERs of the same size, it is not possible any more to veto them based on their S2 size without affecting the ER region to be calibrated.

As introduced in section 5.3, the firmware of the HEV in principle is able to veto events based on their radial position inside the TPC. So far this feature has never been tested in XENON1T as the relevant inputs for the DDC-10 board were not realized. In order to enable this possibility, it would require to sum up the outer most PMT ring of the top array as well as a second group representing the inner part of the TPC by installing more summation and attenuation stages made from linear fans.

Chapter 6

Summary and Outlook

Since the first identification of the missing mass problem in 1933 [3], the question of what dark matter is made of became one of the fundamental questions of physics. Without the presence of dark matter at all length scales it is not possible to explain the structures of the Universe as it is observed today. Despite the fact that dark matter interacts gravitationally and that it contributes $\sim 26\,\%$ to the energy density of the Universe, relatively little is know about its particle nature. Many experiments are aiming for a direct detection, which would reveal the nature of dark matter. Among them are the XENON detectors with the recently completed dark matter program of XENON100 [75] and the currently running detector XENON1T [54].

In the framework of this thesis, the background model for the analysis of the third science run of XENON100 as well as for the reanalysis of the first and second science run has been developed. These background models were used in the combined analysis of all three runs, comprising a total exposure of 17.6 tons$\times$days [75]. The result confirms the absence of a WIMP dark matter signal and the limits on the spin-independent WIMP-nucleon as well as on the spin-dependent WIMP-neutron and WIMP-proton cross sections were improved with respect to the previous XENON100 limits by a factor of ~ 1.7, reaching an exclusion of spin-independent WIMP-nucleon cross section of $1.1 \times 10^{-45}\,\mathrm{cm}^2$ at $50\,\mathrm{GeV/c}^2$ (at 90 % CL). This work is presented in chapter 3.

The null result from [75] as well as null results from other experiments are in strong conflict with the dark matter detection claim by DAMA/LIBRA [59] if their $9.3\,\sigma$ modulation signal is interpreted within the usual framework of standard WIMP interactions. Magnetic inelastic dark matter (MiDM), proposed by Chang et al. [145], provides an alternative to the classical WIMP scenario in order to reconcile the null results with the DAMA/LIBRA signal. In this thesis the first search for dark matter-induced delayed coincidence signals, predicted by the MiDM model is presented, using the 224.6 live days of the XENON100 science run II. No signal has been found and a limit on the interaction strength has been calculated. In certain parameter space a significant improvement was achieved with respect to previous results in [147], excluding the modulation signal measured by DAMA/LIBRA being due to MiDM. The analysis and results are described in chapter 4.

In order to significantly increase the sensitivity to WIMP interactions, the XENON collaboration has built the first ton-scale direct dark matter detector, XENON1T, which is currently running at LNGS in Italy. The goal of this detector is to improve the sensitivity to the spin-independent WIMP-nucleon cross section by two orders of magnitude compared to XENON100, down to spin-independent WIMP-nucleon cross sections of $1.6 \times 10^{-47}\,\mathrm{cm}^2$ at a WIMP mass of $50\,\mathrm{GeV/c}^2$ [54]. Besides several other improvements, a new data acquisition system (DAQ) has been developed for XENON1T. As part of this thesis a veto system for the DAQ has been developed based on FPGAs, and is presented in chapter 5. This system includes a high energy veto based on the charge signal, a busy veto and the possibility of a veto depending on the radial position of an event. The veto system has been installed at LNGS and is currently operational in the DAQ system of XENON1T.

The future of noble liquid direct dark matter detectors

So far there is no convincing evidence for a dark matter signal from direct detection experiments [161]. The current best limit by LUX is based on an exposure of 33.5 tons×days, excluding spin-independent WIMP-nucleon cross sections above $1.1 \times 10^{-46}\,\mathrm{cm}^2$ at a WIMP mass of $50\,\mathrm{GeV/c}^2$ [80]. In order to significantly increase the sensitivity and to open up the chance of a discovery at, detectors with a considerably larger target mass (beyond the ton-scale) are needed. The first ton-scale detector, XENON1T, is already in operation and currently taking data. Further ton-scale noble liquid detectors are ArDM [162], a liquid argon TPC under commissioning with a target mass of 850 kg, and DEAP-3600 [56], a single phase liquid argon detector with a fiducial mass of 1 ton, which started taking science data. Other experiments with even larger target masses, such as LZ [81] and XENONnT [54], are in construction or planing phase.

The ultimate sensitivity of noble liquid direct detection experiments, limited by the irreducible background from coherent neutrino-nucleus scattering [163], will be reached by detectors containing multi-tons of target material. A proposal for such a detector is the DARk matter WImp search with liquid xenoN (DARWIN) experiment [84]. Like XENON1T, this detector will be a liquid xenon TPC, but containing a total target mass of 40 tons. The baseline design of DARWIN is a dual-phase TPC read out by

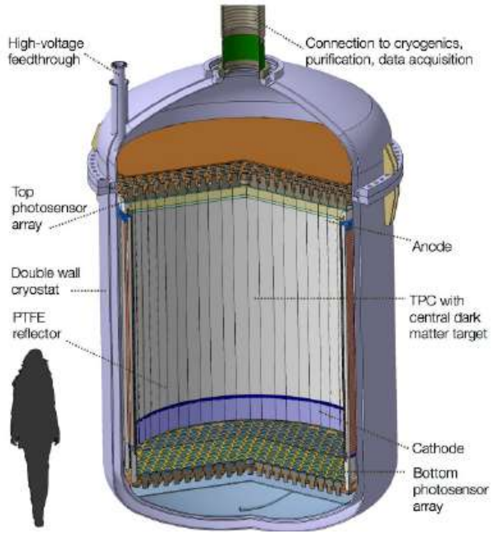

FIGURE 6.1: A possible realisation of the $\sim$ 50 t (40 t) total (target) LXe mass DARWIN detector, inside a double-walled stainless steel cryostat. The TPC is surrounded by highly reflective PTFE walls, closed by the cathode and anode electrodes on bottom and top, respectively. The sketch shows a TPC with two photosensor arrays made of circular PMTs with 3" diameter, similar to XENON1T. Figure from [84].

two arrays of photosensors. However, the feasibility of alternative light and charge readout concepts is under study. In figure 6.1 a possible realization of the TPC and other detector components are shown. The detector will be located inside a water Cherenkov shield. Additionally it might be shielded by a liquid scintillator detector, acting as a neutron veto, to achieve the required neutron background level. With an exposure of 200 tons $\times$ years (500 tons $\times$ years) this detector will reach a sensitivity to spin-independent WIMP interactions of $2.5 \times 10^{-49}\,\mathrm{cm}^2$ ($1.5 \cdot 10^{-49}\,\mathrm{cm}^2$) at a WIMP mass of $40\,\mathrm{GeV/c}^2$ [84].

In figure 6.2 the current and predicted limits of future noble liquid detectors are shown. If dark matter should be discovered by current direct detection experiments, DARWIN will be able acquire more statistics and to constrain the mass and the scattering cross section of the dark matter particle. Although the main purpose of DARWIN is to probe the entire experimentally accessible parameter space for WIMPs, its large target mass, low energy threshold and low background opens the possibility to study other rare processes as well [84]. Among them are solar pp-neutrinos, coherent neutrino-nucleus interactions and the search for solar axions and axion-like particles. Furthermore, the search for the neutrinoless double beta decay will be possible via the xenon isotope ^{136}Xe.

In conclusion, following the successful track of noble liquid detectors, there is a potential for a discovery of a dark matter particle in the next decade, considering the current and near-future detectors up to the ultimate detector DARWIN. However, if by this time dark matter has not yet been found, new detection techniques such as directional detection are needed in order to overcome the irreducible neutrino background [166], which will be limiting conventional noble liquid detectors [163]. However, it remains to be demonstrated, that directional detectors can achieve the exposure and background level required to be able to probe such low cross sections.

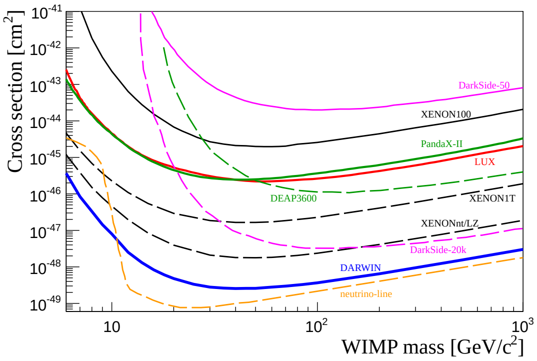

FIGURE 6.2: Existing upper limits on the WIMP-nucleon cross section from DarkSide-50 [164], XENON100 [86], PandaX-II [53], and LUX [80] together with the projected limits from DEAP-3600 [56], XENON1T [54], XENONnT [54], LZ [81], DarkSide-20k [165] and for a 200 tons × years exposure of DARWIN [84].

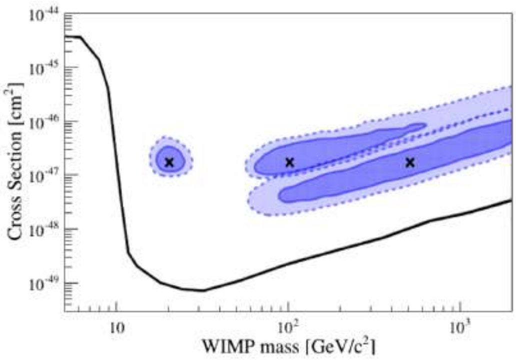

FIGURE 6.3: Simulated $1\,\sigma$ and $2\,\sigma$ confidence regions, showing how well the WIMP parameters can be reconstructed in DARWIN after a $200\,\mathrm{t} \times \mathrm{y}$ exposure. The '×' indicate the simulated benchmark models for three different WIMP masses of $20\,\mathrm{GeV/c^2}$, $100\,\mathrm{GeV/c^2}$ and $500\,\mathrm{GeV/c^2}$, assuming a cross section of $2 \times 10^{-47}\,\mathrm{cm}^2$, which is close to the sensitivity limit of XENON1T. Figure from [84].

Bibliography

[1] (Planck), P. A. R. Ade, et al. Planck 2015 results. XIII. Cosmological parameters. *Astron. Astrophys.*, 594:A13, 2016.

[2] J. C. Kapteyn. First Attempt at a Theory of the Arrangement and Motion of the Sidereal System. *Astrophys. J.*, 55:302–328, 1922.

[3] F. Zwicky. Die Rotverschiebung von extragalaktischen Nebeln. *Helv. Phys. Acta*, 6:110–127, 1933. [Gen. Rel. Grav.41,207(2009)].

[4] Edwin Hubble and Milton L. Humason. The Velocity-Distance Relation among Extra-Galactic Nebulae. *Astrophys. J.*, 74:43–80, 1931.

[5] M. L. Kutner. Astronomy, A Physical Perspective. chapter 13, pages 225–231. Cambridge University Press, 2003.

[6] V. C. Rubin, N. Thonnard, and W. K. Ford, Jr. Extended rotation curves of high-luminosity spiral galaxies. IV - Systematic dynamical properties, SA through SC. *ApJL*, 225:L107–L111, 1978.

[7] D. Walsh, R. F. Carswell, and R. J. Weymann. 0957 + 561 A, B - Twin quasistellar objects or gravitational lens. *Nature*, 279:381–384, 1979.

[8] Douglas Clowe, Marusa Bradac, Anthony H. Gonzalez, Maxim Markevitch, Scott W. Randall, Christine Jones, and Dennis Zaritsky. A direct empirical proof of the existence of dark matter. *Astrophys. J.*, 648:L109–L113, 2006.

[9] K. G. Begeman, A. H. Broeils, and R. H. Sanders. Extended rotation curves of spiral galaxies: Dark haloes and modified dynamics. *Mon. Not. Roy. Astron. Soc.*, 249:523, 1991.

[10] A. A. Penzias and R. W. Wilson. A Measurement of Excess Antenna Temperature at 4080 Mc/s. *Astrophysical Journal*, 142:419–421, 1965.

[11] G. F. Smoot et al. Structure in the COBE differential microwave radiometer first-year maps. *ApJL*, 396:L1–L5, 1992.

[12] (WMAP), E. Komatsu, et al. Seven-Year Wilkinson Microwave Anisotropy Probe (WMAP) Observations: Cosmological Interpretation. *Astrophys. J. Suppl.*, 192: 18, 2011.

[13] C. Alcock et al. Possible Gravitational Microlensing of a Star in the Large Magellanic Cloud. *Nature*, 365:621–623, 1993.

[14] E. Aubourg et al. Evidence for gravitational microlensing by dark objects in the galactic halo. *Nature*, 365:623–625, 1993.

[15] (EROS-2), P. Tisserand, et al. Limits on the Macho Content of the Galactic Halo from the EROS-2 Survey of the Magellanic Clouds. *Astron. Astrophys.*, 469: 387–404, 2007.

[16] Marc Davis, George Efstathiou, Carlos S. Frenk, and Simon D. M. White. The Evolution of Large Scale Structure in a Universe Dominated by Cold Dark Matter. *Astrophys. J.*, 292:371–394, 1985.

[17] S. D. M. White, C. S. Frenk, and M. Davis. Clustering in a neutrino-dominated universe. *ApJL*, 274:L1–L5, 1983.

[18] Joop Schaye et al. The EAGLE project: Simulating the evolution and assembly of galaxies and their environments. *Mon. Not. Roy. Astron. Soc.*, 446:521–554, 2015.

[19] R. D. Peccei and Helen R. Quinn. CP Conservation in the Presence of Pseudoparticles. *Phys. Rev. Lett.*, 38:1440–1443, 1977.

[20] F. Wilczek. Problem of Strong P and T Invariance in the Presence of Instantons. *Phys. Rev. Lett.*, 40:279–282, 1978.

[21] Steven Weinberg. A New Light Boson? *Phys. Rev. Lett.*, 40:223–226, 1978.

[22] Jihn E. Kim. Weak-Interaction Singlet and Strong CP Invariance. *Phys. Rev. Lett.*, 43:103–107, 1979.

[23] Mikhail A. Shifman, A. I. Vainshtein, and Valentin I. Zakharov. Can Confinement Ensure Natural CP Invariance of Strong Interactions? *Nucl. Phys.*, B166:493–506, 1980.

[24] Michael Dine, Willy Fischler, and Mark Srednicki. A Simple Solution to the Strong CP Problem with a Harmless Axion. *Phys. Lett.*, B104:199–202, 1981.

[25] A. R. Zhitnitsky. On Possible Suppression of the Axion Hadron Interactions. (In Russian). *Sov. J. Nucl. Phys.*, 31:260, 1980. [Yad. Fiz.31,497(1980)].

[26] (ADMX), S. J. Asztalos, et al. A SQUID-based microwave cavity search for dark-matter axions. *Phys. Rev. Lett.*, 104:041301, 2010.

[27] (OSQAR), R. Ballou, et al. New exclusion limits on scalar and pseudoscalar axionlike particles from light shining through a wall. *Phys. Rev.*, D92(9):092002, 2015.

[28] Klaus Ehret et al. New ALPS Results on Hidden-Sector Lightweights. *Phys. Lett.*, B689:149–155, 2010.

[29] (XENON), E. Aprile, et al. First Axion Results from the XENON100 Experiment. *Phys. Rev.*, D90(6):062009, 2014.

[30] Gerard Jungman, Marc Kamionkowski, and Kim Griest. Supersymmetric dark matter. *Phys. Rept.*, 267:195–373, 1996.

[31] Fabio Iocco, Miguel Pato, and Gianfranco Bertone. Evidence for dark matter in the inner Milky Way. *Nature Phys.*, 11:245–248, 2015.

[32] Mark W. Goodman and Edward Witten. Detectability of certain dark-matter candidates. *Phys. Rev. D*, 31:3059–3063, 1985.

[33] David G. Cerdeno and Anne M. Green. Direct detection of WIMPs. *arXiv:1002.1912 [astro-ph.CO]*, 2010.

[34] Anne M. Green. Astrophysical uncertainties on direct detection experiments. *Mod. Phys. Lett.*, A27:1230004, 2012.

[35] Richard H. Helm. Inelastic and Elastic Scattering of 187-Mev Electrons from Selected Even-Even Nuclei. *Phys. Rev.*, 104:1466–1475, 1956.

[36] J. Menendez, D. Gazit, and A. Schwenk. Spin-dependent WIMP scattering off nuclei. *Phys. Rev.*, D86:103511, 2012.

[37] Andrzej K. Drukier, Katherine Freese, and David N. Spergel. Detecting cold dark-matter candidates. *Phys. Rev. D*, 33:3495–3508, 1986.

[38] Katherine Freese, Joshua Frieman, and Andrew Gould. Signal modulation in cold-dark-matter detection. *Phys. Rev. D*, 37:3388–3405, 1988.

[39] David N. Spergel. Motion of the Earth and the detection of weakly interacting massive particles. *Phys. Rev. D*, 37:1353–1355, 1988.

[40] G. Angloher et al. Commissioning Run of the CRESST-II Dark Matter Search. *Astropart. Phys.*, 31:270–276, 2009.

[41] (CDMS), Z. Ahmed, et al. Search for Weakly Interacting Massive Particles with the First Five-Tower Data from the Cryogenic Dark Matter Search at the Soudan Underground Laboratory. *Phys. Rev. Lett.*, 102:011301, 2009.

[42] (SuperCDMS), R. Agnese, et al. Search for Low-Mass Weakly Interacting Massive Particles with SuperCDMS. *Phys. Rev. Lett.*, 112:241302, 2014.

[43] Cecile Kéfélian. Status of the EDELWEISS-III Dark Matter search. *J. Phys. Conf. Ser.*, 606(1):012002, 2015.

[44] (CRESST-II), G. Angloher, et al. Results on low mass WIMPs using an upgraded CRESST-II detector. *Eur. Phys. J.*, C74(12):3184, 2014.

[45] (PICO), C. Amole, et al. Dark Matter Search Results from the PICO-2L C_3F_8 Bubble Chamber. *Phys. Rev. Lett.*, 114:231302, 2015.

[46] Chris Jillings. The SNOLAB Science Program. *J. Phys. Conf. Ser.*, 718(6):062028, 2016.

[47] (PICO), C. Amole, et al. Improved dark matter search results from PICO-2L Run 2. *Phys. Rev.*, D93(6):061101, 2016.

[48] E. Behnke et al. Final Results of the PICASSO Dark Matter Search Experiment. *arXiv:1611.01499 [hep-ex]*, 2016.

[49] (COUPP), E. Behnke, et al. First Dark Matter Search Results from a 4-kg CF_3I Bubble Chamber Operated in a Deep Underground Site. *Phys. Rev.*, D86(5): 052001, 2012. [Erratum: Phys. Rev.D90,no.7,079902(2014)].

[50] M. Felizardo et al. Final Analysis and Results of the Phase II SIMPLE Dark Matter Search. *Phys. Rev. Lett.*, 108:201302, 2012.

[51] W. H. Lippincott, K. J. Coakley, D. Gastler, A. Hime, E. Kearns, D. N. McKinsey, J. A. Nikkel, and L. C. Stonehill. Scintillation time dependence and pulse shape discrimination in liquid argon. *Phys. Rev.*, C78:035801, 2008.

[52] (LUX), D. S. Akerib, et al. Improved Limits on Scattering of Weakly Interacting Massive Particles from Reanalysis of 2013 LUX Data. *Phys. Rev. Lett.*, 116(16): 161301, 2016.

[53] (PandaX-II), Andi Tan, et al. Dark Matter Results from First 98.7 Days of Data from the PandaX-II Experiment. *Phys. Rev. Lett.*, 117(12):121303, 2016.

[54] E. Aprile et al. Physics reach of the XENON1T dark matter experiment. *Journal of Cosmology and Astroparticle Physics*, 2016(04):027, 2016.

[55] (DarkSide), P. Agnes, et al. Results from the first use of low radioactivity argon in a dark matter search. *Phys. Rev.*, D93(8):081101, 2016.

[56] (DEAP-3600) and Nasim Fatemighomi. DEAP-3600 dark matter experiment. In *35th International Symposium on Physics in Collision (PIC 2015) Coventry, United Kingdom, September 15-19, 2015*, 2016.

[57] D. Acosta-Kane et al. Discovery of underground argon with low level of radioactive 39Ar and possible applications to WIMP dark matter detectors. *Nucl. Instrum. Meth.*, A587:46–51, 2008.

[58] J. B. R. Battat et al. DMTPC: Dark matter detection with directional sensitivity. *PoS*, IDM2010:042, 2011.

[59] (DRIFT), J. B. R. Battat, et al. First background-free limit from a directional dark matter experiment: results from a fully fiducialised DRIFT detector. *Phys. Dark Univ.*, 9-10:1–7, 2015.

[60] (DMTPC) and Michael Leyton. Directional dark matter detection with the DMTPC m^3 experiment. *J. Phys. Conf. Ser.*, 718(4):042035, 2016.

[61] Q. Riffard et al. Dark Matter directional detection with MIMAC. In *Proceedings, 48th Rencontres de Moriond on Very High Energy Phenomena in the Universe: La Thuile, Italy, March 9-16, 2013*, pages 227–230, 2013.

[62] (Super-Kamiokande), K. Choi, et al. Search for neutrinos from annihilation of captured low-mass dark matter particles in the Sun by Super-Kamiokande. *Phys. Rev. Lett.*, 114(14):141301, 2015.

[63] (IceCube), M. G. Aartsen, et al. Search for Dark Matter Annihilations in the Sun with the 79-String IceCube Detector. *Phys. Rev. Lett.*, 110:131302, 2013.

[64] Marc Schumann. Dark Matter 2013. *Braz. J. Phys.*, 44:483–493, 2014. [,1314(2013)].

[65] Christoph Weniger. A Tentative Gamma-Ray Line from Dark Matter Annihilation at the Fermi Large Area Telescope. *JCAP*, 1208:007, 2012.

[66] (Fermi-LAT), M. Ackermann, et al. Search for gamma-ray spectral lines with the Fermi large area telescope and dark matter implications. *Phys. Rev.*, D88:082002, 2013.

[67] (PAMELA), Oscar Adriani, et al. An anomalous positron abundance in cosmic rays with energies 1.5-100 GeV. *Nature*, 458:607–609, 2009.

[68] (AMS), M. Aguilar, et al. First Result from the Alpha Magnetic Spectrometer on the International Space Station: Precision Measurement of the Positron Fraction in Primary Cosmic Rays of 0.5–350 GeV. *Phys. Rev. Lett.*, 110:141102, 2013.

[69] (PAMELA), O. Adriani, et al. PAMELA results on the cosmic-ray antiproton flux from 60 MeV to 180 GeV in kinetic energy. *Phys. Rev. Lett.*, 105:121101, 2010.

[70] Peng-Fei Yin, Zhao-Huan Yu, Qiang Yuan, and Xiao-Jun Bi. Pulsar interpretation for the AMS-02 result. *Phys. Rev.*, D88(2):023001, 2013.

[71] (ATLAS), Georges Aad, et al. Search for dark matter candidates and large extra dimensions in events with a jet and missing transverse momentum with the ATLAS detector. *JHEP*, 04:075, 2013.

[72] (ATLAS), Georges Aad, et al. Observation of a new particle in the search for the Standard Model Higgs boson with the ATLAS detector at the LHC. *Phys. Lett.*, B716:1–29, 2012.

[73] G. Belanger, B. Dumont, U. Ellwanger, J. F. Gunion, and S. Kraml. Status of invisible Higgs decays. *Phys. Lett.*, B723:340–347, 2013.

[74] (ATLAS), Georges Aad, et al. Search for Invisible Decays of a Higgs Boson Produced in Association with a Z Boson in ATLAS. *Phys. Rev. Lett.*, 112:201802, 2014.

[75] (XENON), E. Aprile, et al. XENON100 Dark Matter Results from a Combination of 477 Live Days. *Phys. Rev.*, D94(12):122001, 2016.

[76] Marc Schumann, Laura Baudis, Lukas Bütikofer, Alexander Kish, and Marco Selvi. Dark matter sensitivity of multi-ton liquid xenon detectors. *JCAP*, 1510(10):016, 2015.

[77] (XENON), E. Aprile, et al. The XENON100 Dark Matter Experiment. *Astropart. Phys.*, 35:573–590, 2012.

[78] P. Zappa, L. Bütikofer, D. Coderre, B. Kaminsky, M. Schumann, and M. von Sivers. A versatile and light-weight slow control system for small-scale applications. *JINST*, 11(09):T09003, 2016.

[79] M. v. Sivers, B. A. Hofmann, Å.V. Rosén, and M. Schumann. The GeMSE Facility for Low-Background γ-Ray Spectrometry. *JINST*, 11(12):P12017, 2016.

[80] (LUX), D. S. Akerib, et al. Results from a search for dark matter in the complete LUX exposure. *Phys. Rev. Lett.*, 118(2):021303, 2017.

[81] (LZ), D. S. Akerib, et al. LUX-ZEPLIN (LZ) Conceptual Design Report. 2015.

[82] L. S. Miller, S. Howe, and W. E. Spear. Charge Transport in Solid and Liquid Ar, Kr, and Xe. *Phys. Rev.*, 166:871–878, 1968.

[83] E. Aprile, C. E. Dahl, L. DeViveiros, R. Gaitskell, K. L. Giboni, J. Kwong, P. Majewski, Kaixuan Ni, T. Shutt, and M. Yamashita. Simultaneous measurement of ionization and scintillation from nuclear recoils in liquid xenon as target for a dark matter experiment. *Phys. Rev. Lett.*, 97:081302, 2006.

[84] (DARWIN), J. Aalbers, et al. DARWIN: towards the ultimate dark matter detector. *JCAP*, 1611(11):017, 2016.

[85] G Plante. The XENON100 Dark Matter Experiment: Design, Construction, Calibration and 2010 Search Results with Improved Measurement of the Scintillation Response of Liquid Xenon to Low-Energy Nuclear Recoils. *PhD Thesis, Columbia University (2012).* URL `https://academiccommons.columbia.edu/catalog/ac%3A143844`.

[86] (XENON), E. Aprile, et al. Dark Matter Results from 225 Live Days of XENON100 Data. *Phys. Rev. Lett.*, 109:181301, 2012.

[87] (XENON), E. Aprile, et al. Low-mass dark matter search using ionization signals in XENON100. *Phys. Rev.*, D94(9):092001, 2016.

[88] Tadayoshi Doke, Akira Hitachi, Jun Kikuchi, Kimiaki Masuda, Hiroyuki Okada, and Eido Shibamura. Absolute Scintillation Yields in Liquid Argon and Xenon for Various Particles. *Japanese Journal of Applied Physics*, 41(3R):1538, 2002.

[89] M. J. Berger. Stopping-Power and Range Tables for Electrons, Protons, and Helium Ions, Jan 2017. URL `https://www.nist.gov/pml/stopping-power-range-tables-electrons-protons-and-helium-ions`.

[90] XCOM M. J. Berger, Jan 2017. URL `https://www.nist.gov/pml/xcom-photon-cross-sections-database`.

[91] Joshua Jortner, Lothar Meyer, Stuart A. Rice, and E. G. Wilson. Localized Excitations in Condensed Ne, Ar, Kr, and Xe. *The Journal of Chemical Physics*, 42 (12):4250–4253, 1965.

[92] Akira Hitachi, Tan Takahashi, Nobutaka Funayama, Kimiaki Masuda, Jun Kikuchi, and Tadayoshi Doke. Effect of ionization density on the time dependence of luminescence from liquid argon and xenon. *Phys. Rev.*, B27:5279–5285, 1983.

[93] (LUX), D. S. Akerib, et al. Low-energy (0.7-74 keV) nuclear recoil calibration of the LUX dark matter experiment using D-D neutron scattering kinematics. *arXiv:1608.05381*, 2016.

[94] A. Manalaysay et al. Spatially uniform calibration of a liquid xenon detector at low energies using 83m-Kr. *Rev. Sci. Instrum.*, 81:073303, 2010.

[95] (XENON), E. Aprile, et al. Response of the XENON100 dark matter detector to nuclear recoils. *Phys. Rev. D*, 88:012006, 2013.

[96] E. Aprile, L. Baudis, B. Choi, K. L. Giboni, K. Lim, A. Manalaysay, M. E. Monzani, G. Plante, R. Santorelli, and M. Yamashita. New measurement of the relative scintillation efficiency of xenon nuclear recoils below 10 keV. *Phys. Rev. C*, 79: 045807, 2009.

[97] A. Manzur, A. Curioni, L. Kastens, D. N. McKinsey, K. Ni, and T. Wongjirad. Scintillation efficiency and ionization yield of liquid xenon for monoenergetic nuclear recoils down to 4 keV. *Phys. Rev. C*, 81:025808, 2010.

[98] G. Plante, E. Aprile, R. Budnik, B. Choi, K.-L. Giboni, L. W. Goetzke, R. F. Lang, K. E. Lim, and A. J. Melgarejo Fernandez. New measurement of the scintillation efficiency of low-energy nuclear recoils in liquid xenon. *Phys. Rev. C*, 84:045805, 2011.

[99] M. Horn et al. Nuclear recoil scintillation and ionisation yields in liquid xenon from ZEPLIN-III data. *Physics Letters B*, 705(5):471 – 476, 2011. ISSN 0370-2693.

[100] J. Lindhard, V. Nielsen, M. Scharff, and P. V. Thomsen. Integral equations governing radiation effects. *Mat. Fys. Medd. Dan. Vid. Selsk. 33*, 1963.

[101] Fedor Bezrukov, Felix Kahlhoefer, Manfred Lindner, Felix Kahlhoefer, and Manfred Lindner. Interplay between scintillation and ionization in liquid xenon Dark Matter searches. *Astropart. Phys.*, 35:119–127, 2011.

[102] Brian Lenardo, Kareem Kazkaz, Aaron Manalaysay, Jeremy Mock, Matthew Szydagis, and Mani Tripathi. A Global Analysis of Light and Charge Yields in Liquid Xenon. *IEEE Trans. Nucl. Sci.*, 62(6):3387–3396, 2015.

[103] (XENON), E. Aprile, et al. Observation and applications of single-electron charge signals in the XENON100 experiment. *J. Phys.*, G41:035201, 2014.

[104] B. Edwards et al. Measurement of single electron emission in two-phase xenon. *Astropart. Phys.*, 30:54–57, 2008.

[105] C. Dahl. The physics of background discrimination in liquid xenon, and first results from Xenon10 in the hunt for WIMP dark matter. *PhD Thesis, Princeton University (2009).* URL `https://www.princeton.edu/physics/graduate-program/theses/theses-from-2009/E.Dahlthesis.pdf`.

[106] (ZEPLIN-III), V. N. Lebedenko, et al. Result from the First Science Run of the ZEPLIN-III Dark Matter Search Experiment. *Phys. Rev.*, D80:052010, 2009.

[107] L. Baudis, H. Dujmovic, C. Geis, A. James, A. Kish, A. Manalaysay, T. Marrodán Undagoitia, and M. Schumann. Response of liquid xenon to Compton electrons down to 1.5 keV. *Phys. Rev. D*, 87:115015, 2013.

[108] M Szydagis, N Barry, K Kazkaz, J Mock, D Stolp, M Sweany, M Tripathi, S Uvarov, N Walsh, and M Woods. NEST: a comprehensive model for scintillation yield in liquid xenon. *Journal of Instrumentation*, 6(10):P10002, 2011.

[109] E. Aprile et al. Measurement of the Scintillation Yield of Low-Energy Electrons in Liquid Xenon. *Phys. Rev.*, D86:112004, 2012.

[110] E. Aprile, K. L. Giboni, P. Majewski, K. Ni, and M. Yamashita. Observation of anticorrelation between scintillation and ionization for MeV gamma rays in liquid xenon. *Phys. Rev. B*, 76:014115, 2007.

[111] (XENON), E. Aprile, et al. Analysis of the XENON100 Dark Matter Search Data. *Astropart. Phys.*, 54:11–24, 2014.

[112] M. Ambrosio et al. Vertical muon intensity measured with MACRO at the Gran Sasso laboratory. *Phys. Rev. D*, 52:3793–3802, 1995.

[113] (XENON), E. Aprile, et al. Design and Performance of the XENON10 Dark Matter Experiment. *Astropart. Phys.*, 34:679–698, 2011.

[114] (XENON), E. Aprile, et al. Lowering the radioactivity of the photomultiplier tubes for the XENON1T dark matter experiment. *Eur. Phys. J.*, C75(11):546, 2015.

[115] (XENON), E. Aprile, et al. Conceptual design and simulation of a water Cherenkov muon veto for the XENON1T experiment. *JINST*, 9:11006, 2014.

[116] Rafael F. Lang, Andrew Brown, Ethan Brown, Mayra Cervantes, Sean Macmullin, Darryl Masson, Jochen Schreiner, and Hardy Simgen. A ^{220}Rn source for the calibration of low-background experiments. *JINST*, 11(04):P04004, 2016.

[117] (XENON), E. Aprile, et al. Material screening and selection for XENON100. *Astroparticle Physics*, 35(2):43 – 49, 2011. ISSN 0927-6505.

[118] L. Baudis et al. Gator: a low-background counting facility at the Gran Sasso Underground Laboratory. *JINST*, 6:P08010, 2011.

[119] C. Arpesella, S. Latorre, and P. P. Sverzellati. A Low background counting facility at Laboratori Nazionali del Gran Sasso. volume 47, pages 991 – 996, 1996.

[120] (XENON), E. Aprile, et al. Removing krypton from xenon by cryogenic distillation to the ppq level. *arXiv:1612.04284 [physics.ins-det]*, 2016.

[121] (XENON), E. Aprile, et al. Online ^{222}Rn removal by cryogenic distillation in the XENON100 experiment. *arXiv:1702.06942 [physics.ins-det]*, 2017.

[122] (XENON), E. Aprile, et al. First Dark Matter Results from the XENON100 Experiment. *Phys. Rev. Lett.*, 105:131302, 2010.

[123] (XENON), E. Aprile, et al. Dark Matter Results from 100 Live Days of XENON100 Data. *Phys. Rev. Lett.*, 107:131302, 2011.

[124] (XENON), E. Aprile, et al. Limits on spin-dependent WIMP-nucleon cross sections from 225 live days of XENON100 data. *Phys. Rev. Lett.*, 111(2):021301, 2013.

[125] (XENON), E. Aprile, et al. Search for Event Rate Modulation in XENON100 Electronic Recoil Data. *Phys. Rev. Lett.*, 115(9):091302, 2015.

[126] (XENON), E. Aprile, et al. Exclusion of Leptophilic Dark Matter Models using XENON100 Electronic Recoil Data. *Science*, 349(6250):851–854, 2015.

[127] R. Bernabei et al. DAMA results at Gran Sasso underground lab. *Nucl. Part. Phys. Proc.*, 263-264:87–92, 2015.

[128] (XENON), E. Aprile, et al. Search for Two-Neutrino Double Electron Capture of ^{124}Xe with XENON100. *arXiv:1609.03354*, 2016.

[129] J. Aalbers and C.D. Tunnell. The pax data processor v4.0.0, jul 2016. URL `https://doi.org/10.5281/zenodo.58613`.

[130] E. Aprile et al. The neutron background of the XENON100 dark matter search experiment. *Journal of Physics G: Nuclear and Particle Physics*, 40(11):115201, 2013.

[131] D.G. et al. Madland. SOURCES 4A: A Code for Calculating (alpha,n), Spontaneous Fission, and Delayed Neutron Sources and Spectra. *Technical Report LA-13539-MS, Los Alamos*, 1999.

[132] (GEANT4), S. Agostinelli, et al. GEANT4: A Simulation toolkit. *Nucl. Instrum. Meth.*, A506:250–303, 2003.

[133] V. A. Kudryavtsev. Muon simulation codes MUSIC and MUSUN for underground physics. *Comput. Phys. Commun.*, 180:339–346, 2009.

[134] Gary J. Feldman and Robert D. Cousins. A Unified approach to the classical statistical analysis of small signals. *Phys. Rev.*, D57:3873–3889, 1998.

[135] (PandaX), Xiang Xiao, et al. Low-mass dark matter search results from full exposure of the PandaX-I experiment. *Phys. Rev.*, D92(5):052004, 2015.

[136] Glen Cowan, Kyle Cranmer, Eilam Gross, and Ofer Vitells. Asymptotic formulae for likelihood-based tests of new physics. *Eur. Phys. J.*, C71:1554, 2011. [Erratum: Eur. Phys. J.C73,2501(2013)].

[137] (XENON), E. Aprile, et al. Likelihood Approach to the First Dark Matter Results from XENON100. *Phys. Rev.*, D84:052003, 2011.

[138] (PICO), C. Amole, et al. Dark matter search results from the PICO-60 CF_3I bubble chamber. *Phys. Rev.*, D93(5):052014, 2016.

[139] (DAMA), R. Bernabei, et al. First results from DAMA/LIBRA and the combined results with DAMA/NaI. *Eur. Phys. J.*, C56:333–355, 2008.

[140] (LUX), D. S. Akerib, et al. Results on the Spin-Dependent Scattering of Weakly Interacting Massive Particles on Nucleons from the Run 3 Data of the LUX Experiment. *Phys. Rev. Lett.*, 116(16):161302, 2016.

[141] R. Bernabei et al. Investigating the DAMA annual modulation data in a mixed coupling framework. *Phys. Lett.*, B509:197–203, 2001.

[142] (ZEPLIN-III), V. N. Lebedenko, et al. Limits on the spin-dependent WIMP-nucleon cross-sections from the first science run of the ZEPLIN-III experiment. *Phys. Rev. Lett.*, 103:151302, 2009.

[143] (CDMS), Z. Ahmed, et al. Search for Weakly Interacting Massive Particles with the First Five-Tower Data from the Cryogenic Dark Matter Search at the Soudan Underground Laboratory. *Phys. Rev. Lett.*, 102:011301, 2009.

[144] (XENON), E. Aprile, et al. Search for Electronic Recoil Event Rate Modulation with 4 Years of XENON100 Data. 2017.

[145] Spencer Chang, Neal Weiner, and Itay Yavin. Magnetic Inelastic Dark Matter. *Phys. Rev.*, D82:125011, 2010.

[146] David Tucker-Smith and Neal Weiner. Inelastic dark matter. *Phys. Rev.*, D64: 043502, 2001.

[147] G. Barello, Spencer Chang, and Christopher A. Newby. A Model Independent Approach to Inelastic Dark Matter Scattering. *Phys. Rev.*, D90(9):094027, 2014.

[148] R. Bernabei et al. New limits on WIMP search with large-mass low-radioactivity NaI(Tl) set-up at Gran Sasso. *Phys. Lett.*, B389:757–766, 1996.

[149] J. I. Collar. Quenching and channeling of nuclear recoils in NaI(Tl): Implications for dark-matter searches. *Phys. Rev.*, C88(3):035806, 2013.

[150] J. D. Lewin and P. F. Smith. Review of mathematics, numerical factors, and corrections for dark matter experiments based on elastic nuclear recoil. *Astropart. Phys.*, 6:87–112, 1996.

[151] Tongyan Lin and Douglas P. Finkbeiner. Magnetic Inelastic Dark Matter: Directional Signals Without a Directional Detector. *Phys. Rev.*, D83:083510, 2011.

[152] A. Liam Fitzpatrick, Wick Haxton, Emanuel Katz, Nicholas Lubbers, and Yiming Xu. The Effective Field Theory of Dark Matter Direct Detection. *JCAP*, 1302:004, 2013.

[153] Nikhil Anand, A. Liam Fitzpatrick, and W. C. Haxton. Weakly interacting massive particle-nucleus elastic scattering response. *Phys. Rev.*, C89(6):065501, 2014.

[154] S. Yellin. Finding an upper limit in the presence of unknown background. *Phys. Rev.*, D66:032005, 2002.

[155] X. Du et al. An atom trap system for practical 81Kr dating. *Rev. Sci. Instrum.*, 75, 2004.

[156] National Nuclear Data Center (NNDC), Jan 2017. URL `http://www.nndc.bnl.gov/nudat2/`.

[157] Maxim Pospelov, Neal Weiner, and Itay Yavin. Dark matter detection in two easy steps. *Phys. Rev.*, D89(5):055008, 2014.

[158] MongoDB Inc 2008-2017. The MongoDB 3.4 Manual, feb 2017. URL `https://docs.mongodb.com/manual`.

[159] Daniel Coderre, Cyril Grignon, and Christopher Tunnell. XENON1T/kodiaq: Production release, nov 2016. URL `https://doi.org/10.5281/zenodo.165486`.

[160] (XENON), E. Aprile, et al. Observation and applications of single-electron charge signals in the XENON100 experiment. *J. Phys.*, G41:035201, 2014.

[161] Teresa Marrodán Undagoitia and Ludwig Rauch. Dark matter direct-detection experiments. *Journal of Physics G: Nuclear and Particle Physics*, 43(1):013001, 2016.

[162] (ArDM), J. Calvo, et al. The ArDM Liquid Argon Time Projection Chamber at the Canfranc Underground Laboratory: a ton-scale detector for Dark Matter Searches. 2016.

[163] J. Billard, L. Strigari, and E. Figueroa-Feliciano. Implication of neutrino backgrounds on the reach of next generation dark matter direct detection experiments. *Phys. Rev.*, D89(2):023524, 2014.

[164] (DarkSide) M. Bossa. DarkSide-50, a background free experiment for dark matter searches. *JINST*, 9:C01034, 2014.

[165] (DarkSide), D. Franco, et al. The Search for Dark Matter with low-radioactivity Argon at LNGS, Letter of Intent. 2015.

[166] Philipp Grothaus, Malcolm Fairbairn, and Jocelyn Monroe. Directional Dark Matter Detection Beyond the Neutrino Bound. *Phys. Rev.*, D90(5):055018, 2014.

Acknowledgements

I would like to express my special appreciation and thanks to my supervisor, *Marc Schumann*, for the continuous support throughout my whole PhD. Your guidance has been very valuable and you have always taken the time to discuss with me the relevant issues. I learned a lot from you.

Many tanks to *Laura Baudis*, for agreeing to being my second referee without hesitation and for being part of the audit committee.

A special thank to *Daniel Coderre* for proofreading my thesis, as well as for all his help related to the DAQ, and to *Moritz von Sivers* for his valuable work on the magnetic inelastic dark matter analysis. In addition I would like to thank them, as well as *Basho Kaminsky*, for the great time during the last years, and for the nice games and the hard competition at the kicker table.

Thanks to the whole XENON collaboration for the fruitful discussions and to all the people I have met in Italy during shifts, detector installation and meetings. The best part of coming to LNGS has always been to meet you guys.

I would also like to thank all people from LHEP for the great time at a beer after work, barbecue, ski day and Christmas (after) parties.

I thank all my friends for their friendship over the last years and for their patience during intensive working and writing periods.

Last but certainly not least, I would like to thank my family for everything they did for me. You have always believed in me and encouraged me throughout my study. A special thanks to you *Laura* for your patience and your support.

Erklärung

gemäss Art. 28 Abs. 2 RSL 05

Name/Vorname:	Lukas Bütikofer
Matrikelnummer:	08-103-632
Studiengang:	PhD in Physics
Titel der Arbeit:	From XENON100 to XENON1T: direct dark matter searches with dual phase liquid xenon time projection chambers
Leiter der Arbeit:	Prof. Dr. Marc Schumann

Ich erkläre hiermit, dass ich diese Arbeit selbständig verfasst und keine anderen als die angegebenen Quellen benutzt habe. Alle Stellen, die wörtlich oder sinngemäss aus Quellen entnommen wurden, habe ich als solche gekennzeichnet. Mir ist bekannt, dass andernfalls der Senat gemäss Artikel 36 Absatz 1 Buchstabe r des Gesetzes vom 5. September 1996 über die Universität zum Entzug des auf Grund dieser Arbeit verliehenen Titels berechtigt ist. Ich gewähre hiermit Einsicht in diese Arbeit

Ort/Datum

Unterschrift

Lukas Bütikofer

Personal data

Lukas Bütikofer
Postgasse 42
3011 Bern
Switzerland

Date of Birth: 31.8.1988

Education

02/2017	**PhD in Physics**
06/2016	**Dark Matter 2016: From the smallest to the largest scales.** (Santander, Spain)
01/2015	**CHIPP PhD Winter School 2015** (Grindelwald, Switzerland)
2013–2/2017	**PhD studies in Physics at the University of Bern**
2013	**Master of Science in Physics**
2012	**Bachelor of Science in Physics**
2008-2013	**Studies in Physics at the University of Bern** Minors: Astronomy and Mathematics
2008	**Matura with major music**